Doctoral Dissertation
Doctoral Program in Physics (33rd cycle)

Resistive switching devices with improved control of oxygen vacancies dynamics

Ing. Vittorio Fra

* * * * * * *

Supervisor
Prof. Carlo Ricciardi

Doctoral Examination Committee:
Umberto Celano, Ph.D., Referee, imec
Prof. Enrique Miranda, Referee, Universitat Autònoma de Barcelona
Prof. Fernando Corinto, Politecnico di Torino
Prof. Emiliano Descrovi, Politecnico di Torino
Prof. Themis Prodromakis, University of Southampton

Politecnico di Torino
22nd April 2021

This thesis is licensed under a Creative Commons License, Attribution - Noncommercial - NoDerivative Works 4.0 International: see `www.creativecommons.org`. The text may be reproduced for non-commercial purposes, provided that credit is given to the original author.

I hereby declare that the contents and organisation of this dissertation constitute my own original work and does not compromise in any way the rights of third parties, including those relating to the security of personal data.

Vittorio Fra

Ing. Vittorio Fra

Torino, 9th November 2020

Summary

According to some analysts, the information revolution responsible for the unprecedentedly fast technological development of last decades is about to give way to the "Neuromorphic Revolution", leaded by big data and artificial intelligence. Similar forecasts are made possible by the huge Research efforts that have been providing us deeper knowledge and enhanced control of emerging technologies expected to be the basis for next-generation computing. In this framework, resistive switching is one of the most relevant phenomena, and resistive switching devices are among the leading players in the upcoming breakthrough of neuromorphic computing. However, some open questions and unresolved issues have yet to be faced. Primarily, device reliability and integration with current technology standards need to be improved. In this Thesis, such aspects are accounted for through the investigation of possible strategies to deal with these issues in well-defined cases. Particularly, a specific class of resistive switching devices is investigated, focusing on the valence change memory (VCM) effect. This mechanism relies on the drift of oxygen anions, under the effect of an external voltage, within a metal oxide that consequently undergoes variations of its electrical resistance. Investigation of different oxides and different structures is reported, proposing possible technological strategies to tailor the device performances through an enhanced control on the key aspect in the VCM mechanism, namely the oxygen vacancies dynamics. The first resistive switching material investigated is zinc oxide. Characterized by a wide direct band gap, a large exciton energy, a good thermal and chemical stability, as well as biocompatibility, ZnO is widely employed for applications ranging from electronics to medicine. Such a versatility comes from the richness of nanostructures it can provide. In the field of resistive switching, zinc oxide is typically employed in form of thin films or nanowires, and in this Thesis the effect of a complementary action of these structures is reported, showing the improvements achieved in terms performances with respect to Pt/ZnO-film/Pt devices. The resistive switching instability observed for these latter, explained by a lack of ionic species needed for the redox reactions of VCM mechanism, is mitigated by hydrothermally grown ZnO nanowire arrays. The additional zinc oxide

layer represented by the nanowires turns out to be affected by a slight understoichiometry suitable to supply the underlying ZnO film with a surplus of oxygen vacancies, thus filling the lack of ionic species for VCM resistive switching. Acting as an oxygen vacancies reservoir, zinc oxide nanowires provides significant performance improvements, with endurance and retention results outperforming previous data reported in literature for similar devices. Following the study on ZnO, investigations on hafnium dioxide are presented. Widely employed in electronics as a high-k dielectric, HfO_2 naturally emerged among the possible metal oxides to be exploited for resistive switching devices thanks to the well-established technological knowledge of its properties. In this Thesis, the case of resistive memory cells employing tungsten as oxidizing electrode for VCM-based devices is discussed. The HfO_2/W interface has been indeed previously reported to be affected by critical resistive switching instabilities hindering them from providing reliable performances, and the insertion of a titanium buffer layer between hafnium dioxide and tungsten has been proposed to mitigate such issue. An extensive investigation of this stabilization strategy is presented, with systematic electrical characterizations on more than one hundred devices. The role played by titanium is analysed at different stages of resistive switching operations varying both thickness and composition of the buffer layers: in addition to pure-Ti films with thickness of 1 nm, 3 nm and 5 nm, a mixed W-Ti layer, with 10% in weight of titanium and thickness of 3 nm, is employed. The impact of the buffer layer properties on the main resistive switching parameters, namely the forming voltage (V_{FORMING}), the switching voltages (V_{SET} and V_{RESET}) and the resistance levels (R_{LRS} and R_{HRS}), is reported and discussed. Investigation of the forming process by means of conductive atomic force microscopy (C-AFM) is also presented, showing the filamentary nature of the observed resistive switching. Finally, results from tests in the dynamic operational regime are reported, showing how the different oxidizing activity of titanium and tungsten play a key role in the involved VCM mechanism. Thanks to a more efficient oxygen extraction, Ti can indeed hinder the more energy demanding tungsten oxidation, especially avoiding the metastable oxides formed before WO_3 is achieved and thus mitigating, or avoiding, resistive switching instabilities.

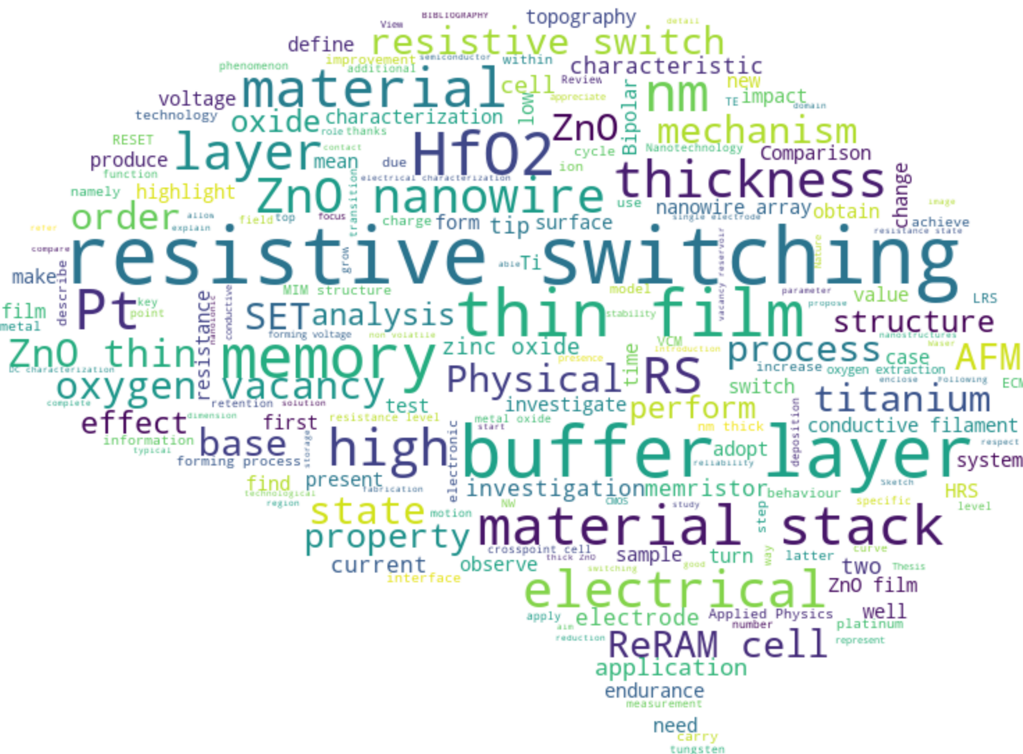

resistive switching
buffer layer
thin film
material stack
memory
HfO2
electrical
ZnO nanowire
thickness
material
layer
Pt
nm
RS
ZnO thin
oxygen vacancy
high
resistive switch
mechanism
titanium
ReRAM cell
Physical
process
AFM
SET
analysis
state
property
order
structure
ZnO
oxide
effect
base
perform
topography
characteristic
characterization
define
voltage
cell
produce
mean
highlight
zinc oxide
nanowire array
tip
surface
form
investigation
memristor
conductive filament
application
endurance
need
electrode
current
observe
sample
turn
two
ZnO film
well
Comparison
impact
new
Bipolar
low
cycle
switch
test
investigate
first
find
present
adopt
system
case
value
obtain
change
achieve
make
film
describe
resistance
time
deposition
electronic
step
HRS
latter
Applied Physics
platinum
information
forming process
namely
technology
RESET
phenomenon
improvement
additional
within
MIM structure
zinc oxide
increase
oxygen extraction
behaviour
metal
Ti
charge
due
ion
use

Contents

List of Tables xi

List of Figures xii

1 Introduction 1
- 1.1 Historical overview 1
- 1.2 Physical and electronic background 4
  - 1.2.1 Memristor and memristive systems 4
  - 1.2.2 Resistive switching mechanisms 9
  - 1.2.3 Resistive switching devices as digital memories 17
- 1.3 Future applications and perspectives 21
- 1.4 Thesis outlook 23

2 Device fabrication 25
- 2.1 ZnO-based devices 26
  - 2.1.1 ZnO thin films 27
  - 2.1.2 ZnO nanowires 27
- 2.2 HfO_2-based devices 28
  - 2.2.1 Crosspoint ReRAM cells 28
  - 2.2.2 Single-electrode ReRAM cells 30

3 Characterization methodologies 31
- 3.1 ZnO-based devices 32
- 3.2 HfO_2-based devices 40

4 ZnO nanowires as oxygen vacancies reservoir 43
- 4.1 Resistive switching in ZnO thin films 43
- 4.2 Conductive filament observation in ZnO thin films 46

4.3 Improved resistive switching with ZnO nanowires 52
4.3.1 Electrical characterization 52
4.3.2 Analysis of the resistive switching mechanism 57
4.4 Discussion 59

5 Ti-based buffer layers to modulate oxygen extraction from HfO_2 63
5.1 Device structure and buffer layer selection 64
5.2 Electrical characterization setups 66
5.3 Buffer layer influence on the forming voltage 67
5.3.1 DC characterization of crosspoint cells 67
5.3.2 C-AFM analysis 68
5.4 Impact of the buffer layer on device performances 74
5.5 Discussion 83

6 Conclusion 85

A Process flow for HfO_2-based crosspoint cells 91

B Force estimation in contact mode AFM measurements 97

C Superposition of current and topography data from C-AFM analysis 101

Nomenclature 105

Bibliography 108

List of Tables

1.1 Benchmarking of ReRAM compared to DRAM and Flash technologies [94] 21
4.1 Comparison of RS performances for devices based on ZnO nanowire arrays [130] 61
5.1 Material stacks of the investigated ReRAM cells [135] 65
5.2 Statistical analysis of the DC characterization [135] 79
5.3 Summary of endurance and retention tests with mean values and coefficients of variation for R_{HRS} and R_{LRS} [135] 83

List of Figures

1.1 Data from Scopus on the trend of scientific publications in the resistive switching domain since 1990. Partial data for 2020 have been omitted . 3
1.2 The complete set of relationships and basic circuit elements relying on the four fundamental variables of circuit theory. Standard symbols for the nonlinear elements are used [32] 6
1.3 The hysteretic *i*-*v* characteristics observed in MIM structures with understoichiometric semiconductors was modelled by the Williams' group at the HP labs through the motion of oxygen vacancies acting as charged dopants [25] 9
1.4 Classification of resistive switching mechanisms proposed in [43] . . . 10
1.5 Sketch of a nanoionics-based device with its simple MIM structure and filamentary conduction mechanism 11
1.6 Schematic representation of typical *i*-*v* characteristics obtained applying voltage ramps. Adapted from [14] 12
1.7 Schematic representation of filamentary resistive switching, with formation, partial dissolution and recovery of the CF 13
1.8 Summary of the electrochemical processes, and the corresponding *i*-*v* curve, of a typical ECM cell operating in sweep mode. Adapted from [60] 14
1.9 Schematic modelling of the CF in a VCM cell through oxygen vacancies migration. Adapted from [64] 15
1.10 Schematization of the memory hierarchy. Connections between units and levels from the CPU to the external input sources are summarized 18
1.11 Scheme of the cell structure and of the charge storage for SRAMs, DRAMs and Flash memories. Adapted from [85] 19
1.12 In-memory computing consists in performing computational tasks ($f(D)$) without moving data (D) back and forth from the memory unit to the processing unit. Adapted from [85] 20
1.13 Data from Table 1.1 mapped onto a Kiviat diagram 21

2.1 Data from Scopus about publications on ZnO nanostructures and HfO_2. Partial data for 2020 have been omitted . . . 26
2.2 Sketch of a ZnO-based device with a ZnO nanowire array grown on top of the zinc oxide thin film . . . 27
2.3 Sketch of a crosspoint ReRAM cell with highlights on the key elements of the fabrication process . . . 29
3.1 Classification of the characterization techniques available for RS investigation proposed in [136] . . . 31
3.2 FESEM cross-section image of a ZnO thin film . . . 32
3.3 By means of false colours, the different layers are highlighted in the cross-section picture of a ZnO thin film . . . 33
3.4 FESEM cross-section image of a ZnO nanowire array . . . 33
3.5 The Pt top electrode is well defined on top of the NWs, without significant deposition across the array . . . 34
3.6 Top-view by FESEM characterization of a nanowire array . . . 34
3.7 FESEM image of a nanowire array with a 30° tilt with respect to the top-view . . . 35
3.8 The XPS depth profile of the NW array highlights a good confinement of the Pt TE on top of the NWs and a slight ZnO understoichiometry within the array . . . 35
3.9 Good stoichiometry of the ZnO thin film reported by the XPS depth profile 36
3.10 Fit and analysis of the O 1s peak in ZnO thin films . . . 36
3.11 Fit and analysis of the O 1s peak in ZnO nanowire arrays . . . 37
3.12 Raman spectrum of ZnO thin films . . . 37
3.13 Raman spectrum acquired for nanowire arrays . . . 38
3.14 XRD pattern showing evidences of the wurtzite phase in ZnO thin films 39
3.15 XRD pattern of ZnO nanowires grown along the c-axis of the wurtzite phase . . . 39
3.16 FESEM images of crosspoint ReRAM cells with different magnification levels to highlight both the device arrangement on each sample and the crosspoint geometry of a single ReRAM cells . . . 40
3.17 AFM images with different colour maps of a VIA opening in single-electrode ReRAM cells . . . 41
4.1 Cycling operation of VCM devices employing ZnO films with thicknesses of 50 nm and 100 nm. Adapted from [143] . . . 44

4.2 Endurance tests carried out for the 100 nm thick ZnO films in VCM configuration showed easily collapsing HRS and LRS levels. Adapted from [143] 45
4.3 Cycle-to-cycle reliability in ECM devices with 250 nm thick ZnO film. Adapted from [143] 45
4.4 Retention up to 800 s obtained for ECM devices with 250 nm thick ZnO film. Adapted from [143] 46
4.5 Topography map acquired through a tapping mode measurement on ZnO thin film. Adapted from [143] 47
4.6 Surface roughness analysis from the height signal of the AFM map acquired in tapping mode 48
4.7 Forming process observed by C-AFM on 250 nm thick ZnO film 50
4.8 2D conduction map on 250 nm thick ZnO film after pointwise voltage ramps 51
4.9 Scheme of the *i*-*v* characterization setup 53
4.10 Forming process of a Pt/ZnO/NWs/Pt device. Adapted from [130] 53
4.11 Representative subset of the *i*-*v* curves collected for more than 110 consecutive cycles. Adapted from [130] 54
4.12 The V_{SET} and V_{RESET} narrow distribution resulting from the cyclic *i*-*v* characterization. Adapted from [130] 54
4.13 Endurance of the NW-based devices showing stable resistance levels for more than 1100 cycles. Adapted from [130] 55
4.14 Retention tests for the NW-based devices. Both the ON state and the OFF state were retained for more than 10^5 s. Adapted from [130] 55
4.15 Cyclic *i*-*v* curves and endurance measurement obtained after the retention tests showing an almost unchanged operability of the devices. Adapted from [130] 56
4.16 Sketch of the RS transitions occurring thanks to the nanowire array acting as an oxygen vacancies reservoir. Adapted from [130] 57
4.17 *i*-*v* characteristics of NW-based devices in full-logarithmic plot with fit. Adapted from [130] 58
5.1 Data from Scopus on the number of papers, published since 2000, focusing on HfO_2-based resistive switching devices. Partial data for 2020 have been omitted 64
5.2 Schemes of the setups employed for the electrical characterizations of the ReRAM cells 66

5.3 Comparison of the *i*-*v* characteristics during forming process for the different material stacks investigated. Adapted from [135] 67
5.4 Exponential decrease of the forming voltage as a function of the Ti-based buffer layer thickness. Adapted from [135] 68
5.5 Representative *i*-*v* characteristics acquired by C-AFM for the forming process of devices without buffer layer. Adapted from [135] 69
5.6 Representative *i*-*v* characteristics acquired by C-AFM for the forming process of devices with the MixBuffer material stack. Adapted from [135] 70
5.7 Representative *i*-*v* characteristics acquired by C-AFM for the forming process of devices with the Buffer3 material stack. Adapted from [135] 70
5.8 Current map acquired after forming on a single-electrode ReRAM cell without buffer layer. Adapted from [135] 71
5.9 Current map acquired after forming on single-electrode ReRAM cell with MixBuffer material stack. Adapted from [135] 71
5.10 Current map acquired after forming on single-electrode ReRAM cell with a 3 nm thock titanium buffer layer. Adapted from [135] 72
5.11 Comparison between topography and electrical conduction localization for the NoBuffer material stack. Adapted from [135] 72
5.12 Comparison between topography and electrical conduction localization for the MixBuffer material stack. Adapted from [135] 73
5.13 Comparison between topography and electrical conduction localization for the Buffer3 material stack. Adapted from [135] 73
5.14 Box plots from the statistical analysis of resistance levels and switching voltages for devices with NoBuffer, MixBuffer and Buffer5 material stack. Adapted from [135] 75
5.15 Sketch of the VCM-based filamentary resistive switching in crosspoint cells, with the conductive filament modelled as the result of oxygen vacancies motion within the HfO_2 layer 76
5.16 Comparison of cyclic *i*-*v* characteristics acquired for each material stack. Adapted from [211] 76
5.17 Representative *i*-*v* characteristics of resistive switching cycles for each material stack. Adapted from [135] 77
5.18 Summary of the switching voltages from statistical analysis of the DC characterization. Adapted from [135] 78
5.19 Summary of the resistance levels from statistical analysis of the DC characterization. Adapted from [135] 78
5.20 Optimized pulse parameters for each material stack. Adapted from [135] 80

5.21 Comparison of endurance performances, for each material stack, through a fixed-length test employing 2000 SET-RESET pulse pairs. Adapted from [135] 81
5.22 Comparison of resistance state retention, for each material stack, through a common benchmark of $2{\cdot}10^4$ s. Adapted from [135] 82

Chapter 1

Introduction

Technology is the way human beings overcome their limits. But what if technology could do the same for itself? Would that be pure, authentic artificial intelligence (AI)? Can mankind create it? Is the information revolution driving us toward self-learning machines? As it often happens, great challenges and complex questions do not have simple answers, and within them a multitude of problems exists, which change and evolve every time new solutions are found. In this complexity, resistive switching (RS) devices are like the tile of a mosaic: a small contribution to achieve an amazing result.

1.1 Historical overview

The first appearances of resistive switching in scientific and technical literature date back to the end of 19th Century [1–3]. In [1, 2], Prof. Calzecchi-Onesti, reported studies on the conductivity of metallic filings enclosed in little glass tubes (3.5 cm long with inner diameter of 1 cm). By applying external, electrical stimuli, he showed that it was possible to produce changes in conduction which were retained in time depending on the specific metal employed. These findings, represented, few years later, the basis for the receiver in the Marconi's wireless telegraph [3], which was made by a device similar to the one described by Prof. Calzecchi-Onesti, called *coherer* or *radio-conductor*, filled with mixed filings of silver and nickel. In the configuration used by Marconi, the coherer was a forerunner of the metal-insulator-metal (MIM) structure. The metallic filings, indeed, were placed into a small gap created between two electrodes, and were used, in their pristine state, as insulator. When, decades later, in the 1960s, similar phenomena started again attracting interest [4], dielectric films replaced the metallic filings, but the MIM structure was preserved. At that time, the concept of resistive switching had not

been fully established yet, and the *"anomalous behaviour"* [5] observed was often referred to as negative resistance. For the whole decade, Research provided new results on RS phenomena and continuously enlarged the field of investigation, involving materials like NiO [6], Nb_2O_5 [7], Ta_2O_5 [8], SiO [9] and TiO_2 [10].
The same productivity did not hold in 1970s, that instead gave preferential treatment to the Si-based electronics, whose developments marked an epoch in the growth of the integrated circuit (IC) technology. Nevertheless, a milestone in the history of RS devices was laid within this decade: in 1971, the existence of the fourth basic circuit element, the *memristor*, was postulated by Chua [11], who also defined, five years later, the concept of *memristive device* [12]. The fading interest resistive switching obtained in this decade, and in the following one as well, can be explained, as mentioned, with the dawning era of silicon electronics, but this might be just half of the story. Another reason for the slowing down of research in RS can be found indeed in the difficulties encountered in understanding and controlling the phenomenon. If on one side silicon was getting more and more attention giving glimpses of success, on the other side resistive switching was still quite obscure. Especially in terms of technological applications, the resounding success of non-volatile memories (NVMs) based on MOSFETs (metal-oxide-semiconductor field-effect transistors), and then on EPROMs (erasable programmable read-only memories) and flash memories, thwarted most of the possible ambitions related to RS devices [13, 14].
Only in late 1990s things started changing with a renewed interest in resistive switching. In 1997, Asamitsu et al. reported on some magnetoresistive manganites exhibiting resistance changes upon electrical stimuli, showing that $Pr_{0.7}Ca_{0.3}MnO$ could undergo reversible resistive switching with resistance levels divided by more than three orders of magnitude [15]. Such results paved the way to the first integrated memory application of a resistive switching device: in 2002, Zhuang et al. presented a 64-bit array, fabricated with a 500 nm CMOS process, built on memory cells made of $Pr_{0.7}Ca_{0.3}MnO$ enclosed between platinum electrodes [16]. For the first time since Marconi's wireless telegraph, the RS phenomenon found a technological application, and the acronyms RRAM (resistance random access memory) and ReRAM (resistive random access memory) were introduced to identify non-volatile memories based on resistive switching devices [17, 18]. At the same time, key results were achieved for different materials too, extending the domain of investigation to electrochemically active metals like silver and to metal oxides. In 2001 and 2005, the Aono's group reported on atomic switches relying on the motion of silver ions [19, 20], while, in 2002, Mitkova and Kozicki presented a programmable metallization cell (PMC) based on the incorporation of silver in Ge-Se

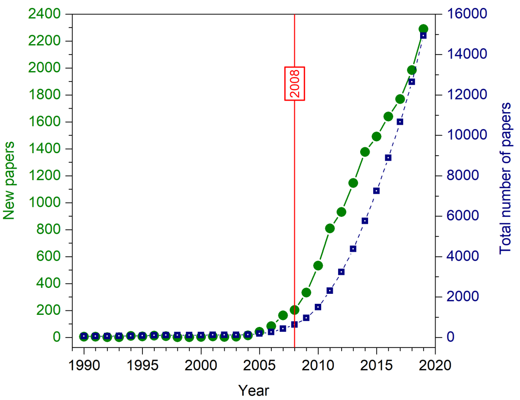

(a) In the 1990s and in the early 2000s, interest in resistive switching started growing again, and 2008 can be identified as the breakthrough year, with the number of new papers per year steeply increasing since then.

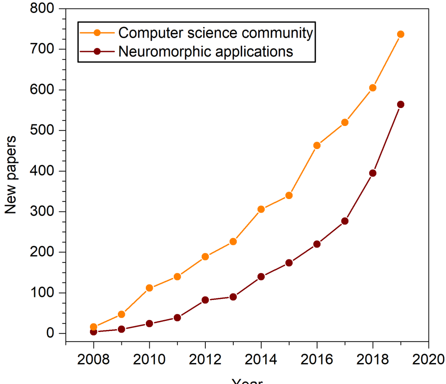

(b) Since 2008, resistive switching and its applications have attracted more and more interest in communities and research fields that were not involved, or did not even exist, up to that time.

Figure 1.1: Data from Scopus on the trend of scientific publications in the resistive switching domain since 1990. Partial data for 2020 have been omitted

glasses [21]. Concerning the advances with metal oxides, in 2004 a new class of resistive memories was proposed by Samsung with the acronym OxRRAM (oxide RRAM), to clearly indicate that, differently from the devices introduced in 2002 by Zhuang et al., the resistive switching material was an oxide. More in detail, the first OxRRAM presented was made of a transition metal oxide (TMO) like NiO enclosed between two noble metal electrodes [22]. Alongside this success in applications, two works, in 2006 and 2007, marked a turning point in understanding resistive switching in oxides proposing an explanation for the RS mechanism based on the motion of oxygen ions [23, 24].
In a period of such an impressive growth, that rapidly provided fundamental results in the theory as well as in the application domain, time was ripe for some disruptive contribution able to translate all the commitment of the last decade into an even greater interest in the subject. Something of such a fascinating impact that research in resistive switching could further improve fed by new and enthusiastic efforts. In 2008 all this happened. A paper by Strukov et al. gave the RS scientific community a new viewpoint: resistive switching devices can be interpreted in the framework of the memristor theory by Chua [25]. The impact of this work was almost immediate, with an increase of new papers published in 2009 of over 60%. In Figure 1.1, an analysis of the trend of scientific publications related to resistive switching is shown (data from Scopus). As it can be appreciated in Figure 1.1a, an unceasing growth took place starting from 2008, with

the period 2009-2011 characterized by an increase in the number of papers per year close to 300%, corresponding to more than 800 publications in 2011 compared with approximately 200 in 2008. Interestingly, the significant and continuous growth of new papers published each year started in 2007, that is to say the year after the publication by Waser's group of the already mentioned paper proposing the motion of oxygen ions as driving mechanism for resistive switching in oxides [23]. The prosperous period RS is still experiencing can be therefore traced back to the coupling of a turning point in the comprehension of the phenomenon with a cutting-edge intuition, which produced a combined impact able to captivate new scientific communities, like that of computer science, that scarcely contributed to the development of resistive switching applications up to that time. Such additional engagements were inspired by the new research horizons predicted straight away in 2008 with the suggestion of learning networks having synapse-like functions [25]: the era of neuromorphic applications for RS devices was rising [26–28]. In Figure 1.1b, a focus on the growing interest in the field of resistive switching for the computer science community is shown, together with data about the enlargement of literature on possible neuromorphic applications. After little more than a century, resistive switching might be again the key for an epochal advance in technology: at that time it was wireless telegraphy, now it is neuromorphic computing.

1.2 Physical and electronic background

Since the invention of the coherer, the improvements achieved in the comprehension of resistive switching phenomena have been leading to a better control on them, and this, in turn, has been encouraging further studies in a kind of positive feedback loop. As a consequence, as already mentioned, interest in resistive switching phenomena has spilled over into different domains: from physics and material science to electronics and computer science. Even neuroscience has been touched by the development of resistive switching devices [29, 30]. However, the beating hearth of this subject always remained in the physical and electronic domain, which still represent the propulsive thrust and the natural environment for novel, original advances in the comprehension, as well as in the applications, of resistive switching.

1.2.1 Memristor and memristive systems

As it is well known, circuit theory provides the models needed to describe and approximate the properties of physical elements, or phenomena, within electrical circuits [31]. The basis for such theory is represented by four fundamental variables: charge

(q), voltage (v), current (i) and flux-linkage (φ). Relying on them, the basic circuit elements are defined through their own constitutive relationships:

- resistor: $v(t) = R \cdot i(t)$
- capacitor: $i(t) = C \cdot \frac{\mathrm{d}v(t)}{\mathrm{d}t}$
- inductor: $v(t) = L \cdot \frac{\mathrm{d}i(t)}{\mathrm{d}t}$

In addition, two definitions are given to describe how the fundamental variables are in relation to each other:

- $q(t) = \int_{-\infty}^{t} i(\tau)\,\mathrm{d}\tau$
- $\varphi(t) = \int_{-\infty}^{t} v(\tau)\,\mathrm{d}\tau$

In this picture, what is missing is the relationship between the charge (q) and the flux-linkage (φ). In 1971, *"for the sake of completeness"*, the existence of a fourth basic circuit element was postulated by Leon Chua, who named it *memristor* from the contraction of the words *memory* and *resistor* [11]. Such two-terminal element is described by a constitutive equation of the type

$$\mathscr{M} = \{(q, \varphi) \,:\, f_M(q, \varphi) = 0\} \tag{1.1}$$

which can be made explicit in two forms:

- for a charge-controlled memristor:

$$v(t) = M(q(t)) \cdot i(t) \tag{1.2}$$

  where

$$M(q) \equiv \frac{\mathrm{d}\varphi(q)}{\mathrm{d}q} \tag{1.3}$$

  has the dimensions of a resistance and it is named *incremental memristance* (or *memristance*);

- for a flux-controlled memristor:

$$i(t) = W(\varphi(t)) \cdot v(t) \tag{1.4}$$

  where

$$W(\varphi) \equiv \frac{\mathrm{d}\varphi(q)}{\mathrm{d}q} \tag{1.5}$$

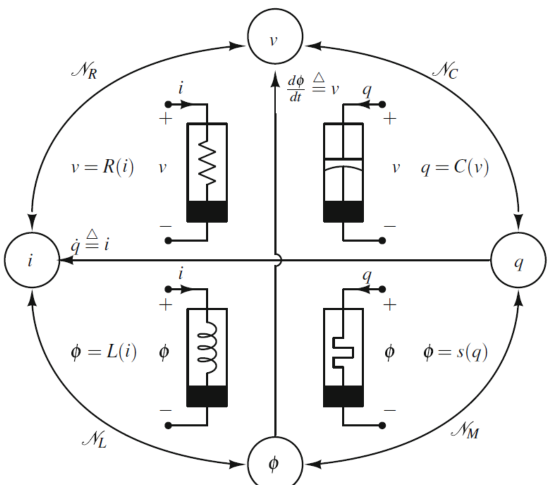

Figure 1.2: The complete set of relationships and basic circuit elements relying on the four fundamental variables of circuit theory. Standard symbols for the nonlinear elements are used [32]

has the dimensions of a conductance and it is named *incremental memductance* (or *memductance*) .

With the definition of the relationship between q and φ, the set of possible equations relating the four fundamental variables of circuit theory is eventually complete, as summarized in Figure 1.2.
Looking at (1.2) and comparing it with the constitutive equation of a resistor, it is clear that the memristor behaves, at a given time t_0, as a resistor whose resistance depends on the complete past history of the current flowed through itself. The genesis of the name is hence clarified: the fourth basic element postulated by Leon Chua can be described as a nonlinear resistor with memory.
Rapidly after the publication of Chua's paper, Oster and co-workers shed light on the possibility of applying the brand new model of the memristor also outside the electronic domain [33, 34], opening the way to its generalization through the definition of a wide class of systems named *memristive* [12]. The constitutive properties of such dynamical systems are described by an output equation embedding a dependence on the state of the system itself:

$$\begin{cases} \dot{x} = f(x, u, t) \\ y = g(x, u, t) \cdot u \end{cases} \tag{1.6}$$

where the time evolution of the state variable x represents the so-called state equation and the function $g(x, u, t)$ defines the dependence of the output equation on the state of the system. Given that the state equation must have a unique solution for any initial state x_0, the output equation is such that an input u equal to zero nullifies the output y regardless of the state x.
For what concerns the two functions f and g, they are defined as:

$$\begin{aligned} f &: \mathscr{R}^n \times \mathscr{R} \times \mathscr{R} \longrightarrow \mathscr{R}^n \\ g &: \mathscr{R}^n \times \mathscr{R} \times \mathscr{R} \longrightarrow \mathscr{R} \end{aligned} \tag{1.7}$$

resulting in an n-dimensional vector function and a scalar function respectively. The dimension of the function f, which corresponds to the dimension of the state space, defines the order of the system.
In the framework of memristive systems, hence following definition (1.6), the constitutive equation (1.2) can now be rewritten as:

$$\begin{cases} x = q \\ \dot{q} = i \\ v = M(q) \cdot i \end{cases} \tag{1.8}$$

where the charge q is now explicitly identified as the state variable of a charge-controlled memristor. In the same way, if one considers the flux-linkage φ as the state variable of a flux-controlled memristor, (1.4) becomes:

$$\begin{cases} x = \varphi \\ \dot{\varphi} = v \\ i = W(\varphi) \cdot v \end{cases} \tag{1.9}$$

Looking at (1.8) and (1.9), it can be appreciated how the memristor, which is now intended as a special case of memristive system in the electrical domain [12], behaves according to an output equation which has the dimensions of a state-dependent Ohm's law [35]. The distinguishing features of a memristor within the class of memristive systems have been clearly recalled in [36]:

- periodic current or voltage inputs with zero mean values result in an i-v output loop which is pinched at the origin and confined to the first and third quadrant;

- the shape of the output loop depends on both the amplitude and the frequency of the input.

Despite the comprehensive theoretical description relying on exhaustive mathematical definitions and demonstrations provided by the aforementioned works, the concept of memristor (and memristive system) struggled to find real applications, likely because of a lack of evidences for connections with physical properties of practical systems. Only in 2008 *"a physical model of a two-terminal electrical device that behaves like a perfect memristor"* was proposed for the first time [25]. Stanley Williams' group showed that memristive effects can naturally take place in nanoscale systems when electronic and ionic transport phenomena are coupled under the effect of an external bias [25, 37]. The experimental *i-v* curve of a cross-point device, having a MIM structure made of platinum electrodes sandwiching a titanium oxide film, was compared with simulations relying on a model built upon boundary motion in a semiconductor film exhibiting regions of different dopant concentration (Figure 1.3). Under an external voltage *v(t)* applied at the Pt electrodes, the charged dopants within the semiconductor film are forced to drift, and the boundary between the doped region and the undoped one moves. Assuming ohmic conduction, linear ionic drift and uniform electric field, the equations of the model were defined as:

$$\begin{cases} v(t) = \left(R_{\mathrm{ON}}\dfrac{w(t)}{D} + R_{\mathrm{OFF}}\left(1 - \dfrac{w(t)}{D}\right)\right)i(t) \\ \dfrac{\mathrm{d}w(t)}{\mathrm{d}t} = \mu_{\mathrm{V}}\dfrac{R_{\mathrm{ON}}}{D}i(t) \end{cases} \tag{1.10}$$

where μ_V is the average ion mobility, $w(t)$ is the width of the doped region and it depends on time, D is the thickness of the semiconductor film, R_{ON} and R_{OFF} are the resistances of the doped and the undoped region respectively.
From the second line of (1.10), it was straightforward to obtain the width of the doped region in time:

$$w(t) = \mu_{\mathrm{V}}\frac{R_{\mathrm{ON}}}{D}q(t) \tag{1.11}$$

which, assuming $R_{ON} \ll R_{OFF}$, was used to define the memristance as it follows:

$$M(q) = R_{\mathrm{OFF}}\left(1 - \frac{\mu_{\mathrm{V}}R_{\mathrm{ON}}}{D^2}q(t)\right) \tag{1.12}$$

Proposing a model able to describe experimental results from a *memristive* standpoint had a double effect. On the one hand it brought new blood to a research field that found

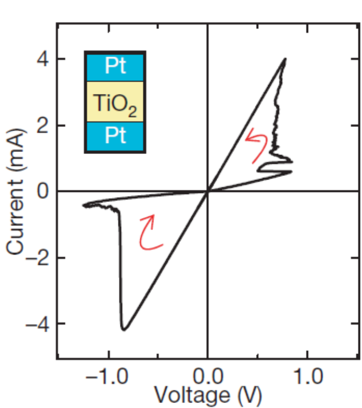

(a) Experimental characteristics of a device with platinum electrodes and under-stoichiometric titanium dioxide

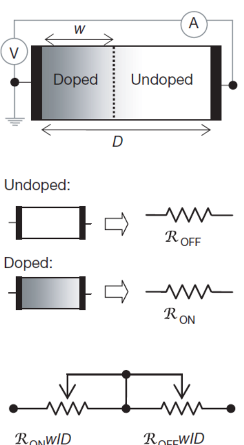

(b) Scheme and equivalent circuit of the model for a semiconductor film enclosed between two metal electrodes

Figure 1.3: The hysteretic *i*-*v* characteristics observed in MIM structures with under-stoichiometric semiconductors was modelled by the Williams' group at the HP labs through the motion of oxygen vacancies acting as charged dopants [25]

it hard to establish during decades of minor advances, on the other hand it implicitly, but it might be more correct to say unwittingly, introduced a dualism fated to evolve into a controversy rather than into a complementarity. Indeed, beside a scepticism reasoned starting from the absence in the proposed model of any relationship with magnetism [38], the thorny issue of whether RS devices are memristors or not naturally came out. Contrary to the early confidence in a possible identity between resistive switching devices and the concept of memristor [35], more recent results seem to suggest its impossibility [39], and new theoretical insights into the memristor theory have been proposed clearly distinguishing the ideal device from the so-called binary memristors, which do not fulfil the requirement, contained in the original definition of 1971, of an infinite number of stable states [40]. Such devices, however, have been widely investigated as non-volatile memories, and are commonly referred to as resistive memories [41, 42].

1.2.2 Resistive switching mechanisms

Resistive switching is a multifaceted phenomenon whose result is the reversible change of electrical resistance in two-terminal devices subject to external stimuli. Typified by reversibility and non-volatility, it is practically employed, in a more and more

widespread way nowadays, for devices aimed to provide repetitive changes in conductivity whose effects must be retained in time according to specific application requirements [14]. Relying on the memristive perspective of 1976 [12], here exemplified by (1.8) and (1.9), resistive switching can be phenomenologically explained with changes induced, by the externally applied stimuli, in an internal state variable that controls the electrical resistance. Such internal variable can show a manifold nature, assuming different characteristics depending on the specific physical mechanism involved in each device. This multiplicity can be summarized with three major classes: magnetic phenomena, electrostatic phenomena and atomic configurations [43]. Each of them, in turn, encloses a variety of processes, ranging from spin-torque transfer to nanoionic redox reactions, from leakage currents to structural phase changes (see Figure 1.4).
Amid this abundance, nanoionics-based devices have been recognized for a prime position among the promising candidates for non-charge-based memories [44, 45]. Compared to other reliable mechanisms like spin-torque transfer and phase change, redox reactions have shown indeed some significant advantages. First, they enable simpler device structures, as an insulating layer enclosed between two metal electrodes represents the basic requirement to achieve non-volatile resistive switching [46]. Second, their current consumption turns out to be extremely low and independent of the device size, as a filamentary mechanism of electrical conduction establishes when the device

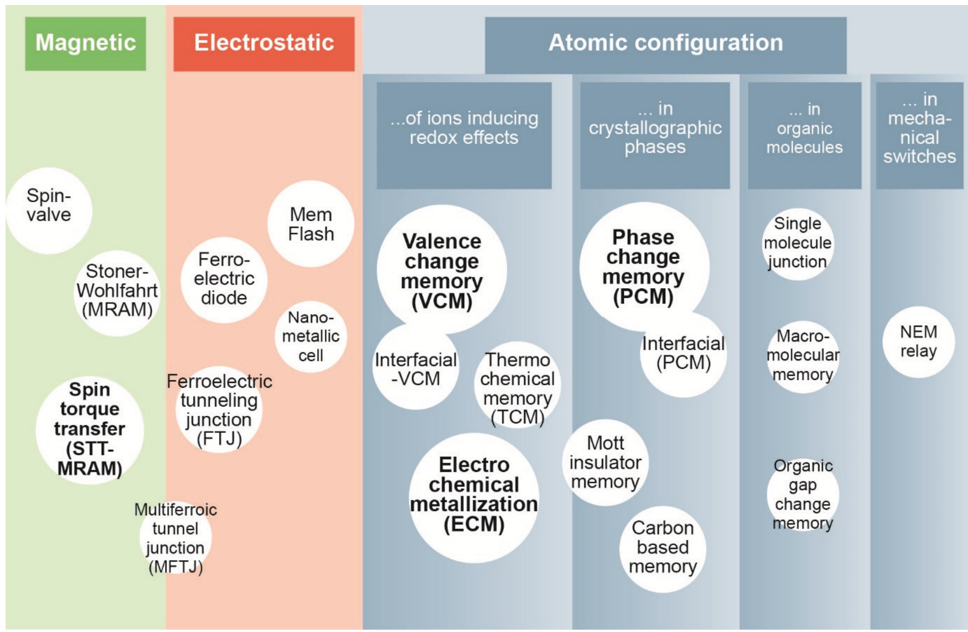

Figure 1.4: Classification of resistive switching mechanisms proposed in [43]

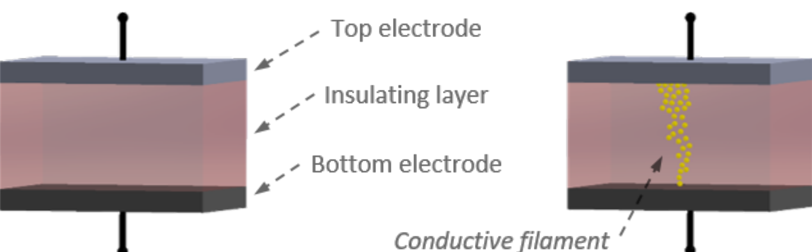

Figure 1.5: Sketch of a nanoionics-based device with its simple MIM structure and filamentary conduction mechanism

is in operating conditions [47]. To further emphasize their significance not only from a technological standpoint but also for a somehow symbolic value they have in the field of resistive switching, it is worth highlighting that the device presented in [25] as experimental comparison for the *"physical model of a two-terminal electrical device that behaves like a perfect memristor"* can be classified as nanoiocs-based [37, 48]. The inset of Figure 1.3b shows its simple metal-insulator-metal structure, and a general schematization of nanoionics-based RS devices [49] is sketched in Figure 1.5.
With an overall view, hence regardless of the specific phenomena and mechanisms involved, resistive switching implies the existence of two stable resistance states at least. When this minimum set is provided, the resulting *binary* RS device is described through a high resistance state (HRS) and a low resistance state (LRS), which are assigned, from the electronic standpoint, to 0 (OFF state) and 1 (ON state) logic values respectively. If a higher number of states is available, intermediate levels are defined according to the actual device performances [14]. State transitions are obtained by means of proper electrical stimuli, typically external voltages applied as ramps or pulses depending on the required operation mode [43]. The switching capability generally needs to be activated through the so-called electroforming process, also referred to simply as forming, which produces the first transition from the pristine state of the device to a higher conduction state. Once this is accomplished, full operability is achieved, and the device can hence be switched between its resistance states. When the switch occurs from a state of high resistance to a lower one, a SET transition is said to take place, while the opposite, namely a state variation from a low resistance level to a higher one, is called RESET. From the digital memories standpoint, these are also defined as write operation and erase operation resepctively. RS devices whose SET and RESET are obtained applying voltages with the same polarity are said to have a bipolar resistive switching behaviour. Otherwise, if SET and RESET have opposite polarity, the RS behaviour is called unipolar [50]. Figure 1.6 schematically summarizes both the behaviours as they

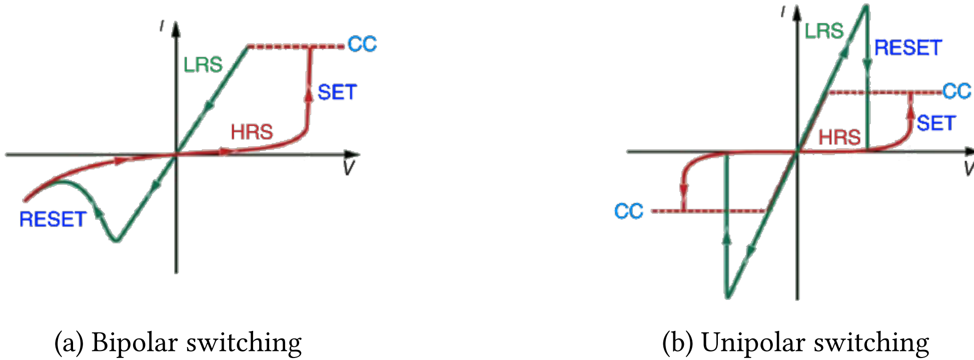

(a) Bipolar switching

(b) Unipolar switching

Figure 1.6: Schematic representation of typical *i*-*v* characteristics obtained applying voltage ramps. Adapted from [14]

can be typically observed in sweep mode applying voltage ramps. It also shows the effect of the so-called compliance current (CC or I_{CC}), which is the maximum value of current across the device imposed during the SET transitions in order to prevent critical endangering of RS reversibility, a phenomenon referred to as hard breakdown or stuck-at-one (SA1) error [14, 51, 52]. For the same reason, a compliance current is generally employed during the forming process too [53].
In nanoionics-based devices, the RS behaviour, as well as the resulting properties in terms of SET and RESET characteristics, can be ascribed to the consequential combination of ionic transport and redox reactions giving rise to the formation of a localized conductive filament (CF) within the insulating layer. Depending on the materials employed for the MIM structure, such conductive filament can arise as the result of either cation or anion migration [47]. In a simplified picture with the CF considered as the key player but treated like a black-box, the forming process of a nanoionics-based device can be described as an initialization step, required to *form* the conductive filament for the first time. Once the forming is achieved, the device is in the LRS, and a RESET is needed to switch it back into a less conductive state (HRS). This transition occurs through a partial dissolution of the CF that makes it no longer able to provide an electrical path of high conductivity between the two electrodes. Such interruption is recovered with a SET, that provides a restored conductive filament and hence brings the device again in a highly conductive state [54]. The three processes are schematized in Figure 1.7. Looking at the nature of the CF in more detail, nanoionics involved in its formation, partial dissolution and recovery takes shape in redox processes based on cation or anion migration depending on the materials of the MIM structure. In resistive switching devices employing an electrochemically active metal like silver or copper as one of the electrodes, the ionic drift induced by an applied voltage, and responsible for the RS transitions,

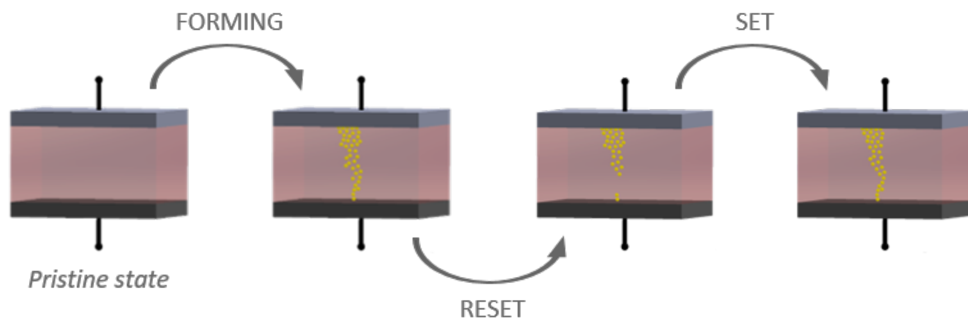

Figure 1.7: Schematic representation of filamentary resistive switching, with formation, partial dissolution and recovery of the CF

involves metal cations produced from the oxidation of the active metal. Such positive ions move towards the opposite electrode, which is made of an inert metal like platinum, and there undergo reduction. Following these redox reactions, metallic dendrites grow at the counter electrode where cations are discharged, building up the conductive filament [47] (see Figure 1.8). Due to this kind of metallization process taking place within the "I" layer because of electrochemical processes eventually bridging the electrodes, RS devices based on cation migration are generally referred to as programmable metallization cells (PMCs), conductive-bridge random access memories (CBRAMs) or electrochemical metallization (ECM) cells [55–57]. When cation migration from the electrodes is hindered because of "M" layers with high enough electrochemical potential with respect to 0.520 V and 0.7991 V of copper and silver respectively [58], ionic migration in nanoionics-based devices implies anion motion. This situation is also fostered by many oxides whose oxygen-related defects have a significantly higher mobility compared to foreign cations. The combination of inert electrodes with oxides prone to defects motion translates into a mechanism, called valence change memory (VCM) effect [59], relying on the drift of oxygen ions within the "I" layer. Such voltage-induced migration, generally described through the motion of oxygen vacancies (see Figure 1.9), produces local changes in the stoichiometry of the oxide, with the formation of oxygen-deficient regions and consequent valence changes in the cation sublattice [50]. As a result, the CF grows as a conductive phase of the oxide, which behaves as a moving virtual cathode until its expansion reaches the anode and a conductive path is created [47].
In both ECM and VCM cells, the dielectric film enclosed between the metal layers behaves like a solid electrolyte; seemingly a contradiction to its insulating properties. However, as pointed out in [60], no inconsistency arises in fact, due to the nanoscale

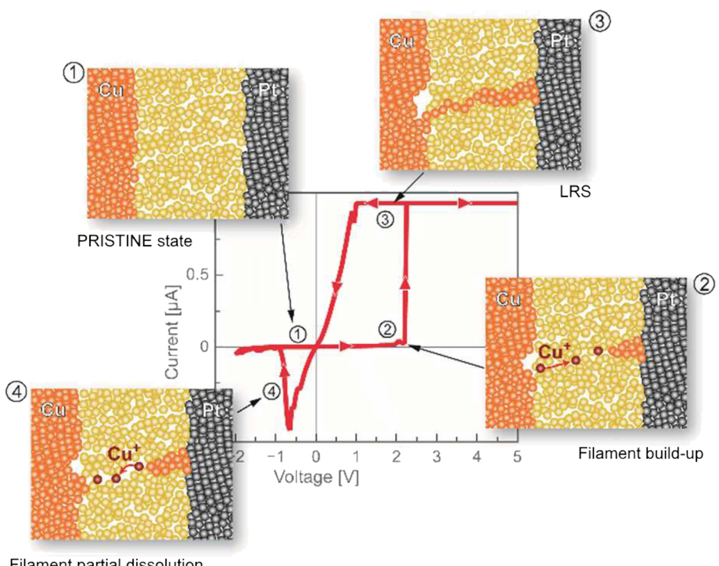

Figure 1.8: Summary of the electrochemical processes, and the corresponding *i*-*v* curve, of a typical ECM cell operating in sweep mode. Adapted from [60]

dimensions involved which turn out to be of the same order of magnitude as the Debye length [59, 61]. Furthermore, the nanometric film thickness leads, in presence of an applied voltage, to an electric field across the insulating layer of the order of $(10\div10^3)$ MV/m. With such values, the ionic drift velocity, defined as

$$v \approx fae^{-\frac{U_A}{k_B T}}\sinh\left(\frac{qEa}{2k_B T}\right) \tag{1.13}$$

can be approximated with an exponential equation:

$$v \approx \mu E_0 e^{\frac{E}{E_0}} \tag{1.14}$$

where $\mu = qfa^2\exp[-U_A/(k_B T)]$ is the mobility at small electric fields, q is the ion charge, f is the escape frequency, a is the periodicity of the net ion potential, U_A is the activation energy for ion hopping, k_B is the Boltzmann constant, T is the local temperature at the conductive filament, E is the electric field across the "I" layer and $E_0 = 2k_B T/(qa)$ is the characteristic field for the specific mobile ions [62, 63]. Given this relationship, ions can drift through a nm-sized dielectric film in a characteristic time that can be estimated as:

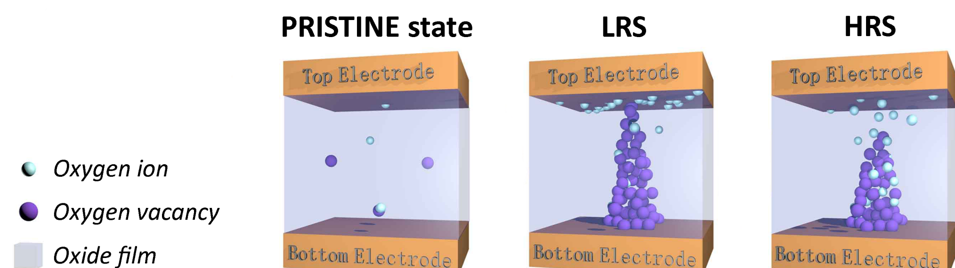

Figure 1.9: Schematic modelling of the CF in a VCM cell through oxygen vacancies migration. Adapted from [64]

$$\tau \approx \frac{d}{\mu E_0 e^{\frac{E}{E_0}}} \tag{1.15}$$

where d is the film thickness [62]. From (1.13), it is possible to recall the Mott-Gurney law for ionic transport:

$$j_{\mathrm{hop}} = 2qcfae^{-\frac{U_{\mathrm{A}}}{k_{\mathrm{B}}T}} \sinh\left(\frac{qEa}{2k_{\mathrm{B}}T}\right) \tag{1.16}$$

where c is the ion concentration. As for (1.13), the condition $E \gg E_0$ leads to an exponential relation:

$$j_{\mathrm{hop}} \approx 2qcfae^{-\frac{U_{\mathrm{A}}}{k_{\mathrm{B}}T}} e^{\frac{E}{E_0}} \tag{1.17}$$

From (1.16) and (1.17) it clearly appears that a dependence on both temperature and electric field affects the ion motion; and being the latter identified, in nanoionics-based devices, as a trigger for resistive switching through the CF formation, it eventually turns out that ECM and VCM mechanisms can be influenced by either electric field or temperature [65]. Concerning the latter, it is worth stressing that it refers to the effective temperature of the conductive filament, which is strongly affected by Joule heating during its build-up [63].

When ions move, a flow of mass and charge is produced and sustained only if the system can provide an ion source at the one end and an ion sink at the other end; otherwise, due to charge accumulation, an internal electric field arises and further motion of charged species is prevented. In both ECM and VCM RS devices, such requirement is fulfilled through the coupling of specific redox reactions, which take place depending on the materials the MIM cells are made of [14, 43, 50, 57]:

- the basic structure of an ECM-based device, made of an oxidizable electrode (M_1) playing the role of ion supplier, a solid electrolyte and an inert electrode (M_2) for ion reduction, allows the following half-reactions:

  anode: $M_1 \longrightarrow {M_1}^{z+} + ze^-$

  cathode: ${M_1}^{z+} + ze^- \longrightarrow M_1$

- in VCM cells, given the inert character of the electrodes, the role of ion supplier is played by the "I" layer of the MIM structure, typically a metal oxide, through the creation of oxygen vacancies:

$$O_O \rightleftharpoons \frac{1}{2}O_2(g) + V_{\ddot{o}} + 2e' \tag{1.18}$$

  where, following the Kröger-Vink notation [66], O_O represents an oxygen ion on a lattice site and $V_{\ddot{o}}$ identifies a doubly charged oxygen vacancy. Depending on the specific M-I interfaces of the cell, two scenarios are possible once oxygen vacancies are created and they migrate:

  - in presence of noble metal electrodes, the ionic current is blocked at the M-I interfaces, and local valence changes in the metal ions of the oxide take place to prevent the formation of space charge regions;
  - if the electrodes are made of non-noble metals, oxidations occur at the M-I interface.

Forming, SET and RESET in ECM cells

Due to the presence of an electrochemically active metal whose cations must be able to drift toward the opposite, inert electrode, the "I" layer of ECM cells must be an ion conductor. Given this property, by applying a sufficiently high, positive voltage at the active electrode, it is possible to induce anodic dissolution and consequent ionic migration towards the counter electrode. Being the latter made of an inert metal, cations undergo reduction and electro-crystallization, thus producing metallic dendrites that grow within the "I" layer until the two electrodes are electrically bridged. When this happens, the CF is formed and the device is in the LRS. In order to produce a RESET transition, a negative voltage at the active electrode is needed. The effect is a Faradaic current inducing partial dissolution of the CF and the consequent rupture of the conductive bridge, that switches the device into the HRS. Applying again a positive voltage

at the active electrode, a process similar to forming is induced and a SET transition is obtained, thanks to the recovery of the conductive filament leading again to the LRS. [57, 67–69].

Forming, SET and RESET in VCM cells

As aforementioned, the basic structure of a VCM cell consists of an insulating layer enclosed between two inert metals. Generally, the insulator is a metal oxide and at the interface with one of the electrodes a Schottky barrier arises; while an ohmic contact is typically created with the other metal. Upon the application of a sufficiently high voltage at such MIM system, usually larger than the following SET and RESET voltages, a localized reduction of the "I" layer gives rise to the conductive filament. Growing as an oxygen deficient region, once it is formed, it provides electrical connection between the electrodes. Subsequent SET and RESET transitions take place as the result of the modulation of the oxygen ions (vacancies) content in the CF. Such process may occur close to the interface between the oxide and the electrode with lower oxygen affinity or, more generally, in the region where the formed filament is narrower. With SET, oxygen ions (vacancies) are removed from (injected to) the CF, while the opposite happens during RESET [49, 70–72].
Besides the filamentary mechanism shown by most of the VCM cells, an interface-type RS is possible too. When an external voltage is applied, the M-I interface where the Schottky contact is established undergoes, as a consequence of the external field, a modulation of the barrier height. Due to the ionic migration, indeed, charges can accumulate and modify the potential profile at the Schottky interface, thus inducing changes in the contact resistance that allow subsequent transitions between HRS and LRS [50, 73–76].
Becuase of the specific characteristics of these two mechanisms, VCM cells may show or not a dependence on the device dimensions. When resistive switching is of filamentary-type, being conduction confined in a localized CF, the RS properties are independent of the cell size, while they are affected by the area of the Schottky contact when an interfacial mechanism dominates [77].

1.2.3 Resistive switching devices as digital memories

Computers can be thought of as machines transferring data back and forth from a storage block to a processing unit [78]. With an oversimplified description, this is the idea the von Neumann architecture is based on [79]. Composed of five operational elements assigned to as many functions, namely control, arithmetic-logic, memory, input and output, it relies on the execution of instructions to process data by the so-called

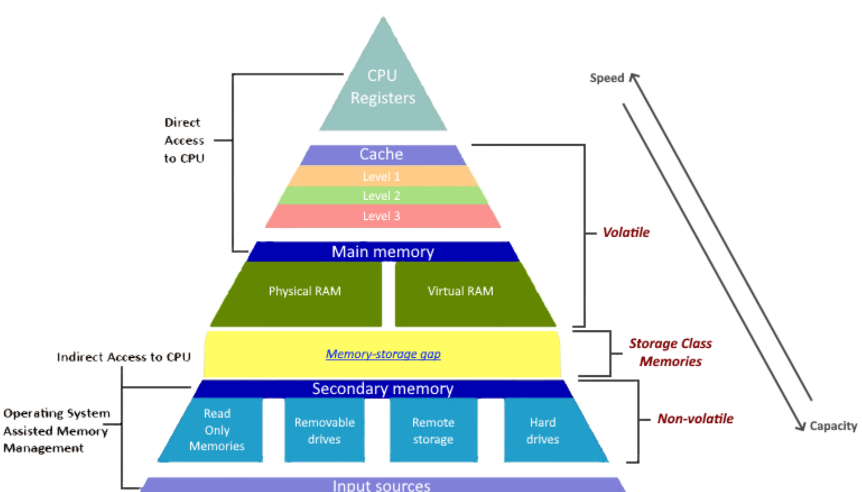

Figure 1.10: Schematization of the memory hierarchy. Connections between units and levels from the CPU to the external input sources are summarized

central processing unit (CPU), which embeds control and arithmetic-logic units. Such instructions, as well as data, are fetched by the CPU from the main memory block, the so-called random access memory (RAM). In order to make this process as fast as possible, cache memories, tasked with bringing specific portion of the needed program data, are employed between the CPU and the RAM. Caches are differentiated according with the capacity and the access time they provide. In the so-called memory hierarchy, higher cache levels correspond to smaller but faster memories [80]. As schematically summarized in Figure 1.10, the same hierarchical order holds for the whole memory subsystem of a computer. From the top downwards, the distance from the CPU increases as well as the capacity of the memory, while the speed decreases. Caches are generally made of static RAMs (SRAMs), whose basic cell is composed of two CMOS inverters and two access transistors. The latter are used to set the cell state, that depends on stored charges (Figure 1.11a). A similar mechanism is employed by the dynamic RAMs, (DRAMs) that constitute the main memory. Compared to SRAMs, they also are non-volatile memories but they provide a higher density, thanks to a simpler structure made of a capacitor in series with a transistor (Figure 1.11b). Additionally, as their position in the memory hierarchy suggests, DRAMs are slower than SRAMs. Historically, the first level of non-volatile memories was the one identified as secondary memory and aimed at storage. There, a third kind of charge-based mechanism is employed by the Flash memories, that guarantee non-volatility storing charges in floating gates (Figure 1.11c) [81–83]. Alternative to this class of semiconductor memories are the magnetic hard drives, well

established and widely diffused but affected, as pointed out also by the 2020 International Roadmap for Devices and Systems (IRDS), by possible mechanical failures, high energy consumption, long access time and large form factor [84].
Following the increasingly more severe requirements in terms of density, storage capacity and operating speed for memory devices, the existence of a gap in the memory hierarchy between the DRAMs (i.e. the main memory level) and the Flash memories (namely the secondary memory level) has become clear in last years. Such empty space, also referred to as the memory-storage gap, highlights the lack of, and the need for, a new class of devices, named storage class memories (SCMs), providing high speed, a storage density comparable to that of DRAMs and the non-volatility ensured by Flash memories [86–89]. The space of SCMs can be in turn subdivided into two levels [84]:

1) memory-type SCM: as fast as needed to be synchronous with a higher level memory and able to provide non-volatility over a period of few days up to few weeks;

2) storage-type SCM: faster than a Flash memory but with the same non-volatility.

Despite some practical challenges and issues not yet overcome, ReRAMs are considered as possible candidates as SCMs to fill the gap between DRAMs and Flash memories [90, 91]. Specifically, ReRAMs could provide a twofold solution. On the one hand, they allow to overcome the scaling limitations inherently affecting all the charge-based memories, as storing information in form of resistance states avoids charge leakage phenomena typical of the advanced technological nodes. On the other hand, they can open the way to highly efficient in-memory computing and break the so-called memory wall.

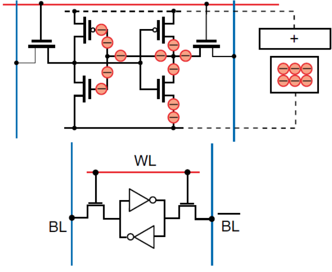

(a) SRAM cells are made of two access transistors and as many inverters connected back to back.

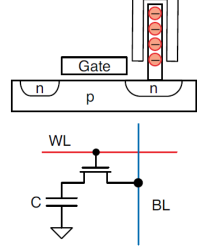

(b) A DRAM cell contains only one transistor and a capacitor, connected in series, acting as storage node.

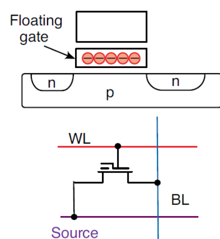

(c) Flash memories are based on a single transistor, and the storage node is associated to the floating gate.

Figure 1.11: Scheme of the cell structure and of the charge storage for SRAMs, DRAMs and Flash memories. Adapted from [85]

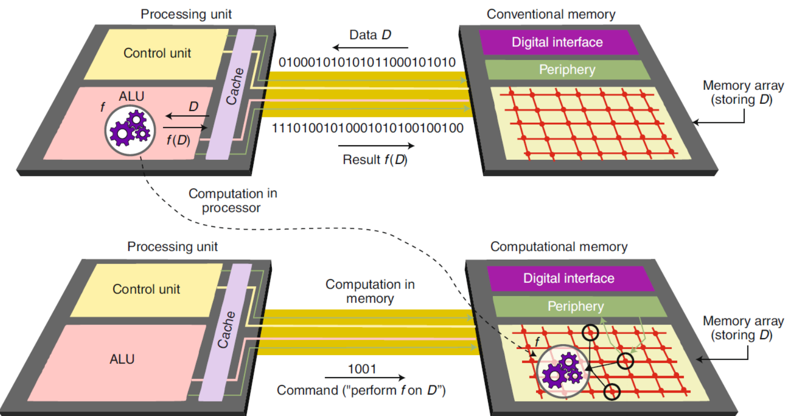

Figure 1.12: In-memory computing consists in performing computational tasks ($f(D)$) without moving data (D) back and forth from the memory unit to the processing unit. Adapted from [85]

Performing computation in the same site where data are stored, would indeed strongly reduce both time and power required for data transmission, thus overcoming the von Neumann bottleneck [83, 85, 92, 93].
In order to assess resistive switching devices in the domain of digital memories, and to identify benchmark values for comparisons, a set of fundamental parameters, or figures of merit, must be introduced to define a specific metrics [14, 91]:

- *resistance levels:* R_{HRS} (or R_{OFF}) and R_{LRS} (or R_{ON}) represent the resistance values for the high resistance state and the low resistance state respectively;
- *ON/OFF ratio:* also referred to as *resistive window (RW)*, it is evaluated as the ratio between the HRS resistance level and the LRS one;
- *switching voltages:* together with the forming voltage V_{FORMING}, the V_{SET} and V_{RESET} values represent the voltages need to induce state transitions;
- *switching time:* also referred to as *switching speed*, it provides information about the time required to achieve a SET or RESET transition. In the first case, it is also named as *write time* or *SET time*, while for RESET it can be referred to as *erase time* or *RESET time*;
- *endurance:* it measures the number of switching cycles before failures;
- *retention:* it quantifies how long a resistance state is preserved;

- *switching energy:* it represents the amount of energy required to change the resistance state.

Besides providing information suitable for performance comparison between different RS devices, some of these parameters are employed to quantify the capability of ReRAM technology as successful candidate for the SCM space. Table 1.1 shows an example of comparison with DRAMs and Flash memories [94], summarized in Figure 1.13 too.

Table 1.1: Benchmarking of ReRAM compared to DRAM and Flash technologies [94]

Technology	State defining particle	Particles per cell (in a 20 nm cell)	State change barrier energy (eV)	Cell switching energy (pJ)	Energy efficiency	Switching time (ns)
DRAM	electron	~ $5{\cdot}10^4$	0.55	~ 0.001	> 0.8	< 10
Flash (3D NAND)	electron	~ 10^{-4}	0.2 ÷ 1.1	~ 0.01	> 0.8	> 10^4
ReRAM	metal/oxygen ion	10 ÷ 1000	1.4 ÷ 1.8	~ 10	~ 10^{-4}	10 ÷ 100

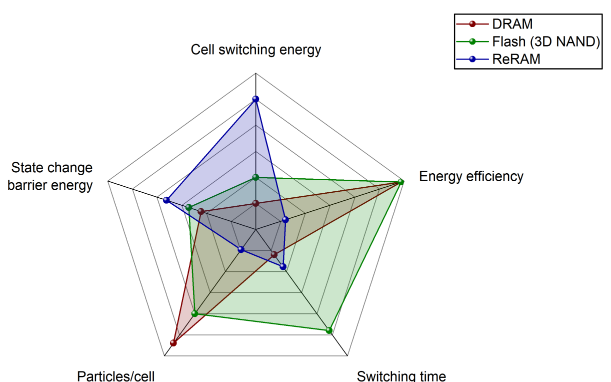

Figure 1.13: Data from Table 1.1 mapped onto a Kiviat diagram

1.3 Future applications and perspectives

As it is clear from our everyday life, computers and, generally speaking, smart-systems and devices, are becoming more and more similar to intelligent objects. Nonetheless, their improving capabilities in performing complex tasks, typically experienced by the user as voices and faces recognition but spanning to much more complicated

operations like images or music creation [95–99], actually hide severe difficulties. Differently from brain, indeed, computer chips cannot perform computation in the same place where they store information. Consequently, every time we talk to our smartphone, tablet, or any other smart-object, asking for something, somewhere else huge servers are dealing with the computational operations needed to produce the precise and correct answer we wait for. A possible solution to really make our devices intelligent is neuromorphic computing: a different, brain-inspired, architecture based on the idea that neuron-like and synapse-like devices can build a network in which physical separation between storage and computation is not needed [100, 101].
With more than 10^{11} neurons and 10^{15} synapses, human brain manages information storage and processing through the mechanism of synaptic plasticity, namely the activity-dependent change of the neuronal connections established by synaptic transmissions [102–104]. In order to replicate or, at least, to emulate it, RS devices, also those acting as memristive devices, and hence able to provide multiple levels or even analog responses, can be employed as either neurons or synapses [64, 105–113]. Furthermore, their built-in suitability for in-memory computing and the high scaling potential open the way to highly energy efficient and parallel systems able to perform advanced cognitive tasks [114]. Thus, in view of a near future characterized by challenging requirements like increasing computational complexity, enhanced learning capability and improving energy efficiency, RS devices stand up as a possible response able to provide solutions in fields like big data analysis and internet of things (IoT) [115, 116].

1.4 Thesis outlook

In this Thesis, studies on resistive switching devices relying on the VCM effect are presented, adopting different perspectives to accommodate to the specific properties of the investigated systems. The attention is especially focused on two metal oxides as resistive switching materials: zinc oxide (ZnO) and hafnium dioxide (HfO_2).
In **Chapter 2**, after a brief overview of these materials from the angle of their relevance in scientific literature, the fabrication processes are reviewed. For each oxide, the choices made concerning the device fabrication are explained in terms of both the material properties and the technological possibilities, and all the steps are reported with technical and operational details.
Afterwards, in **Chapter 3**, the adopted characterization methodologies are presented, focusing on the main results concerning the material properties. The different vantage points for ZnO and HfO_2 are highlighted, further clarifying the specific objectives in the device characterization according to the metal oxide employed.
Chapter 4 is then devoted to the devices based on zinc oxide. After a short introduction about the commonly known, and widely exploited, material properties, resistive switching in zinc oxide thin films is discussed through a comparative analysis of the ECM and the VCM mechanisms. Focusing on this latter, its filamentary nature is then discussed, with results obtained through conductive atomic force microscopy measurements. Finally, the improvements obtained in terms of device performances through the adoption of zinc oxide nanowire arrays hydrothermally grown on top of ZnO thin film are discussed, with a particular focus on the role played by the nanowires as oxygen vacancies reservoir.
Properties and performances of the HfO_2-based devices are instead presented in **Chapter 5**. There, the impact of titanium-based buffer layers is analysed, investigating the effect of finely designed variations in the fabrication process starting from a reference device structure. Filamentary resistive switching is shown by means of conductive atomic force, as for the ZnO-based devices, and by a statistical analysis. Then, the oxidizing activity of titanium, and its impact on the oxygen vacancies dynamics, is proposed and discussed as the reading key for the results of electrical tests performed in different operational regimes.

Chapter 2

Device fabrication

Starting from the silver and nickel metallic filings studied by Prof. Calzecchi-Onesti, different materials have been investigated for resistive switching devices, exploring a variety of forms ranging from thin films to one-dimensional nanostructures [117–122]. In this Thesis, the attention is focused on the effect nano-structural engineering can have on metal oxide thin films and on which advantages it can provide acting on the physics of the RS mechanism involved. To do so, two metal oxides have been considered, based on their peculiarities not only from the physical standpoint but also from a technological viewpoint. Despite a common target, namely an enhanced control of oxygen vacancies dynamics in VCM-based resistive switching devices, different engineering approaches have been adopted in fact, according to the choice of the most suited processes for each material.
At first, zinc oxide (ZnO) has been investigated. Well known and widely employed, ZnO offers a broad spectrum of processing techniques and a large number of possible nanostructures [123–125]. Additionally, it generally ensures a cost effective fabrication, meeting the need for low cost devices especially in view of possible integrations with other electronic systems for large-scale production. Secondly, hafnium oxide (HfO_2) has been employed. Similarly to ZnO, HfO_2 also is a widely employed material. Thanks to its high dielectric constant (25) [126], indeed, hafnium oxide has been highly successful as gate insulator for CMOS (complementary metal-oxide-semiconductor) MOSFETs, and this made it readily available when resistive switching devices gathered again the interest of the scientific community [127, 128].
Both materials have been deposited as thin films for MIM structures through well established processes, and what differentiates them from one another is the approach

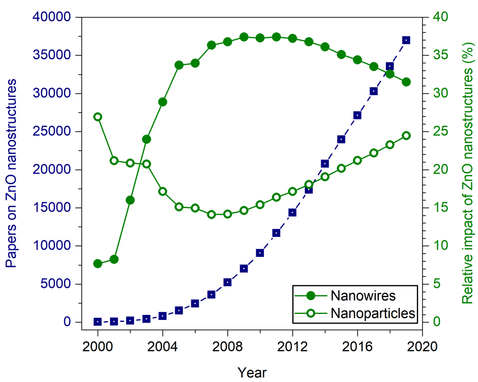

(a) Since 2005, nanowires cover more than 30% of publications on ZnO nanostructures. For comparison, data for papers focusing on ZnO nanoparticles are shown.

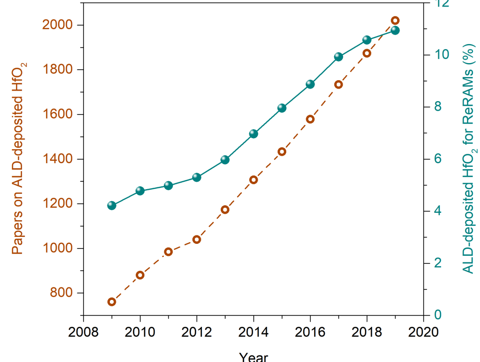

(b) Along with the increasing interest in resistive switching, ALD processes for HfO_2 have been attracting growing attention since 2009.

Figure 2.1: Data from Scopus about publications on ZnO nanostructures and HfO_2. Partial data for 2020 have been omitted

adopted to engineer the resulting thin-film-based devices. While for ZnO the possibility of producing a variety of nanostructures led to the fabrication of vertical nanowire (NW) arrays, in HfO_2-based devices the planar geometry was preserved and an additional metal thin film was deposited as buffer layer. Therefore, while zinc oxide allowed to induce some modification in the device physical behaviour taking advantage of its structural properties during the fabrication steps, hafnium oxide forced the introduction of a different material able to properly interface with it and to provide specific tuning capabilities regarding the device performances. Differently said, with ZnO it was found that its resistive switching properties can be tuned by playing with the nanostructures it can form, while the RS behaviour of HfO_2 can be modified only through its pairing with proper auxiliary materials.

2.1 ZnO-based devices

As anticipated, both the ZnO-based devices and the HfO_2-based ones have been fabricated to investigate suitable ways to achieve an enhanced control on the oxygen vacancies dynamics in VCM RS devices. As a consequence, all the MIM structures produced are based on metal layers characterized by electrochemical potentials high enough to avoid the cation electro-migration and the electrode partial dissolution typical of the ECM mechanism.

2.1.1 ZnO thin films

Starting from Si/SiO_2 wafers, the bottom electrode (BE) of the MIM structures was prepared by sputtering deposition of a tantalum-platinum bi-layer by means of a Kurt J. Lesker PVD 75. With a base pressure of 10^{-4} Pa, Ta at first was sputter-deposited with a DC power density of 7.4 W/cm^2 in a pure Ar atmosphere, then Pt DC sputtering was performed with a power density of 5.9 W/cm^2. The reason for such a bi-layered BE is the adhesion promotion of Pt on SiO_2 given by tantalum; indeed, from the RS MIM structure viewpoint, the role of inert bottom electrode is played by platinum only. The as-deposited $Si/SiO_2/Ta/Pt$ stack was then heated up to 50 ℃ before starting ZnO deposition. The latter was performed by RF magnetron sputtering with a power density of 1.2 W/cm^2. Finally, platinum deposition was performed again to close the MIM structure. This last step was performed by DC sputtering as for the BE, but a shadow mask was employed to obtain circular top electrodes (TEs).

2.1.2 ZnO nanowires

Nanowires are one of the most investigated ZnO nanostructures, as it can be appreciated, in Figure 2.1a, looking at their relative impact on the total number of papers dealing with zinc oxide nanostructures. They can be grown adopting different methods, and the most commons ones turns out to be chemical vapour deposition (CVD) and hydrothermal growth [129]. Here, the latter has been considered. As reported in [130], the same $Si/SiO_2/Ta/Pt$ substrates as for the above mentioned devices based on ZnO

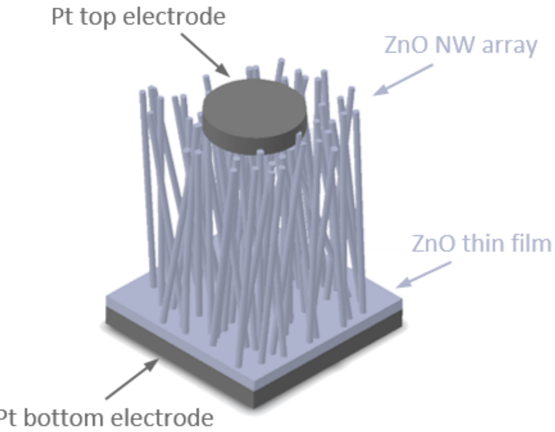

Figure 2.2: Sketch of a ZnO-based device with a ZnO nanowire array grown on top of the zinc oxide thin film

thin films were prepared as first step. After that, a zinc oxide layer with thickness of 80 nm was sputter-deposited on top of it, playing in this case the role of seed layer for the subsequent nanowire growth. The resulting samples were immersed for two hours in a solution of zinc nitrate hexahydrate ($Zn(NO_3)_2{\cdot}6H_2O$), hexamethylenetetramine (HMT), ammonium hydroxide (NH_4OH) and polyethyleneimine (PEI) in bidistilled water. Temperature was kept at 88 ℃ and a slight magnetic stirring was continuously performed. After growth, the samples were rinsed with bidistilled water and dried by a nitrogen flow. As for the devices based on ZnO thin films, top electrodes were deposited by platinum sputtering through a shadow mask.

2.2 HfO_2-based devices

It has been mentioned previously that HfO_2 turned out to be a well known material, especially from the technological viewpoint of the fabrication processes, already at the time in which the lens of ReRAM research stopped over it. As a consequence, details on the possible deposition methods have been available in literature since the beginning of the investigation of hafnium oxide as ReRAM-suitable material [131–134], allowing a quickly increasing employment in RS devices especially through atomic layer deposition (ALD). Figure 2.1b shows indeed that since 2009, namely immediately after the breakthrough year (see Figure 1.1a), the relative impact of ReRAM-related publications on the total number of papers dealing with ALD-deposited HfO_2 has been unceasingly growing. Coherently with such trend, in this Thesis, hafnium oxide films have been deposited by means of ALD to fabricate ReRAM cells.

2.2.1 Crosspoint ReRAM cells

The investigation on resistive switching in HfO_2-based devices has been carried out in two complementary ways. On the one hand, devices with a complete MIM structure have been fabricated in order to test the electrical performances; on the other hand, cells with the same structure but with a single electrode have been prepared to locally investigate the device responses through a movable electrode. In the first case, a crosspoint geometry has been adopted for each ReRAM cell (see Figure 2.3). As for the ZnO-based devices, Si/SiO_2 wafers were used as substrates and platinum was employed as bottom electrode. By means of a Pfeiffer Spider 600, a Ti/Pt double layer was sputter-deposited as electrode layer, with 5 nm and 125 nm of thickness respectively. Photolithography was then performed to pattern the BEs, followed by dry etching thourgh an STS Multiplex ICP etcher. In order to electrically isolate the as-defined metal pads one from

another, a low pressure CVD (LPCVD) process was subsequently performed to deposit a 100 nm thick low temperature oxide (LTO) at 425 °C. Once the bottom electrodes were patterned and isolated, a second step of photolithography, followed by buffer oxide etch (BOE), was carried out to open vertical interconnect accesses (VIAs) through the LTO passivation layer. Such openings, designed with a circular geometry and different diameters, were aimed at defining the active region of each cell, namely the device area where to build the actual MIM structure. With this step, indeed, through holes were opened in the LTO, thus allowing deposition directly on top of the BEs in well defined, localized and regularly arranged regions. There, a HfO_2 layer was deposited first, with a thickness of 5 nm, by means of a BENEQ TFS200 ALD system. Afterwards, depending on the sample, titanium-based films of different thicknesses and compositions were sputter-deposited as buffer layers. By means of an Alliance Concept DP650, sputtering was performed employing a pure (99.9995%) Ti target or a mixed titanium-tungsten one, with the latter having 99.99% of purity and 10% in weight of Ti. Once the buffer layer was deposited, the top electrodes were defined. Employing the same sputtering tool, tungsten and titanium nitride were deposited. The former, with thickness of 60 nm, playing the actual role of TE, the latter, 15 nm thick, acting as capping layer. The final electrode patterning step was then performed by photolithography and subsequent dry etching with the STS Multiplex ICP dry etcher.
The complete process flow, with additional details for each step, is reported in Appendix A.

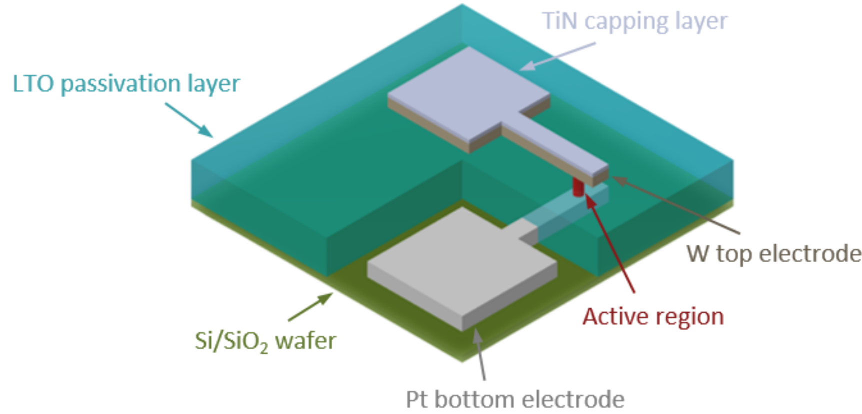

Figure 2.3: Sketch of a crosspoint ReRAM cell with highlights on the key elements of the fabrication process

2.2.2 Single-electrode ReRAM cells

As explained in [135], single-electrode devices were fabricated as a variant of the crosspoint cells, obtained reverting the structure without changing it. All the layers were indeed the same as in the previous scheme, but in an upside down fashion. The only exception was the Pt electrode, that was replaced by a movable one as it will be described in the following. The first layer deposited on top of Si/SiO_2 wafers hence was the tungsten electrode, obtained by sputtering with a thickness of 300 nm. Then, VIAs with the same geometry and size as for the crosspoint cells were opened through the passivation layer deposited on the BE. Afterwards, sputter-deposition was performed again for the buffer layers, employing the same machine, the same targets and the same parameters as previously described. The unique relevant difference compared to the process flow adopted for the crosspoint cells, allowed by the absence of TEs to be patterned, was at this point, with the employment of a shadow mask for the buffer layer deposition. As final step, the HfO_2 film was deposited, again by ALD and with the same thickness of 5 nm.

Chapter 3

Characterization methodologies

Resistive switching devices hide the profound nature of their behaviour behind a complex interplay of processes. Especially in nanoionics-based devices, physical, electrochemical and thermochemical phenomena concur and indissolubly combine to produce the ultimate RS behaviour. In order to carry out appropriate investigations, it is therefore mandatory to probe different aspects employing the most suited techniques. As carefully reviewed in [136], a number of tools exist to specifically target the study of

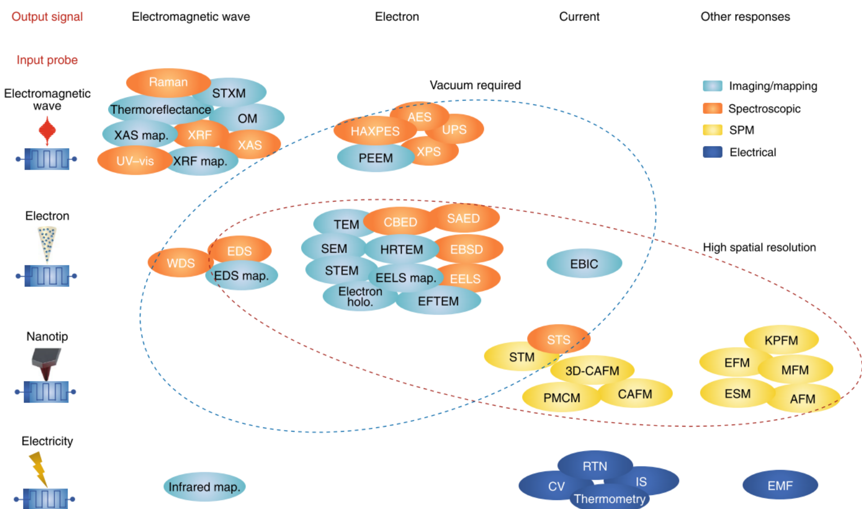

Figure 3.1: Classification of the characterization techniques available for RS investigation proposed in [136]

resistive switching, and Figure 3.1 summarizes and clusters them according to the probing mechanism and the output signal they are based on. A key message immediately delivered by such classification is the multi-domain extent of RS investigation: imaging, spectroscopy techniques, scanning probe instruments and electrical testing are all suited to collect information from RS devices, either from the material properties standpoint or to focus on performance analysis.
The characterization techniques employed in this Thesis are discussed hereinafter, with a primary focus on the results concerning material characterizations in this chapter. The electrical investigation and the resulting findings on device performances are then reported in more detail in following dedicated chapters.

3.1 ZnO-based devices

Due to the different structures employed for the ZnO-based devices, namely thin films and nanowires, morphological characterization was the preliminary step for the investigation and the overall comprehension of the effects of nanostructural engineering. To this aim, field-emission scanning electron microscopy (FESEM) was employed for both thin films and nanowire arrays. Figure 3.2 shows a cross-section image of a ZnO thin film, and the same picture is reported by Figure 3.3, with false colours, to highlight the upper layers of the Si/SiO_2/Ta/Pt substrate. In the same way, FESEM images of the nanowires are presented in Figure 3.4 and Figure 3.5. In the latter, false blue colour has been employed to highlight the platinum TE deposited on top of the NW array. This allows to visualize the level of in-depth penetration of Pt during the top electrode deposition. Being the NWs vertically aligned, possible channelling effects throughout the whole array were indeed a major concern of the fabrication process, since they could

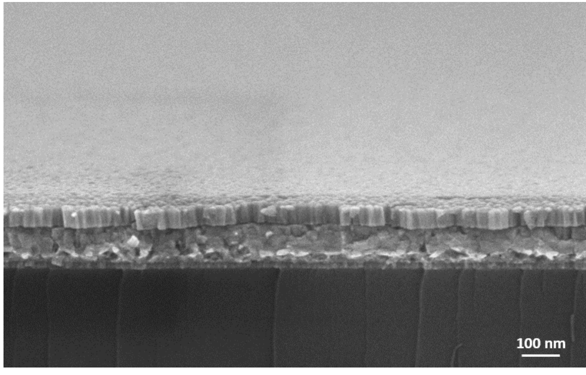

Figure 3.2: FESEM cross-section image of a ZnO thin film

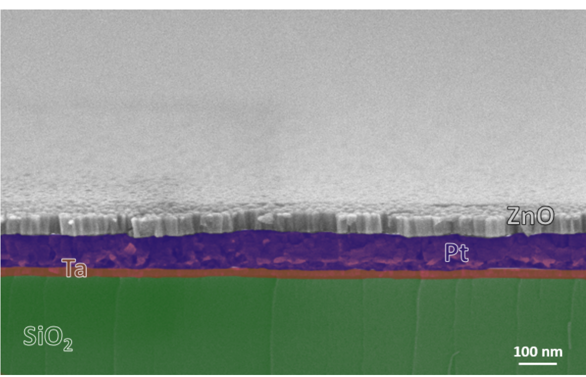

Figure 3.3: By means of false colours, the different layers are highlighted in the cross-section picture of a ZnO thin film

produce a continuum of platinum resulting in the electrical connection between bottom and top electrode. Thanks to the high density and uniformity resulting from the growth process carried out for the NWs (see Figure 3.6 and Figure 3.7), the Pt TE actually turned out to be well defined, and confined, in an uppermost layer of the nanowire array. This key observation was confirmed by X-ray photoelectron spectroscopy (XPS) too.
Aimed at providing compositional information, XPS offers different kinds of analysis like depth profiles and high resolution spectra. In the first case, samples are probed in depth to investigate which elements they contain, while the second type of analysis provides insights on the chemical bonds, and hence the surrounding environment, of such elements. Figure 3.8 shows the XPS depth profile of a nanowire array. The presence of two clear peaks ascribable to platinum and corresponding to the top and the bottom electrode, together with the fall down to zero of the Pt signal between them, validates

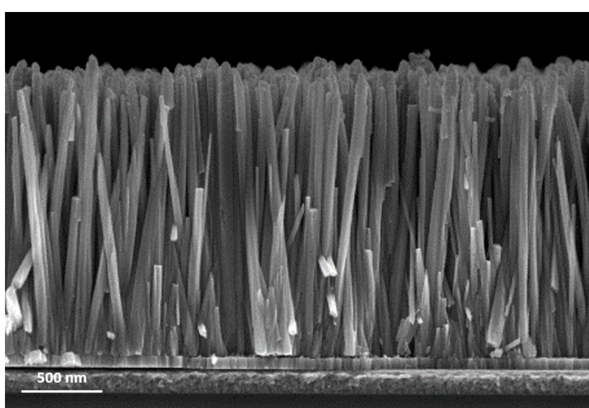

Figure 3.4: FESEM cross-section image of a ZnO nanowire array

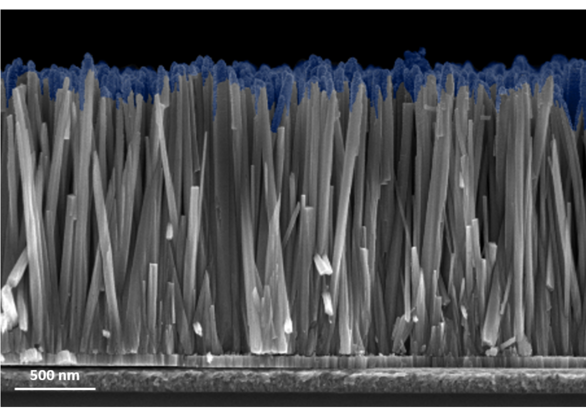

Figure 3.5: The Pt top electrode is well defined on top of the NWs, without significant deposition across the array

the observation made by FESEM cross-section images: during the sputtering deposition of the top electrode, platinum did not penetrate across the nanowire array, thus remaining in the upper part of the NWs. The XPS depth profile also provided another relevant information, namely a slight ZnO understoichiometry throughout the NW array. The same analysis was performed on thin films, showing, as it is reported in Figure 3.9, a less apparent understoichiometry pointed out by a reduced lack of oxygen across the ZnO layer. In order to further investigate this point, high resolution spectra of the oxygen 1s orbital were analysed. As thoroughly explained in [130], the O 1s peak in ZnO can be decomposed in three components. Carrying out a fitting procedure based on Gaussian-Lorentzian functions, after Shirley's background subtraction, the three contributions were identified as reported in Figure 3.10 and Figure 3.11 for thin films and NW arrays

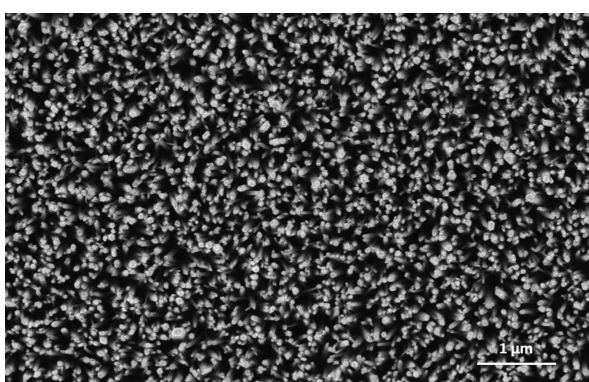

Figure 3.6: Top-view by FESEM characterization of a nanowire array

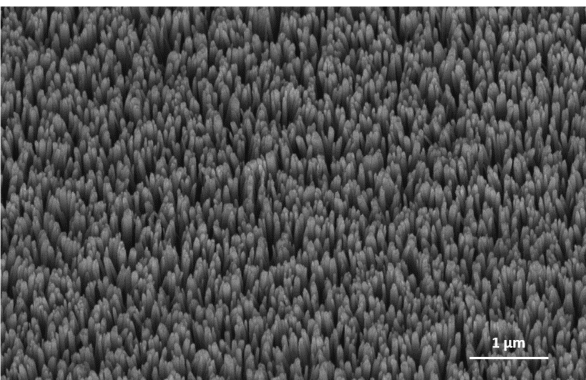

Figure 3.7: FESEM image of a nanowire array with a 30° tilt with respect to the top-view

respectively. The main component (O_a), located at 530 eV, comes from the O^{2-} ions surrounded by the Zn^{2+} ones, while the O_b component at 531.6 eV results from O^{2-} ions whose chemical environment within the crystalline structure of ZnO is characterized by oxygen deficiency. Concerning then the third component (O_c) at 532.8 eV, it can be assigned to hydroxyl groups due to ambient exposure of the samples [137–142]. Following this analysis, it can be observed that the less significant ZnO understoichiometry of thin films matches with a larger relative area of the O_a component in the O 1s peak: 73.09% instead of 68.90% in the NW arrays. Furthermore, the smaller relative area of

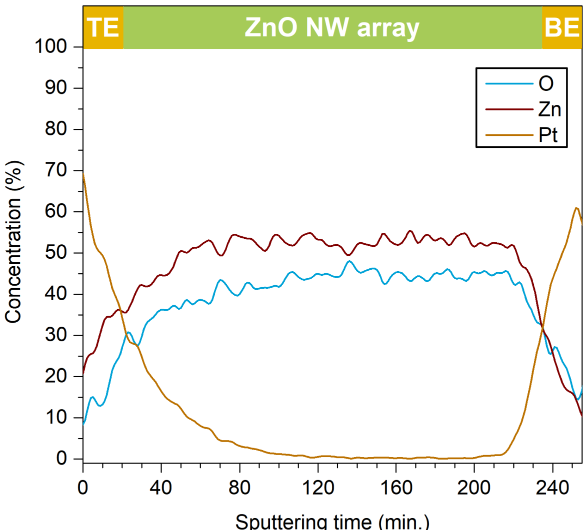

Figure 3.8: The XPS depth profile of the NW array highlights a good confinement of the Pt TE on top of the NWs and a slight ZnO understoichiometry within the array

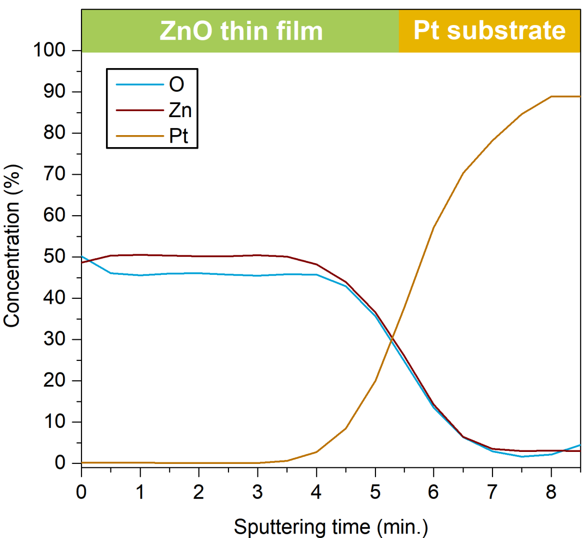

Figure 3.9: Good stoichiometry of the ZnO thin film reported by the XPS depth profile

the O_b component in the case of thin films results in an O_a/O_b area ratio 12.5% larger with respect to the NW arrays. Consequently, since O_a labels the contribution to the O 1s peak coming from O^{2-} ions with by the Zn^{2+} surrounding, while O_b identifies the component related to O^{2-} ions in oxygen deficient regions, it clearly turns out that thin films exhibit a lower concentration of oxygen vacancies.

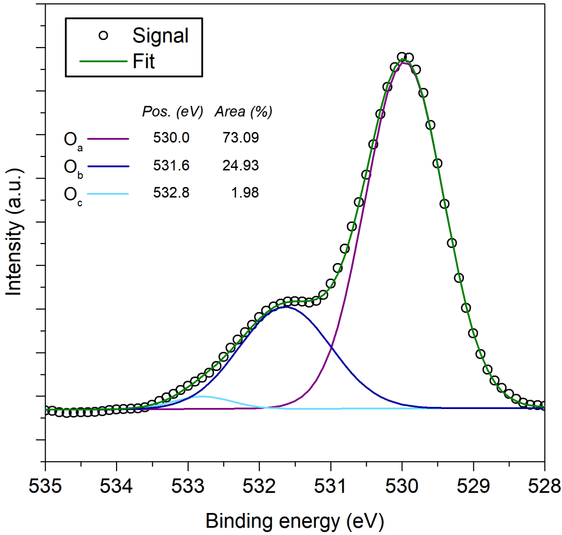

Figure 3.10: Fit and analysis of the O 1s peak in ZnO thin films

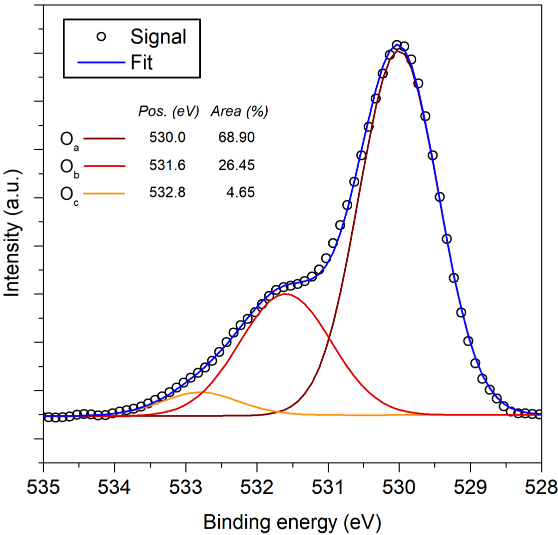

Figure 3.11: Fit and analysis of the O 1s peak in ZnO nanowire arrays

The presence of defects was investigated by means of Raman spectroscopy too, which also revealed typical features of the ZnO wurtzite phase [130, 143]. Figure 3.12 and Figure 3.13 show the Raman spectra acquired for thin films and nanowire arrays respectively. In both cases, Lorentzian functions were employed to decompose the overall signal into individual contributions. The main component of the two spectra comes

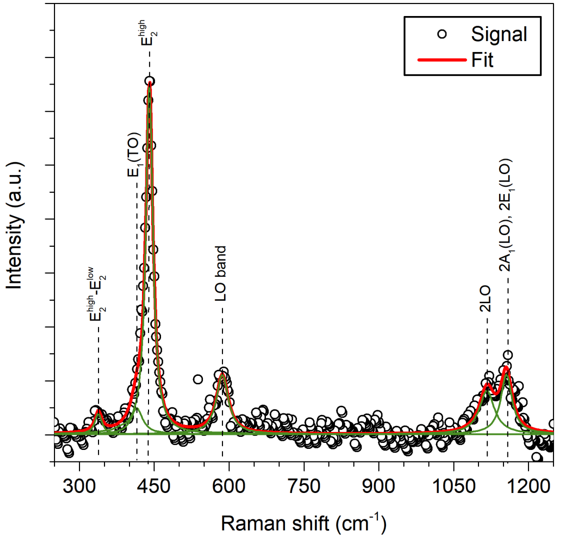

Figure 3.12: Raman spectrum of ZnO thin films

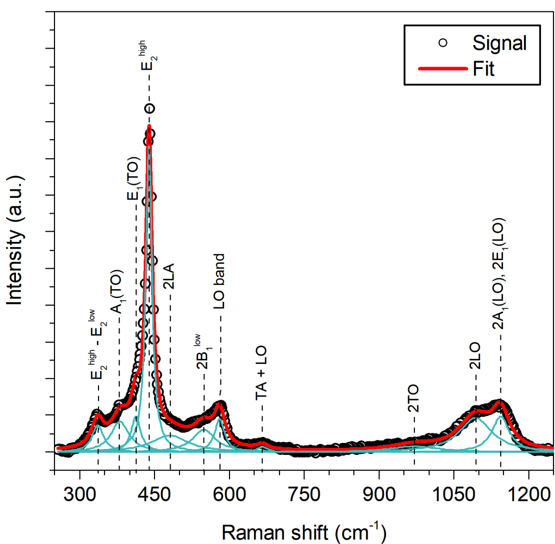

Figure 3.13: Raman spectrum acquired for nanowire arrays

from the non-polar E_2^{high}, which mainly involves the motion of the O sublattice. For the ZnO thin films, this peak was located at 440 cm^{-1}, while it was placed at 440 cm^{-1} in the case of nanowire arrays. The second major contribution, located at 586 cm^{-1} for the thin films and at 580 cm^{-1} for the NW arrays, is instead related to the superposition of the A_1(LO) and the E_1(LO) modes, which have close wavenumbers and are typically identified as a unique LO band. Finally, relevant contributions come from second order modes in the high frequency region of the spectra, with optical phonons producing peaks at 1116 cm^{-1} and 1155 cm^{-1} in the case of thin films and at 1093 cm^{-1} and 1144 cm^{-1} in NW arrays [144–149]. In [130], it is also reported that Raman spectroscopy was employed to assess the ZnO crystal quality of the NW arrays through a comparison of the E_2^{high} peak width with the case of CVD-grown nanowires. With a full width at half maximum (FWHM) of 15.0 cm^{-1}, instead of 9.7 cm^{-1} as for the CVD NWs, the E_2^{high} peak revealed a poorer crystallinity of the hydrothermally grown arrays.
In order to collect further crystallographic information, X-ray diffraction (XRD) analysis was eventually performed, comparing the acquired results with data of ZnO powder (from JCPDS 89-0511). Figure 3.14 shows the XRD pattern obtained for thin films. The prevailing peak at 34.1° can be ascribed to the [002] direction, and, together with the diffraction peak at 35.7° related to the [101] direction, it reveals the presence of the ZnO wurtzite phase. The additional peak at 33° comes instead from the underlying silicon [143]. The XRD pattern for nanowire arrays is then reported in Figure 3.15. In this

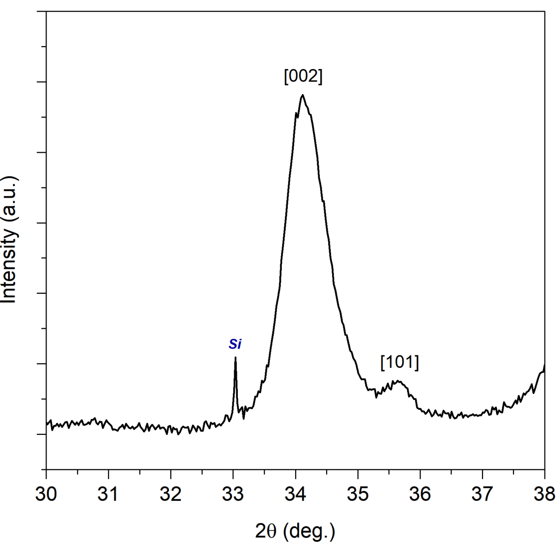

Figure 3.14: XRD pattern showing evidences of the wurtzite phase in ZnO thin films

case, the only and extremely narrow peak observed is the one, at 34.5°, due to the preferential growth of ZnO NWs along the [002] direction, which corresponds to the c-axis of the ZnO wurtzite phase [130].

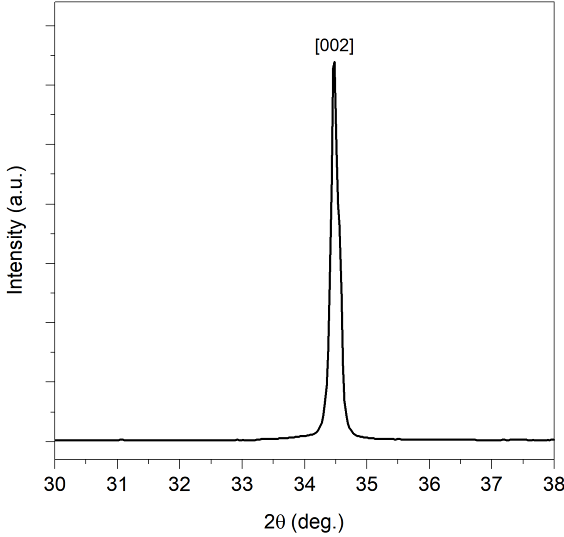

Figure 3.15: XRD pattern of ZnO nanowires grown along the c-axis of the wurtzite phase

3.2 HfO_2-based devices

The fabrication and study of HfO_2-based devices presented in this Thesis was aimed at providing insights on the effect of nano-structural engineering on the resistive switching behaviour of hafnium oxide. Starting from specific technological conditions regarding the device structure, a systematic approach was adopted in order to investigate the effects produced in the device performances by partial modifications of the fabrication process. As a consequence, given the well established boundary conditions and constraints defining the framework in which the investigation process was carried out, the attention was strongly focused on a narrow range of properties and characteristics in the electrical domain, mainly referring to the typical figures of merit of resistive switching devices. As a result, besides the extensive characterizations and tests carried out to allow a systematic and statistical analysis of the electrical performances as a function of the fabrication solutions adopted, material characterization was exclusively focused on morphological investigations. For the crosspoint cells, this translated into FESEM analysis, while atomic force microscopy (AFM) was employed for the single electrode cells. Figure 3.16a shows the FESEM image acquired on a die with the crosspoint ReRAM cells fabricated on it with a periodic arrangement. A single device is then shown in Figure 3.16b to emphasize the crosspoint geometry adopted. For the single-electrode cells, AFM in contact mode was instead performed to acquire detailed images of the VIA

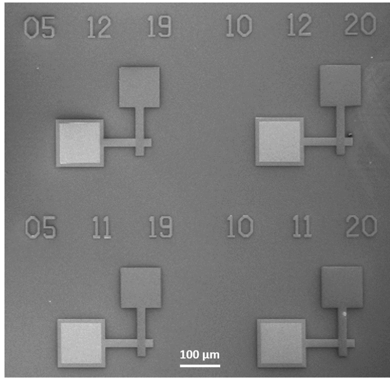

(a) For each nano-structural engineering process performed, 1×1 cm^2 dies with a periodic arrangement of 20×20 crosspoint cells were prepared.

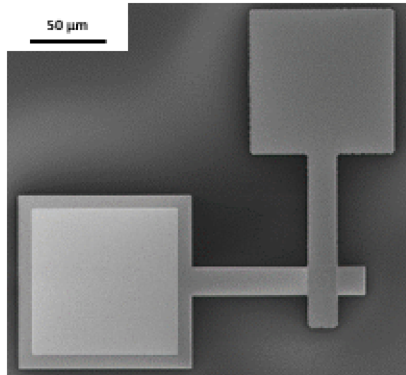

(b) Higher magnifications allow to morphologically inspect single cells and check the outcome of the fabrication process especially for the electrode patterning.

Figure 3.16: FESEM images of crosspoint ReRAM cells with different magnification levels to highlight both the device arrangement on each sample and the crosspoint geometry of a single ReRAM cells

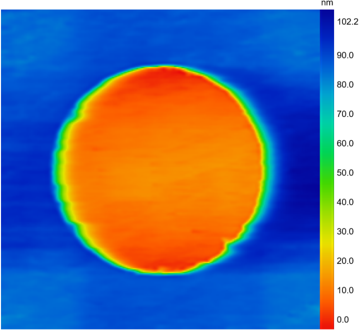

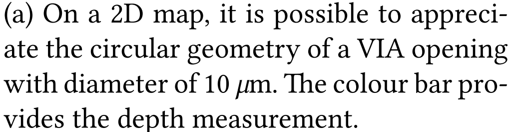

(a) On a 2D map, it is possible to appreciate the circular geometry of a VIA opening with diameter of 10 μm. The colour bar provides the depth measurement.

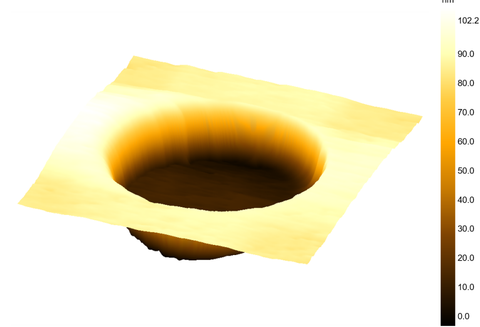

(b) The 3D picture allows, in addition to the measurement provided by the colour bar, to directly visualize the depth of the 10 μm wide VIA opening.

Figure 3.17: AFM images with different colour maps of a VIA opening in single-electrode ReRAM cells

openings used to define the active region of the devices. In Figure 3.17a, a topography map is reported, and a 3D image of the same VIA is shown in Figure 3.17b.

Chapter 4

ZnO nanowires as oxygen vacancies reservoir

Thanks to properties like the wide direct band gap of about 3.3 eV, the large exciton energy of 60 meV, the chemical and thermal stability and the biocompatibility, zinc oxide finds application in many fields ranging from optoelectronics to theranostics. In this range of possibilities, RS devices also find a place. In that domain, great attention has always been focused on thin films, and ZnO was one of the metal oxides that attracted relevant research efforts [150–152]. Additionally, it turned out to be a promising candidate for alternative low-dimensional structures to be employed for resistive switching. Nanowires and nanorods (NRs), for instance, have been proposed and extensively investigated, also thanks to their high surface-to-volume ratio that could open the way to new functionalities [153–169].
In this chapter, the investigation on the impact of ZnO nanowire arrays on the resistive switching performances of ZnO thin films is reported. The electrical characterizations and the device performances are shown, and the resistive switching mechanism is discussed.

4.1 Resistive switching in ZnO thin films

Resistive switching in ZnO thin films was shown to be possible with both VCM and ECM mechanisms. In [143], a comparison between them was carried out, and the impact of film thickness on the RS performances was investigated. Device fabrication was carried out as described in Section 2.1.1, with a symmetric Pt/ZnO/Pt MIM structure for VCM devices and copper TEs instead of platinum ones for the ECM ones. The ZnO film

thicknesses investigated were 50 nm and 100 nm in both VCM and ECM cases, with the additional thickness of 250 nm for ECM only. Such a choice was made due to the outcome obtained from the analysis of the devices in VCM configuration, which did not seem to be as promising as the ECM ones. Performing electrical characterization by means of voltage sweeps, indeed, only few cycles were possible in VCM configuration, with both 50 nm and 100 nm thick ZnO films. In the first case, it was even not possible to stabilize the bipolar RS behaviour, which resulted in noisy and unstable *i-v* characteristics as shown in Figure 4.1a. With the 100 nm thick films, performances only slightly improved, with a too high variability in both SET and RESET processes (see Figure 4.1b) and a clear separation between the HRS and the LRS for few tens of cycles at most (see Figure 4.2).
On the other hand, as mentioned, the ECM configuration allowed much better results, with performances improving as thickness increased. With 250 nm thick films it was possible indeed to obtain up to 400 consecutive cycles, which also showed a strongly reduced variability of the resistance states as it is reported in Figure 4.3. Additionally, retention tests with a fixed length of 800 s were carried out, providing a further confirmation of the significantly improved device stability which can be appreciated in Figure 4.4, where both HRS and LRS resistance levels are shown to be preserved throughout the duration of the test.

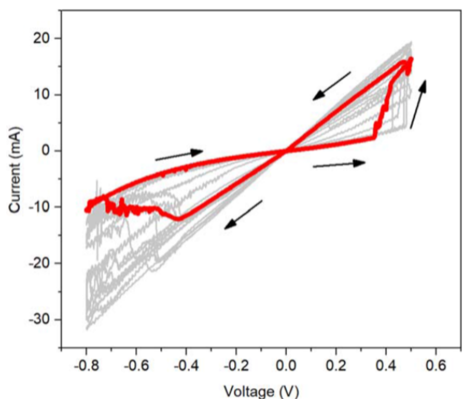

(a) With 50 nm thick ZnO films, it was not possible to stabilize the *i-v* characteristics. The red curve is highlighted as an example over the grey background made of the whole set of acquired characteristics.

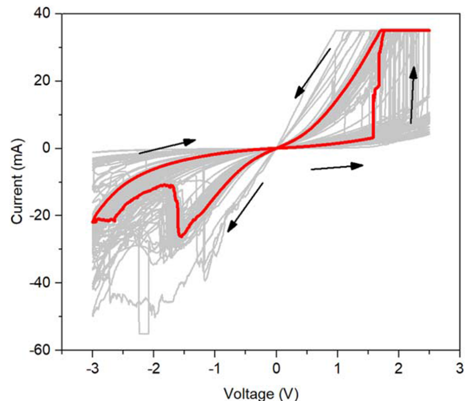

(b) Devices with ZnO thickness of 100 nm showed *i-v* characteristics with poor stability. The red curve is highlighted as reference on the grey background made of the whole set of acquired characteristics.

Figure 4.1: Cycling operation of VCM devices employing ZnO films with thicknesses of 50 nm and 100 nm. Adapted from [143]

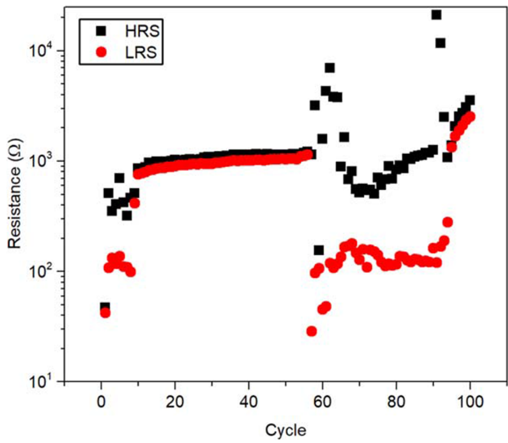

Figure 4.2: Endurance tests carried out for the 100 nm thick ZnO films in VCM configuration showed easily collapsing HRS and LRS levels. Adapted from [143]

In order to correctly interpret these findings, some of the results presented in Section 3.1 must be recalled, especially concerning structural and compositional characterizations. Performing XRD analysis, a preferential crystallographic orientation along the [002] direction, namely the c-axis of the wurtzite phase, was found for the ZnO thin films (Figure 3.14), suggesting the prevailing presence of columnar grains with highly oriented and aligned boundaries [143]. These latter, providing preferential paths for ionic

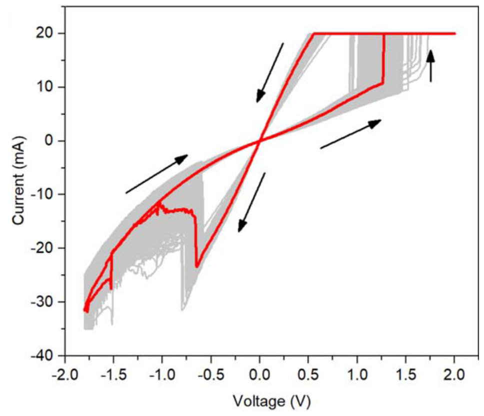

(a) The ECM configuration allowed performance improvements resulting in a reduced variability of cycling operation compared to VCM devices.

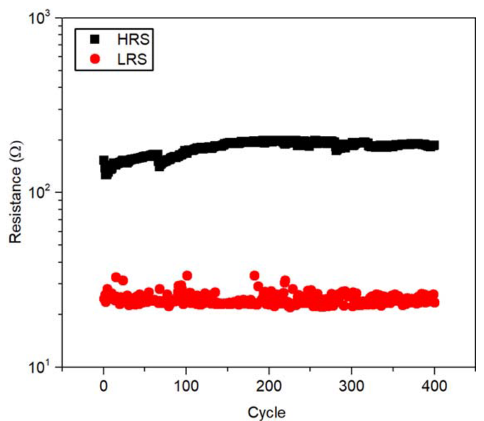

(b) Endurance tests highlighted the good stability of ECM devices showing good stability of both HRS and LRS levels for some hundreds of cycles.

Figure 4.3: Cycle-to-cycle reliability in ECM devices with 250 nm thick ZnO film. Adapted from [143]

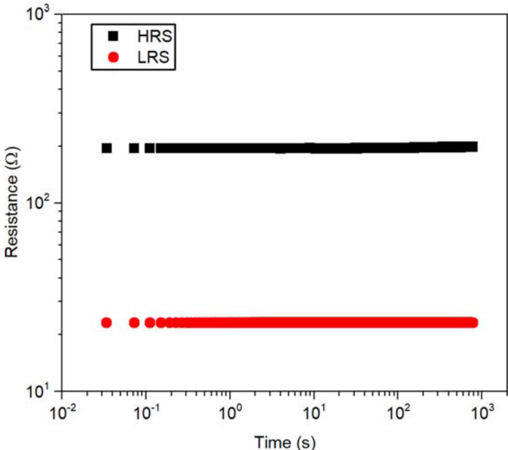

Figure 4.4: Retention up to 800 s obtained for ECM devices with 250 nm thick ZnO film. Adapted from [143]

species motion, endorse the migration of copper cations in the case of ECM devices and of intrinsic defects like oxygen vacancies in VCM ones, with the consequent possibility of conductive filament formation [152, 170–175]. The role played by the ZnO film thickness can hence be elucidated referring to the grain enlargement, and their corresponding reduction in number, occurring when thicker films are deposited. Decreasing the number of grain boundaries available for ionic migration, the CF formation loses indeed in randomicity and gains in stability, resulting in devices with reduced cycle-to-cycle variability and improved reliability [143, 171]. Clearly, this holds only if the ionic species needed for the redox processes involved in the resistive switching mechanism are available. Therefore, the lack of significant improvements for VCM devices can be explained through the good stoichiometry of the zinc oxide films revealed by the XPS analysis (Figure 3.9), which implies a low amount of oxygen-related defects available for the valence change memory mechanism [143, 176, 177].

4.2 Conductive filament observation in ZnO thin films

In order to investigate the nature of the resistive switching behaviour rather than the resulting electrical performances, scanning probe microscopy (SPM) techniques were employed on 250 nm thick ZnO thin films. Specifically, AFM was adopted, with both contact and intermittent modes. Concerning the former, conductive AFM (C-AFM) was performed for electrical investigations, while the latter was employed in the so-called

tapping mode in order to acquire topographical images of the ZnO thin films. The analysis of the surface topography provides indeed a key information for the preparation of subsequent electrical AFM characterizations as well as for a correct interpretation of these latter. Common to all the electrical modes of atomic force microscopy, is the contrast formation mechanism, which relies on the electrical convolution between the AFM tip and the sample surface. More specifically, the electrical contact area defines how and where a signal due to charge flow (in contact mode) or surface potential (in non-contact mode) can be collected as a result of tip-surface interactions. Therefore, the surface roughness of the probed sample must be taken into account during C-AFM characterizations, in order to avoid wrong interpretations due to misleading information obtained during the acquisition of the electrical signal [76, 178–180]. For the 250 nm thick zinc oxide thin films, the surface topography turned out to be characterized by a roughness of (8.9 ± 0.3) nm, evaluated starting from the heigh signal of 2 μm × 2 μm AFM maps like the one shown in Figure 4.5. Such maps provided indeed signals following a normal distribution, as it can be appreciated in Figure 4.6a where both the histogram representation and the gaussian probability density function used to fit the signal are reported. Taking advantage of such observation, the surface roughness evaluation was performed through the standard deviation of the resulting Gauss distribution, as it is reported in [143] too. A third kind of inspection of the surface roughness, in addition to the topography map by itself and the height signal distribution, was then carried out extracting topographical profiles from the AFM maps. As it is shown in Figure 4.6b,

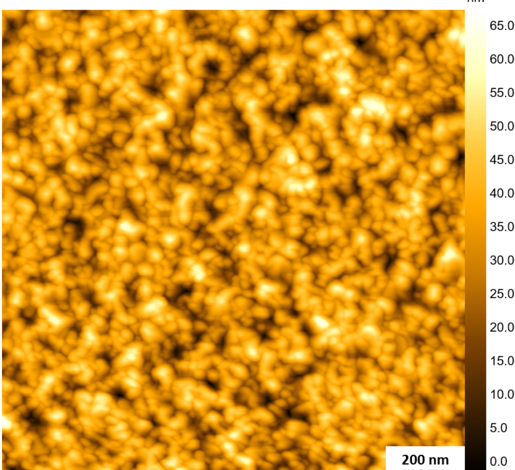

Figure 4.5: Topography map acquired through a tapping mode measurement on ZnO thin film. Adapted from [143]

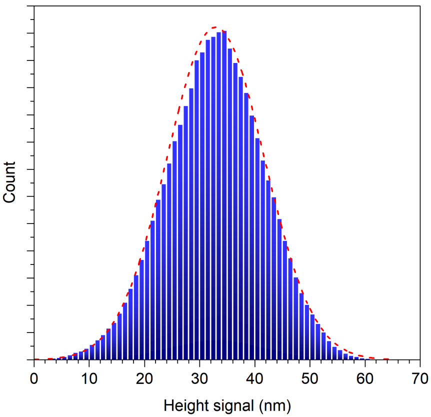

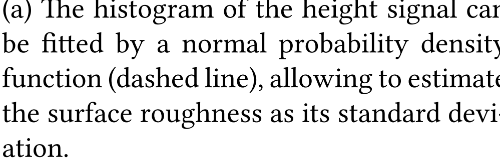
(a) The histogram of the height signal can be fitted by a normal probability density function (dashed line), allowing to estimate the surface roughness as its standard deviation.

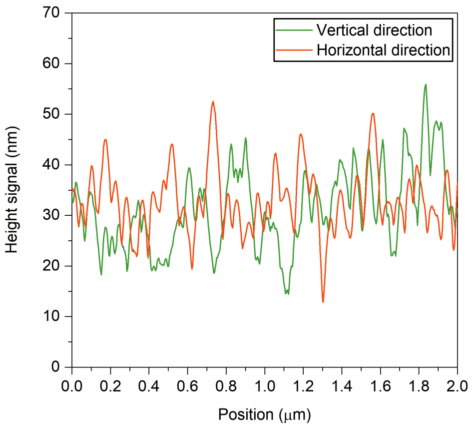

(b) Extracting the topographical profiles from the AFM map, vertical and horizontal directions show similar height signals in terms of both values and peak-to-peak amplitudes.

Figure 4.6: Surface roughness analysis from the height signal of the AFM map acquired in tapping mode

similar peak-to-peak amplitudes of the heigh signal were observed in both vertical and horizontal direction, suggesting once more, although in a limited and slightly more qualitative way, a certain uniformity of the surface topography. Consequently, the possibility for trustworthy C-AFM investigations was confirmed. Particularly, due to the previously described scarce performances of VCM devices, C-AFM was employed to collect additional information about such configuration.

Before starting the measurements, a tip selection process was preliminarily carried out. As it is thoroughly explained in [179], indeed, every C-AFM mode, as well as each C-AFM application, has its own specificities, and the tip to be used must be carefully selected accounting for them. In some cases, choosing the tip might even not be enough, and technical considerations about its cantilever properties may be needed. An AFM probe is indeed composed of a sharp tip, with an apex radius typically in the order of tens of nanometers, placed at the end of a cantilever which in turn is mounted onto a holder structure aimed at probe handling [181]. Length, width and thickness of the cantilever define its stiffness, quantified by the spring constant k_c, which plays the role of proportionality term between the cantilever deflection δ_c and the tip-sample force F_c in the Hooke's law $F_c = -k_c \cdot \delta_c$. From this latter it turns out that the tip-sample interaction is the first criterion to be taken into account not only for the selection of the SPM mode to be used but also for the identification of the best suited combination of tip material

and cantilever properties. Although electrical AFM modes obviously restrict the range of suitable tip materials, conductive AFM experiments can be carried out employing a variety of possible probes. In more detail, focusing on standard contact mode C-AFM, among all the possible conductive tips, the proper one is the one that provides the best combination of spatial and electrical resolution, durability and cost. If, for instance, tip wear-out, and hence durability, is a major concern, metal-coated silicon tips might not provide results as good as those given by doped diamond ones, but these latter have a drastically different cost. A suitable alternative to couple durability and high electrical conductivity with a trade-off in cost is offered by platinum silicides tips. On the other hand, if the electrical resolution must be as high as possible and the tip wear-out is not a critical issue, platinum tips may be an optimal choice [179]. Thanks to their good electrical properties and low cost, typically adopted tips are the PtIr-coated Si ones, which ensure adequate performances in a large number of cases. However, peculiar applications of C-AFM exist that require some of the specific characteristics provided by the other, less common, tips. To give a few examples, in [182] different PtIr-coated silicon tips have been considered, in [183–185] diamond probes have been employed and in [186] they have been compared with platinum silicides tips, which have been adopted, for instance, in [187].
For the C-AFM investigation of the ZnO-based RS devices with zinc oxide film thickness of 250 nm, platinum tips were employed, due to two different reasons. First, following all the aforementioned considerations, to be made when designing a C-AFM experiment, fully metallic tips were the right choice in order to maximize the electrical resolution with a wear-out behaviour good enough according to the material to be probed. Second, since the C-AFM analysis was to be performed directly on the ZnO surface, hence without the patterned top electrode, the platinum AFM tip allowed to replicate the symmetric Pt/ZnO/Pt MIM structure employed for the previously tested devices. Specifically, the chosen tips were characterized by the following technical specifications, given by the manufacturer as nominal values:

- *tip height:* 80 μm
- *tip radius:* < 20 nm
- *cantilever length:* 400 μm
- *cantilever width:* 60 μm
- *spring constant:* 0.3 N/m
- *frequency:* 4.5 kHz

- *manufacturer:* Rocky Mountain Nanotechnology
- *model:* 12Pt400B

Being an SPM technique, conductive AFM natively provides 2D maps containing specific information collected while scanning a surface. Evidently, the peculiarity of C-AFM is the electrical nature of such information, resulting from the conductivity properties of the probed sample. Additionally, pointwise measurements can be performed too, producing *i-v* characteristics through the application of constant or variable voltages. Both current maps and pointwise *i-v* curves are produced using the AFM tip as electrode.
The analysis on the 250 nm thick ZnO film was carried out employing both of these characterization methods, by means of a Bruker Innova AFM, combining them in a three-step procedure as it follows:

step 1: investigation of the pristine state conductivity by means of 2D conduction maps with a maximum applied voltage of 1 V;

step 2: pointwise *i-v* characterization by means of voltage sweeps, up to 10 V, applied in different positions along the surface area previously scanned;

step 3: acquisition of new 2D conduction maps in the same region and with the same applied voltage as for the first step.

With a simplified description, these operations basically compose a read-write-read procedure, where the final read step plays a twofold role: on the one side, it verifies if any

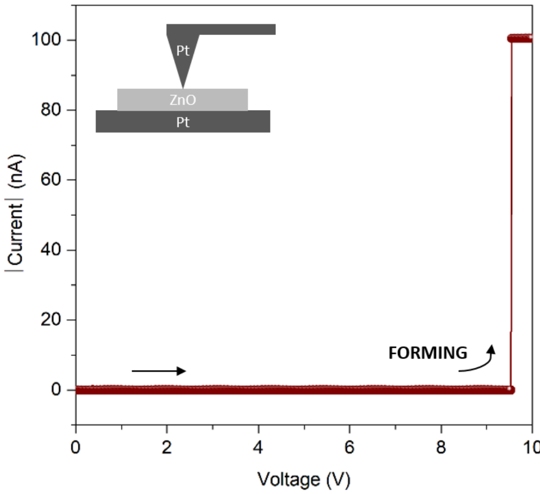

Figure 4.7: Forming process observed by C-AFM on 250 nm thick ZnO film

conductivity change has been induced by the write operation, on the other side, it provides information about the nature of such possible changes, elucidating their localized or distributed character.
Figure 4.7, together with a schematic representation of how the symmetric Pt/ZnO/Pt MIM structure was reproduced during the C-AFM measurements, shows a forming process achieved through the pointwise application of voltage sweeps, described for step 2, with a compliance current of 100 nA. The subsequent conduction map was acquired scanning a 500 nm × 500 nm area with an applied voltage at the tip of -1 V, the bottom Pt electrode grounded, the I_{CC} value kept at 100 nA and a tip-to-sample force about 14 nN. This latter was evaluated by means of a MATLAB function (Appendix B) written on purpose to analyse and combine topography and cantilever deflection information simultaneously collected during the C-AFM scan in contact mode. Reported in Figure 4.8, the C-AFM map shows electrical conduction in a well localized position only. Such spot of high current can be safely ascribed to the presence of a conductive filament created by the previous forming process, but the resulting physical dimensions needs careful evaluations and cannot be considered as precise and reliable measurements. The lateral resolution of electrical AFM modes is indeed related to the so-called effective emission area (A_{eff}), whose correlation with the physical contact area (A_c) is a critical point of electrical AFM in contact mode [179]. While the second one, namely A_c, can be estimated, with some approximation, relying on the Hertz contact theory, A_{eff} is influenced by other factors too, like the electrical tip-sample contact, intended

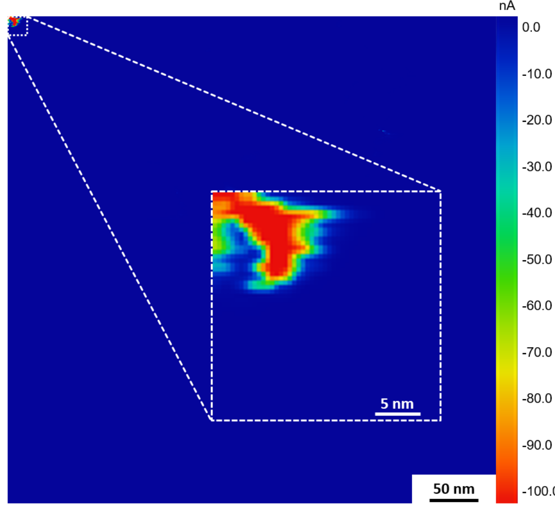

Figure 4.8: 2D conduction map on 250 nm thick ZnO film after pointwise voltage ramps

as the physical properties of the tip-sample junction, and the measurement environment. Specifically, concerning the presented analysis, tests were performed in air and at room temperature, implying the likely presence of a water meniscus at the tip-sample junction able to enlarge the effective contact area. Moreover, being zinc oxide a semiconductor material, the estimation of A_{eff} from A_c could not be obtained through the typical assumptions made for tip-metal or tip-insulator contacts, since none of the two opposite scenarios could be considered. For C-AFM on semiconductors, indeed, the effective emission area neither spreads as on metallic samples nor approaches A_c as for tip-insulator contacts [179]. Due to such limitation, it was not possible to get real information about the conductive filament dimensions, but nonetheless the filamentary nature of VCM-based resistive switching in ZnO thin films was observed.

4.3 Improved resistive switching with ZnO nanowires

In the field of resistive switching, nanowires, as well as nanorods, have been investigated mainly as prospective candidates for possible alternatives to the conventional device structures based on thin films. In many cases, these 1D nanostructures have been proposed for their high surface-to-volume ratio, which endorses the implementation of additional properties and functionalities through the adoption of specific surface treatments [153–155, 157, 169]. In this Thesis, nanowires are shown in a different perspective: not as alternative but as auxiliary to thin film devices. Specifically, the beneficial effect of zinc oxide nanowires hydrothermally grown on ZnO thin films is reported, with the resulting RS performance improvement [130].

4.3.1 Electrical characterization

The RS devices were fabricated as described in Section 2.1.2, with ZnO nanowire arrays grown on top of zinc oxide thin films and platinum electrodes enclosing the resulting ZnO-based double layer. Electrical characterization was carried out in air and at room temperature. Keeping the bottom electrode grounded and applying voltage ramps to the TE by means of a Keithley 4200-SCS (Figure 4.9), *i*-*v* characteristics were produced. With the same setup, and in the same conditions, reliability and stability assessments were also obtained, investigating typical RS parameters as endurance and retention.
Before observing resistive switching, forming of the Pt/ZnO/NWs/Pt devices was needed. To induce it, a voltage ramp up to 11 V was applied at the top electrode, and a current

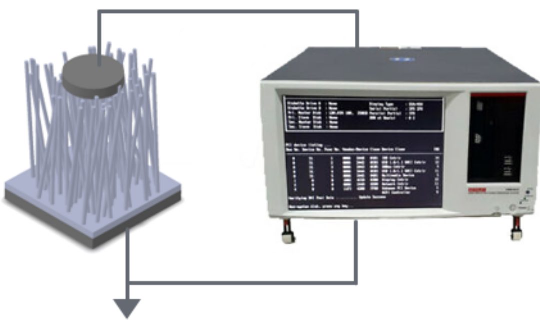

Figure 4.9: Scheme of the *i-v* characterization setup

compliance of 30 mA was set. The resulting *i-v* curve, reported in Figure 4.10, highlighted the presence of a self-limiting behaviour producing an almost flat characteristics in the intermediate voltage range. Such self-imposed current compliance was overcome for voltages higher than 10.4 V, and it can be explained looking at the electrical properties, in the pristine state, of the two ZnO-electrode contacts present within the devices. From the electrical standpoint, since both the BE and the TE make a Schottky junction with the ZnO film the ZnO NWs respectively, the Pt/ZnO/NWs/Pt structure can be indeed described as two Schottky diodes connected back-to-back through a series resistance. As a consequence, when a voltage difference is applied at the device ends, one of these diodes is in direct polarization condition while the other one is reversely polarized [188–190]. Once forming was achieved, cyclic bipolar voltage sweeps 0 V ⟶ 4 V ⟶ -2 V ⟶0 V were employed to evaluate the RS properties and performances of

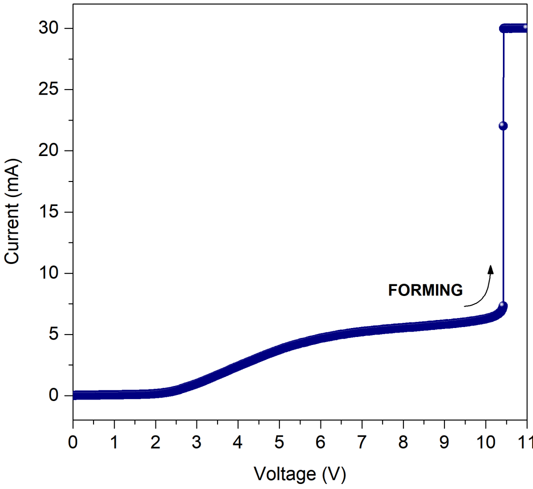

Figure 4.10: Forming process of a Pt/ZnO/NWs/Pt device. Adapted from [130]

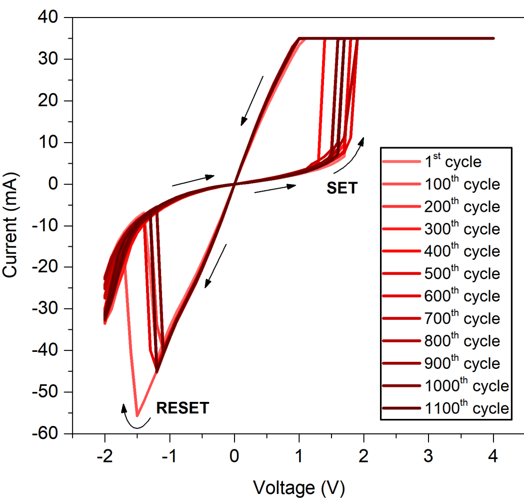

Figure 4.11: Representative subset of the *i*-*v* curves collected for more than 110 consecutive cycles. Adapted from [130]

the devices. Switching voltages and resistance levels, as well as reliability and stability, were investigated. As it is summarized in Figure 4.11, more than 1100 consecutive cycles, with I_{CC} set equal to 35 mA, were obtained with good repeatability. The *i*-*v* characteristics showed indeed a significant overlap, which can be qualitatively considered as a footprint of device stability. The reliability of both SET and RESET transitions was

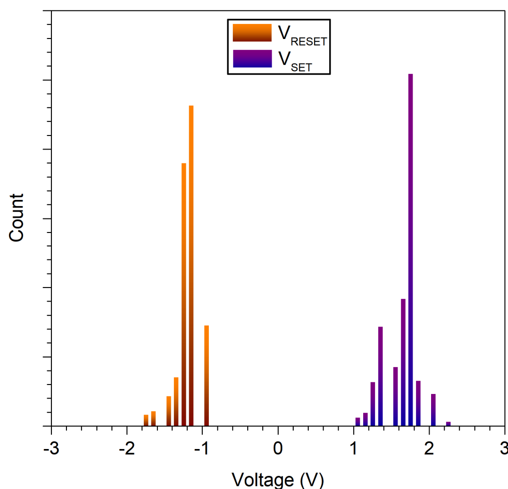

Figure 4.12: The V_{SET} and V_{RESET} narrow distribution resulting from the cyclic *i*-*v* characterization. Adapted from [130]

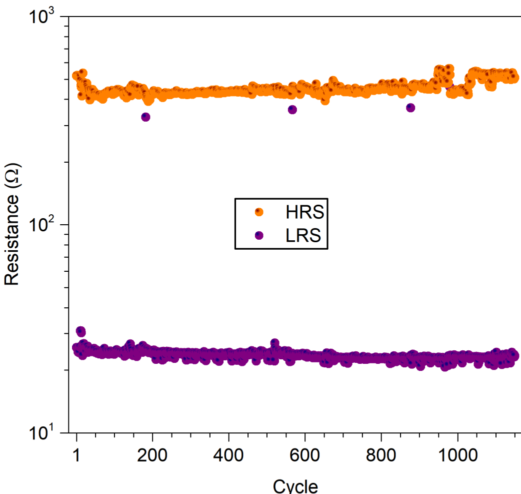

Figure 4.13: Endurance of the NW-based devices showing stable resistance levels for more than 1100 cycles. Adapted from [130]

then reported through the variability of V_{SET} and V_{RESET}. From Figure 4.12, their narrow distributions around 1.7 V and -1.2 V respectively can be appreciated. Comparing these results with Figure 4.1, the huge improvements in cycling capability given by the ZnO nanowires turned out to be quite clear. Better resistive switching performances with respect to the devices based on ZnO thin films were also observed in terms of

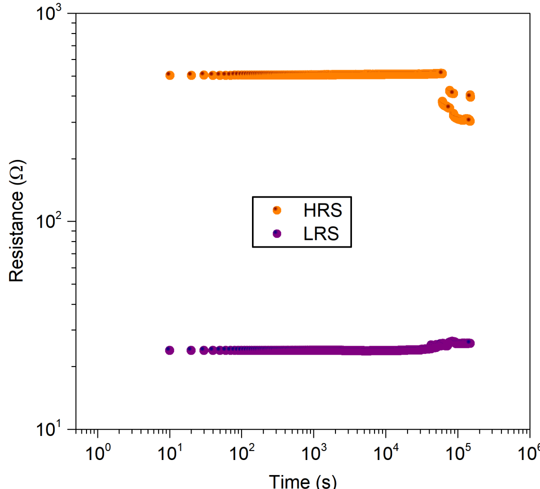

Figure 4.14: Retention tests for the NW-based devices. Both the ON state and the OFF state were retained for more than 10^5 s. Adapted from [130]

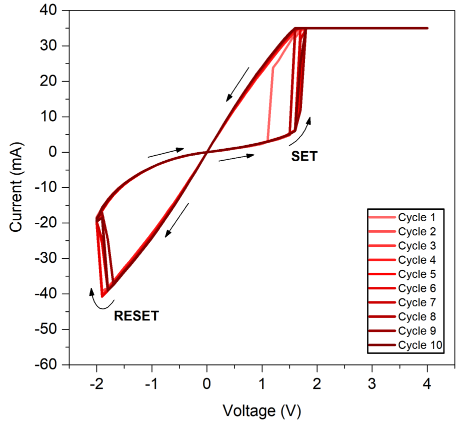

(a) Cyclic bipolar voltage sweeps in the range (-2, 4) V resulted in reliable *i*-*v* characteristics also after the retention tests, with slight changes in V_{RESET} only.

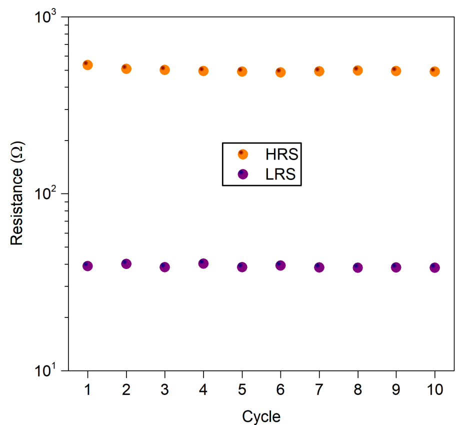

(b) Endurance after the retention tests showed a preserved good stability of the resistance levels, with the ON/OFF ratio almost unaltered.

Figure 4.15: Cyclic *i*-*v* curves and endurance measurement obtained after the retention tests showing an almost unchanged operability of the devices. Adapted from [130]

both endurance and retention, which were evaluated through the application of 0.1 V voltages. The results are shown in Figure 4.13 and Figure 4.14 respectively. Concerning the endurance capability, for more than 1100 cycles an ON/OFF ratio higher than 15 was found, with an error rate about $3{\cdot}10^{-3}$. This latter corresponds to an improvement of two orders of magnitude with respect to the results shown in Figure 4.2 for 100 nm thick ZnO films. Even more relevant improvements were achieved for retention. While for devices with thin film only it was not possible to perform such test because of the RS instability, with nanowires both the HRS and the LRS were successfully retained for more than 10^5 s. Only a slight degradation of the OFF state occurred after $6{\cdot}10^4$ s, and the ON state variability never exceeded 7%. The significance of such results is further enlarged if evaluated with respect to the best performances previously reported for zinc oxide thin films in the ECM configuration. Comparing the retention of NW-based devices with the one in Figure 4.4, namely the best result observed for devices employing ZnO thin films only, an improvement of two orders of magnitude can be indeed appreciated, due to a retention of more than 10^5 s compared to the one of ECM-based devices that only approached the value of 10^3 s. A further proof of the device reliability was also obtained producing additional cycles after the retention tests. As it is shown in Figure 4.15, both the *i*-*v* characteristics and the endurance measurement reported a full operability of the devices, ensured by the almost unchanged ON/OFF ratio and the

minor change, with a slight increase in absolute value, of V_{RESET} only.
Besides comparing the results achieved by the NW-based devices with those reported for thin films, the resistive switching performances obtained with the hydrothermally grown ZnO nanowires were compared to previous results available in literature about ZnO NW-based devices. Table 4.1 summarizes such comparison, showing that the resistive switching performances reported in this Thesis represented, at the time of writing, an unprecedented combination of high-level RS performances, in the framework of ZnO nanowire arrays, in terms of both endurance and retention.

4.3.2 Analysis of the resistive switching mechanism

Given the reasonable certainty that a symmetric MIM structure with Pt electrodes cannot exhibit ECM-based resistive switching because of the high standard redox potential of platinum [57, 69, 191–193], the RS behaviour of the investigated nanowire-based devices can be explained through the VCM mechanism. However, due to the coexistence of two different zinc oxide structures, their interplay, or combined action, must be taken into account. It is therefore necessary to interpret the observed RS behaviour as the result of the coupling between nanowires and the thin film they were grown on (see Section 2.1.1). As it was previously reported, this latter actually provides poor performances in VCM configuration, likely because of the good ZnO stoichiometry and the consequent lack of oxygen-related defects suitable for redox reactions upon anion motion. As it is reported in [194], the formation of a conductive path in ZnO can be ascribed indeed, according to first-principle studies, to extended defects produced by

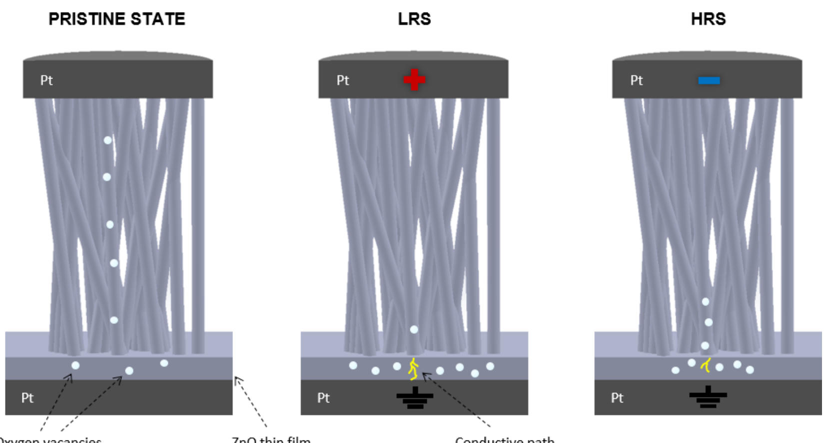

Figure 4.16: Sketch of the RS transitions occurring thanks to the nanowire array acting as an oxygen vacancies reservoir. Adapted from [130]

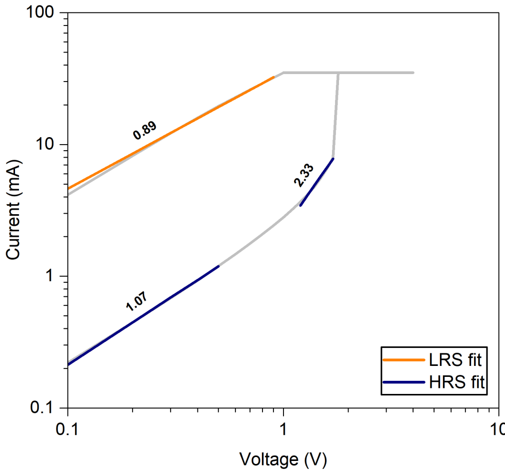

Figure 4.17: *i*-*v* characteristics of NW-based devices in full-logarithmic plot with fit. Adapted from [130]

oxygen ions displacement, and consequent motion of oxygen vacancies, under the effect of an external applied voltage. Therefore, the improvement of resistive switching performances achieved with the nanowire arrays can be explained through the presence of additional ionic species available for the VCM mechanism. In this scenario, ZnO nanowires, thanks to their slight understoichiometry (Figure 3.8), act as an additional oxygen vacancies supplier [130], playing the role of a reservoir as schematically presented in Figure 4.16. The oxygen-related defects, present in the pristine state within the NW array as suggested by the XPS and Raman characterizations discussed in Section 3.1, undergo drift motion when external voltages are applied at the Pt TE. With a positive bias, positively charged defects like oxygen vacancies move towards the BE, and local valence changes give rise to a metallic channel throughout the ZnO thin film. As a result, the forming process is achieved and the device is switched into the LRS. At this stage, once the conductive filament is created by the motion of the oxygen ions and their corresponding vacancies, the role played by the NWs turns into that of an additional series resistance between the ZnO film and the top electrode. Zinc oxide nanowires are indeed unable to exhibit resistive switching unless the ECM configuration is adopted [189]. The opposite transition, namely the RESET, needed to switch the device into the HRS, is achieved applying a negative voltage at the TE. The resulting migration of oxygen vacancies towards the top Pt electrode induces indeed a partial dissolution of the conductive filament in the ZnO thin film, and the device resistance consequently increases. Concerning the electronic conduction mechanism, such RS behaviour produces different regimes, as it is summarized in Figure 4.17 by the fit of an

i-v characteristics in a full-logarithmic plot. The presence of a metal-like conduction path responsible for resistive switching is highlighted by the nearly ohmic behaviour observed in the LRS, while the space-charge-limited current (SCLC) mechanism can be identified in the HRS. In the OFF state, indeed, electronic conduction changes as the applied voltage, and hence the electric field, increases. The initial ohmic behaviour at low voltages is followed by a squared power-law ($i \propto v^2$) region, which leads to the steep current increase, at higher fields, marking the switch into the LRS [130]. Although ohmic conduction is found in both the LRS and a limited region of the HRS, its physical origin differs in the two cases. Concerning the ON state, it results from a local depression of the Pt/ZnO Schottky interface [194]; while in the low voltage regime of the OFF state it can be ascribed to thermally generated free electrons within the ZnO film [195]. For the power-law region of the HRS, the Mott-Gurney law can be employed to describe the current density [196]:

$$j_{\mathrm{SCLC}} = \frac{9}{8}\mu\epsilon_0\epsilon\theta_0\frac{V^2}{L^3} \tag{4.1}$$

where μ is the electronic mobility, ϵ_0 is the vacuum permittivity, ϵ is the ZnO relative dielectric constant, θ_0 is the ratio between the free charges and the shallow trapped ones, L is the ZnO film thickness and V is the applied voltage.
From the electronic performance standpoint, the outlined RS mechanism suffers from the potentially crucial drawback of switching currents in the order of tens of mA, which turn out to be an inherent result of the role played by stoichiometry, translated into presence and concentration of oxygen vacancies, in zinc oxide nanowires. In [160], similar findings are indeed presented, with a reduced O_a/O_b ratio resulting in improved endurance and retention performances at the cost of high switching currents. Additionally, even in an ECM configuration, as it is reported in [162] where different ZnO nanorod-based devices are compared, a larger relative area of the O_b component in the O 1s XPS peak, besides providing improved endurance capabilities, produced a significant increase of the switching currents.

4.4 Discussion

Zinc oxide is a well-known, highly versatile material which finds applications in many different fields ranging from medicine to optoelectronics. Its physical and chemical properties make it suitable for a number of processes and treatments, from ALD deposition to surface functionalization. Resistive switching is one of the technological

domains in which ZnO can be employed, in form of thin films as well as taking advantage of its variety of nanostructures. In this chapter, the possibility of combining some of these aspects has been discussed, reporting the results of a nano-structure engineering approach adopted for ZnO-based RS devices. The performance improvements achieved coupling ZnO thin films with ZnO nanowire arrays have been presented, and the investigation of the physical origin of such results has been reported. Additionally, the validity of the adopted methods for the device fabrication has been shown through a performance comparison with other RS devices, based on zinc oxide NWs, reported in literature. In conclusion, ZnO nanowires have been shown to have the potentiality for complementary mechanisms to be adopted for the purpose of improving the resistive switching performances of ZnO-based devices.

Table 4.1: Comparison of RS performances for devices based on ZnO nanowire arrays [130]

	NW length (μm)	BE - TE materials	Growth process	V_{SET} (V)	V_{RESET} (V)	Endurance (cycles)	Retention (s)	ON/OFF ratio	Switching behaviour
This Thesis	1.6	Pt - Pt	Hydrothermal	1.7	-1.2	>1100	>10^5	>15	Bipolar
[149]	0.8	Pt - Pt	LPCVD	0.9	-1	70	10^4	100	Bipolar
[157]	0.2	FTO glass - Au	Electrochemical deposition	-1.9	2.08	200	10^4	100	Bipolar
[158]	2	Cu - Au (AFM tip as TE)	Vapour-solid	6	4.5	N.A.	Few seconds	$2 \cdot 10^3$	Unipolar
[159]	1.5	Au - Cr	Hydrothermal (with polymer coating)	7	-7	30	N.A.	3.5	Bipolar
[160]	0.65	ITO - Pt	Hydrothermal	5	-4	N.A.	N.A.	$3.3 \cdot 10^2$	Bipolar
			Hydrothermal ^{i}	4.8	-4	N.A.	N.A.	10^4	Bipolar
			Hydrothermal ^{ii}	5.5	-5.2	1000	$5 \cdot 10^4$	$3.3 \cdot 10^5$	Bipolar
[161]	1	ITO - Al	Chemical bath	2	1.5	200	N.A.	10	Bipolar
[162]	0.05	ITO - Cu	Hydrothermal ^{iii}	1.6	-2	<20	$7 \cdot 10^3$	100	Bipolar
			Hydrothermal ^{iv}	1.4	-2	10000	$7 \cdot 10^3$	10^3	Bipolar
[163]	0.8	AZO glass - Au	Aqueous solution	6	-6	30	80 cycles ^{v}	10^4	Bipolar
[164]	0.45-0.54	Ag - Au	Hydrothermal	0.347	-0.754	30	N.A.	100	Bipolar
[165]	1-1.2	Pt - Cu	CVD	1.5	-0.8	N.A.	N.A.	10	Bipolar
			CVD (with polymer coating)	1.5	-1.3			100	
		Pt - Pt	CVD	-1.5	1.5	N.A.	N.A.	10	Bipolar
			CVD (with polymer coating)	-0.5	0.9			10	
[166]	2.9	ITO - Pt	Hydrothermal	0.72	-0.59	120	10^3	6	Bipolar
[167]	N.A.	Au - Au	Hydrothermal	0.84	0.23	100	10^4	10	Unipolar
[168]	0.15	Pt - Pt	Chemical bath	1.3	-0.7	100	10^4	40	Bipolar
				1.5	0.6				Unipolar

^{i} GO/ZnO NRs/GO/ZnO NRs structure
^{ii} GO/ZnO NRs/GO/ZnO NRs/GO/ZnO NRs structure
^{iii} Porous nanorods
^{iv} Compact nanorods
^{v} In cycles with (-1,1) V voltage sweeps

Chapter 5

Ti-based buffer layers to modulate oxygen extraction from HfO_2

In the 1990s, the development of very large scale integration (VLSI) in CMOS technology faced one of its major issues due to the approaching physical limits of gate dielectrics. Traditional gate materials, indeed, were not able to sustain the extreme dimension scaling, because of the excessive leakage currents and the consequent difficulties in charge storage. In order to meet such technological challenge, alternative materials were investigated, looking for a dielectric with high permittivity, large band gap, low interface state density and high thermal stability. A promising solution was found to be represented by HfO_2 [197–200]. As a matter of fact, hafnium dioxide then had a great impact on electronics, also endorsed by the unique potentialities of a fabrication technique like atomic layer deposition. Its application in the resistive switching domain came out almost as a natural consequence, as already mentioned in Chapter 2, and its success can be appreciated looking at the number of papers published on this subject since 2000. Figure 5.1 reports data from Scopus about the overall growth and the annual increase of publications focusing on hafnium dioxide for RS devices. Such Research efforts have been providing more and more detailed insights on the properties and the performances of RS devices based on HfO_2, as well as on the possible technological solutions for their successful CMOS integration [201–205]. However, in view of this key step for ReRAM technologies, further studies involving other typical CMOS materials like tungsten, titanium or titanium nitride are still needed.

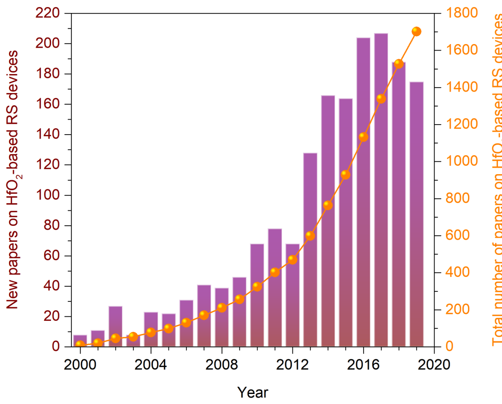

Figure 5.1: Data from Scopus on the number of papers, published since 2000, focusing on HfO_2-based resistive switching devices. Partial data for 2020 have been omitted

In this chapter, an extensive investigation of possible stabilization strategies for ReRAM cells based on hafnium dioxide is reported. Specifically, the case of devices employing tungsten as material of choice for one of the electrodes is shown, highlighting the beneficial effect of titanium as buffer layer. The impact of both thickness and composition of Ti-based films enclosed between the HfO_2 layer and the W electrode is presented through the results of systematic electrical characterizations.

5.1 Device structure and buffer layer selection

In Section 2.2, the fabrication process of the ReRAM cells was entirely described, presenting the complete series of techniques employed according to the process flow reported in Appendix A. Here, the attention is drawn to the device structure, intended as the material stack and its modifications, designed for the investigation of the role played by Ti-based buffer layers. The reference structure, namely the material stack employed for devices without buffer layer, is Pt/HfO_2/W, with platinum as bottom electrode, tungsten as TE and a capping layer made of titanium nitride. This latter, employed as topmost, protective layer is present in all the crosspoint devices, and it will be implicitly accounted for also when not directly mentioned. Table 5.1 summarizes all the material stacks produced through the insertion of a titanium-based buffer layer starting from the reference structure. Each layer is described in terms of both the material it is made of and its thickness, and all the stacks are labelled with a representative name, which refers to the main property of the corresponding samples and hence to the structure of all the devices from each of them. Since the ultimate goal of the whole study was

Table 5.1: Material stacks of the investigated ReRAM cells [135]

Sample name	Inert electrode		Oxide layer		Buffer layer		Oxidizing electrode	
	Material	*Thickness* (nm)	*Material*	*Thickness* (nm)	*Material*	*Thickness* (nm)	*Material*	*Thickness* (nm)
NoBuffer	Pt	125	HfO_2	5	-	-	W	60
MixBuffer	Pt	125	HfO_2	5	W:Ti 10%	3	W	60
Buffer1	Pt	125	HfO_2	5	Ti	1	W	60
Buffer3	Pt	125	HfO_2	5	Ti	3	W	60
Buffer5	Pt	125	HfO_2	5	Ti	5	W	60

a performance evaluation through a comparative approach based on the assessment of the impact produced at the device level by modifications in the fabrication process, a sufficiently large number of devices was needed for electrical characterization. To this aim, a set of one hundred and twenty-five ReRAM cells was considered, with twenty-five devices for each material stack. The need for an extensive, systematic investigation of the effect of a titanium-based buffer layer in devices employing both hafnium dioxide and tungsten originated from the instability observed in ReRAM cells based on the NoBuffer structure. In [206], it was indeed pointed out that the poor memory performances observed in devices with HfO_2/W interfaces can be ascribed to the multiple and metastable oxides tungsten can form. Moreover, it was reported that the insertion of a Ti film, aimed at avoiding the HfO_2/W interface, ensures, thanks to the lower energy required by titanium with respect to tungsten for reaction (1.18) [207, 208], a more efficient oxygen extraction from HfO_2, which results in hindering the formation of tungsten oxides. In this Thesis, the investigation of such effect is reported for pure-Ti buffer layers with thicknesses of 1 nm, 3 nm and 5 nm, together with further insights obtained verifying also the impact of a mixed W-Ti film with thickness of 3 nm. This latter, especially, was aimed at gaining additional information about whether the key parameter for device stability improvement was the buffer layer thickness or its composition. The W:Ti 10% films provided indeed a tungsten layer with a titanium concentration of 10% in weight, implying a significant probability for tungsten oxidation even if the HfO_2/W was nominally avoided. In order to take into account possible interfacial effects too, these tests were carried out for different device dimensions. In more detail, referring to Figure 2.3, different sizes of the active region were considered, preparing devices with VIA openings having diameter of 1.5 μm, 2 μm, 5 μm and 10 μm.

5.2 Electrical characterization setups

The comprehensive set of electrical characterizations needed to properly investigate and analyse the device performances, and their dependence on the buffer layer properties, was produced employing three different methodologies and setups, as it is schematically summarized in Figure 5.2. First, DC tests were carried out, through the application of voltage sweeps by means of a parameter analyser Agilent B1500, to investigate the forming process and the possible impact of the buffer layers on $V_{FORMING}$. During such measurements, voltages were applied at the tungsten electrode, the platinum BE was always kept at ground and a compliance current I_{CC} was set through the internal modules of the parameter analyser. The same bias scheme was then used to carry out a C-AFM investigation. In this case, single-electrode ReRAM cells, fabricated as described in Section 2.2.2, were tested by means of an Asylum Research Cypher VRS, employing the full-platinum tips from Rocky Mountain Nanotechnology previously described in Section 4.2. Keeping the AFM tip grounded and applying voltage sweeps at the tungsten electrode with a compliance current imposed to prevent irreversible damages, the same bias scheme adopted for the crosspoint cells was replicated. In addition to these DC approaches, pulse measurements were then performed too, in order to test the operational behaviour of the crosspoint cells in a dynamic regime. For such analysis, due to a typical delay parameter analysers have with respect to the characteristic switching times [209, 210], the current compliance was set and managed through an external n-channel transistor (n-MOSFET) instead of the internal modules of the Agilent B1500. The I_{CC} value was adjusted tuning the gate voltage, with the source of the transistor at ground and the drain connected in series to the device under test. All the

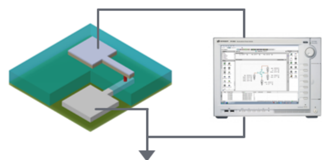

(a) DC characterization of the forming process in crosspoint cells. Voltage ramps are applied at the tungsten electrode, while the Pt BE is kept at ground.

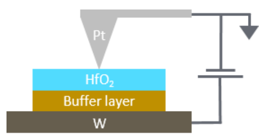

(b) DC characterization of the forming process by C-AFM. The AFM tip is kept at ground and voltage ramps are applied at the tungsten electrode.

(c) Tests in the dynamic regime were performed by pulse measurements taking advantage of an n-MOSFET to control the current compliance.

Figure 5.2: Schemes of the setups employed for the electrical characterizations of the ReRAM cells

electrical measurements, with all the presented setups, were performed in air at room temperature.

5.3 Buffer layer influence on the forming voltage

As mentioned, the investigation of the forming process was the first step in the analysis of the effect of titanium-based buffer layers. For both the DC characterization of crosspoint devices and the C-AFM investigation of single-electrode cells, the same procedure was adopted. Positive voltage ramps from 0 V to 7 V were applied at the tungsten electrode, keeping at ground the platinum one and imposing a current compliance.

5.3.1 DC characterization of crosspoint cells

For the crosspoint cells, the I_{CC} value was set at 1 mA, as it can be appreciated from Figure 5.3. There, the *i*-*v* characteristics acquired during the forming processes are summarized by representative curves for all the material stacks. As it is clear, the presence, and the properties, of a titanium-based buffer layer turned out to affect the forming voltage. Specifically, a decrease of $V_{FORMING}$ was observed moving from the reference (NoBuffer) structure to the Buffer5 samples. A further analysis of such behaviour, carried out adopting a statistical approach, also revealed the possibility for a more quantitative evaluation of the $V_{FORMING}$ reduction. In more detail, Figure 5.4 shows a box

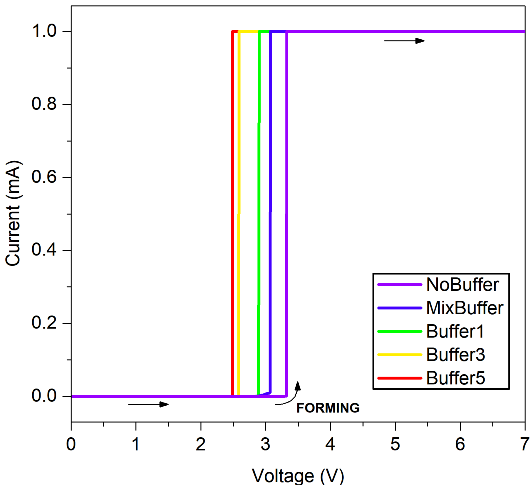

Figure 5.3: Comparison of the *i*-*v* characteristics during forming process for the different material stacks investigated. Adapted from [135]

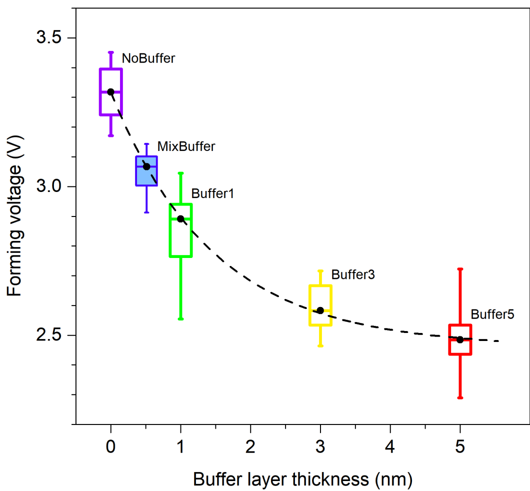

Figure 5.4: Exponential decrease of the forming voltage as a function of the Ti-based buffer layer thickness. Adapted from [135]

plot of the forming voltages observed for all the tested devices from the different samples. As it is highlighted by the dashed line, an exponential decay turned out to well fit the median values of $V_{FORMING}$ for each material stack employing a pure-Ti film. Additionally, operating the other way around, the same exponential fit was employed to define an effective thickness (t_{eff}) of the W-Ti mixed film, suitable for a comparison with the Buffer3 samples. Put another way, the definition of an effective thickness for the W:Ti 10% film was aimed at evaluating whether the key parameter in the $V_{FORMING}$ reduction was the physical thickness of the buffer layer or its actual content of titanium. Clearly, because of its inherent meaning, t_{eff} was defined to coincide with the real thickness for pure-Ti films. The value of about 0.5 nm found as the effective buffer layer thickness for MixBuffer samples, much smaller than the physical dimension of 3 nm, provided an early indication about the substantial importance of titanium compared to the buffer layer thickness. Ti-based buffer layers do not operate as a simple physical barrier between hafnium dioxide and tungsten, their contribution depends on the amount of titanium interposed between the oxide film and the oxidizing electrode [135].

5.3.2 C-AFM analysis

The importance of film composition, rather than its thickness, in defining the impact of Ti-based buffer layers on the forming voltage was further investigated performing C-AFM measurements. As anticipated in Section 5.2, this kind of analysis was carried

out on single-electrode ReRAM cells, replicating the MIM structure of the crosspoint devices by means of a full-platinum AFM tip (Figure 5.2b). As for the study of ZnO thin films discussed in Section 4.2, a three-step procedure was adopted in this case too, with the only relevant difference represented by the maximum applied voltage. In order to replicate the characterization performed for the crosspoint cells, voltage ramps from 0 V to 7 V were indeed employed. Keeping at ground the platinum tip, the same bias scheme adopted for the crosspoint cells (Figure 5.2a) was obtained. Due to the specificity of the characterization technique, namely in order to take into account the extremely reduced section of the AFM tip, and hence to preserve it from melting due to an excessive current density, the I_{CC} value was set at 1 μA. The *i-v* characteristics of the forming process were acquired for devices from NoBuffer, MixBuffer and Buffer3 samples. The selection of such triplet directly originated from the key points highlighted for the crosspoint cells. With these material stacks, it was indeed possible to gain additional information about whether a Ti-based buffer layer has an impact on the device forming voltage and how its content of titanium can influence such effect. The *i-v* curves produced by C-AFM substantially confirmed the previous findings. The highest value of V_{FORMING} was observed for NoBuffer samples, that is to say the devices without buffer layer. A representative characteristic is reported in Figure 5.5, whose inset schematizes the corresponding material stack. The forming voltage was then found to be slightly reduced, by the insertion of the W-Ti mixed buffer layer, as it shown in Figure 5.6. Finally, Buffer3 samples, namely the devices with a 3 nm thick pure-Ti buffer layer, turned out to provide the lowest forming voltage, as it can be appreciated in Figure 5.7. Such results

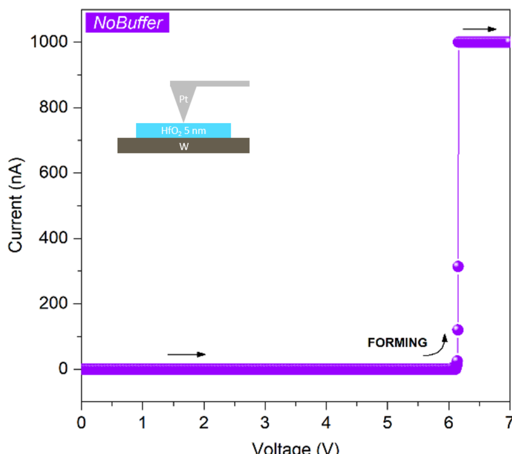

Figure 5.5: Representative *i-v* characteristics acquired by C-AFM for the forming process of devices without buffer layer. Adapted from [135]

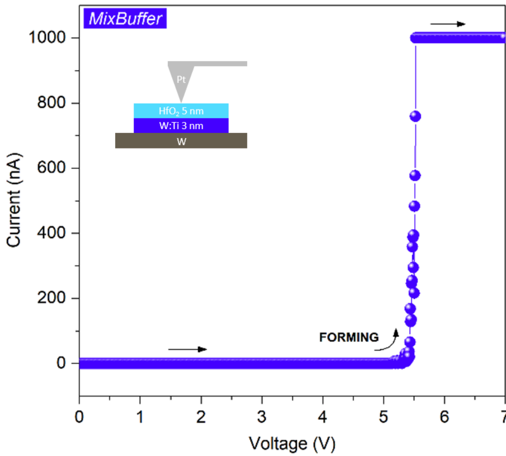

Figure 5.6: Representative *i-v* characteristics acquired by C-AFM for the forming process of devices with the MixBuffer material stack. Adapted from [135]

essentially replicated what DC characterization of crosspoint cells previously revealed: the impact of a Ti-based buffer layer on $V_{FORMING}$ depends on both its thickness and its composition. The MixBuffer and the Buffer3 samples employed indeed a buffer layer with the same thickness of 3 nm, but the effect on the forming voltage was significantly different. Following these observation, the importance of titanium concentration between the oxide and the oxidizing electrode was thus emphasized, since it quite clearly turned out to be the ultimate responsible for the observed variations in $V_{FORMING}$ [135].

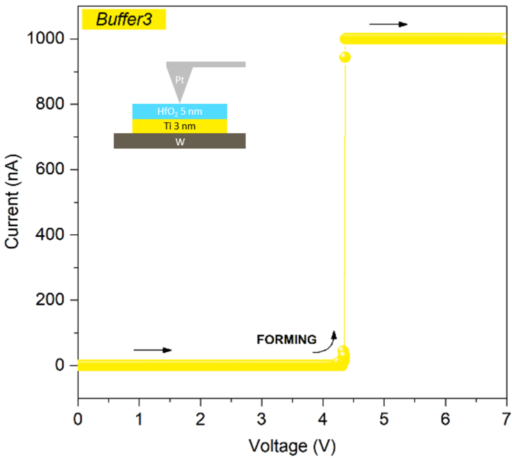

Figure 5.7: Representative *i-v* characteristics acquired by C-AFM for the forming process of devices with the Buffer3 material stack. Adapted from [135]

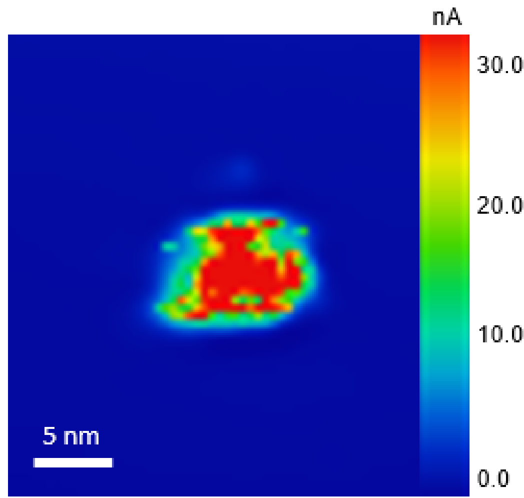

Figure 5.8: Current map acquired after forming on a single-electrode ReRAM cell without buffer layer. Adapted from [135]

After the pointwise *i*-*v* characterization of the forming processes, 2D current maps were also produced. Applying a fixed voltage at the tungsten electrode, with the platinum tip kept at ground, electrical conduction was probed scanning the sample surfaces. For all the three material stacks, current maps reported the presence of well localized, nanometre-sized conductive spots, as it can be appreciated in Figure 5.8 for NoBuffer

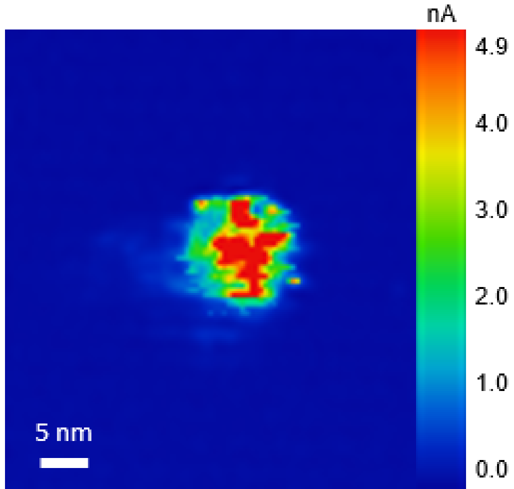

Figure 5.9: Current map acquired after forming on single-electrode ReRAM cell with MixBuffer material stack. Adapted from [135]

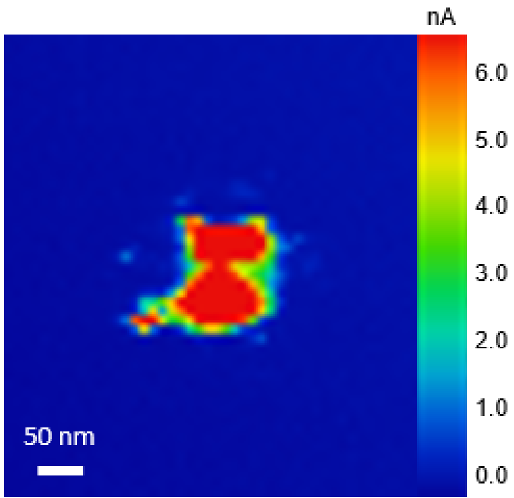

Figure 5.10: Current map acquired after forming on single-electrode ReRAM cell with a 3 nm thock titanium buffer layer. Adapted from [135]

samples, in Figure 5.9 for devices with the MixBuffer material stack and in Figure 5.10 for cells employing a 3 nm thick pure-titanium buffer layer. The presence of such spots strongly suggested a filament-based resistive switching for all the devices [135].
In the same regions where the current maps were acquired, a further analysis was performed in order to verify if any topographical changes occurred on the sample surfaces

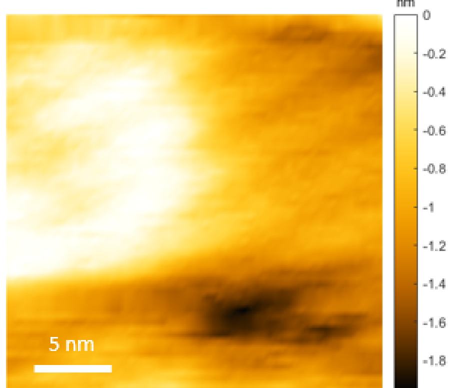

(a) After the forming process, the AFM analysis, performed in contact mode, provided topography images without significant changes in morphology.

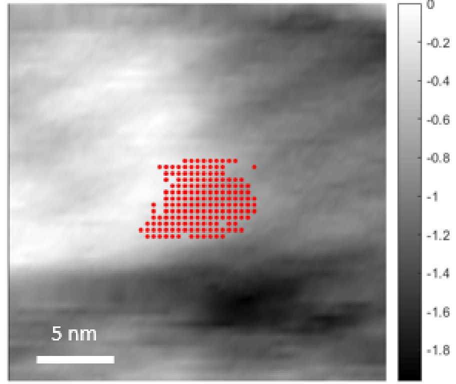

(b) Superimposing current and morphology data, the conductive spot did not show any correspondence with relevant topographical features.

Figure 5.11: Comparison between topography and electrical conduction localization for the NoBuffer material stack. Adapted from [135]

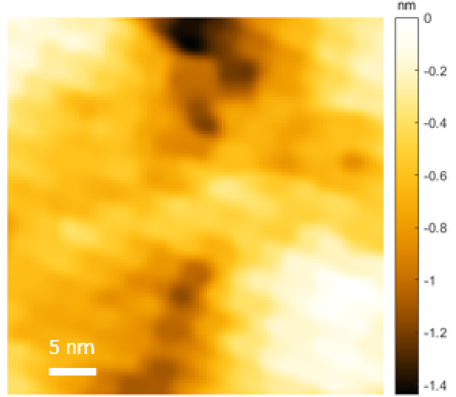

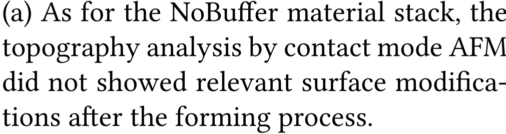

(a) As for the NoBuffer material stack, the topography analysis by contact mode AFM did not showed relevant surface modifications after the forming process.

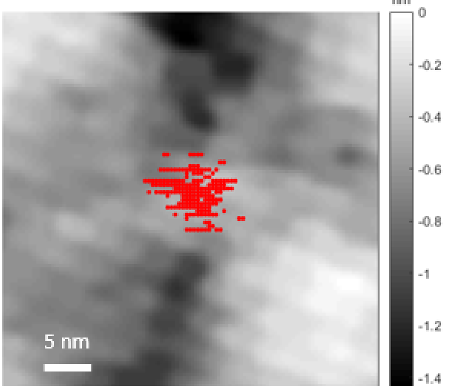

(b) Similarly to the case of NoBuffer samples, the conductive spot did not exhibit any relation with specific topographical features.

Figure 5.12: Comparison between topography and electrical conduction localization for the MixBuffer material stack. Adapted from [135]

after forming, and how such modification could be related to the observed electrical conduction. This additional investigation was possible thanks to the topography signal simultaneously acquired by the AFM tool while scanning the device surfaces for the current map acquisition. By means of a MATLAB code written on purpose, and

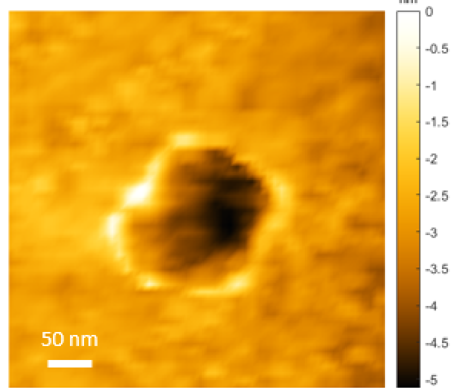

(a) For the Buffer3 material stack, clear surface modifications were found with the topographical analysis after forming process.

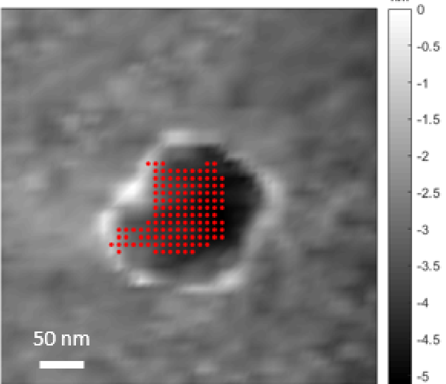

(b) The conductive spot observed with C-AFM turned out to perfectly match with the position of the morphological changes.

Figure 5.13: Comparison between topography and electrical conduction localization for the Buffer3 material stack. Adapted from [135]

reported in Appendix C, a point-by-point superposition of the current maps onto the topography images was performed, thus obtaining a precise localization of the highly conductive spots on the topographical maps. The resulting images are reported, together with the corresponding purely topographical maps, in Figure 5.11 for the NoBuffer material stack, in Figure 5.12 for the case of mixed W-Ti buffer layer and in Figure 5.13 for the Buffer3 sample. As it can be appreciated, changes in the surface morphology were only observed in the case of this latter, and the reported surface modification was found to perfectly match with the position of the conductive spot revealed by C-AFM.

5.4 Impact of the buffer layer on device performances

After the comprehensive electrical characterization of the forming process, device performances were tested. To this aim, the setups sketched in Figure 5.2a and in Figure 5.2c where employed to investigate the cycling capability and the dynamic behaviour respectively. With the former, *i-v* characteristics were produced applying at all the devices bipolar voltage sweeps in the range (-1.5, 3) V, while the latter was subsequently adopted to apply voltage pulses having optimized amplitude and width for each material stack. In both cases, a current compliance of 1 mA was adopted in the positive polarity, in order to avoid critical damages possibly arising from the sudden current increase when switching into the LRS.
By means of the DC characterization, it was also possible to verify the filamentary nature, suggested by C-AFM, of the resistive switching. Consecutive voltage sweeps 0 V ⟶ -1.5 V ⟶ 3 V ⟶0 V were applied at devices from the NoBuffer, MixBuffer and Buffer5 samples. The resistance levels and the switching voltages were evaluated for twenty-five devices from each material stack, accounting for all the different VIA diameters within the crosspoint cells which are 1.5 μm, 2 μm, 3 μm, 5 μm and 10 μm. As it is reported in Figure 5.14, all the tested devices exhibited independence of the RS parameters (R_{HRS}, R_{LRS}, V_{SET} and V_{RESET}) from the VIA size, thus leaving out the possibility of interfacial mechanisms responsible for the resistive switching behaviour. Consequently, the absence of any trend for these parameters as a function of the dimension of the active region represented an additional evidence for the presence of a localized conductive filament, in good agreement with the previous observations by C-AFM [135]. As it is explained in [206], the physical origin of such CF can be ascribed to the efficient oxygen extraction from hafnium dioxide performed by titanium, which also results in an increase of the oxygen vacancies concentration close to the interface between the

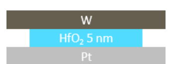

(a) Sketch of the NoBuffer material stack.

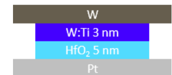

(b) Sketch of the MixBuffer material stack.

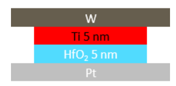

(c) Sketch of the Buffer5 material stack.

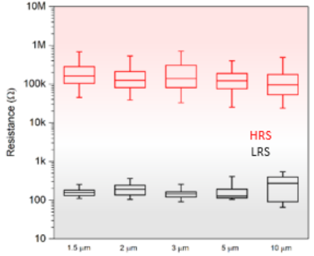

(d) Resistance levels for the different the VIA diameters in devices with the NoBuffer material stack.

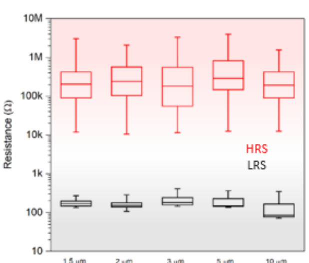

(e) Resistance levels for the different the VIA diameters in devices with the MixBuffer material stack.

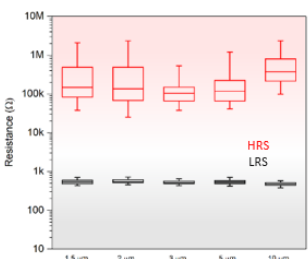

(f) Resistance levels for the different the VIA diameters in devices with the Buffer5 material stack.

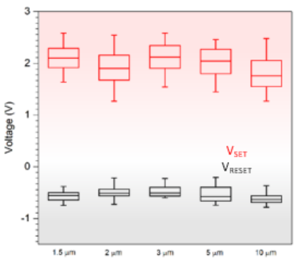

(g) Switching voltages for the different the VIA diameters in devices with the NoBuffer material stack.

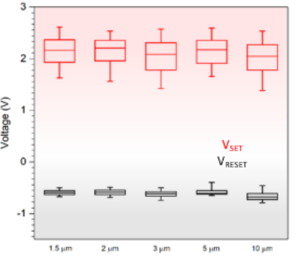

(h) Switching voltages for the different the VIA diameters in devices with the MixBuffer material stack.

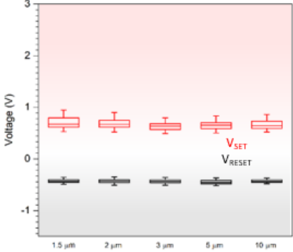

(i) Switching voltages for the different the VIA diameters in devices with the Buffer5 material stack.

Figure 5.14: Box plots from the statistical analysis of resistance levels and switching voltages for devices with NoBuffer, MixBuffer and Buffer5 material stack. Adapted from [135]

HfO_2 film and the buffer layer. When positive voltages are applied at the tungsten electrode, this $V_{ö}$ accumulation couples with an additional drift of oxygen anions towards the buffer layer, and the corresponding vacancies creation eventually leads, according to the VCM mechanism, to the conductive filament formation. A sketch of this process within a crosspoint cell is reported in Figure 5.15.

The same DC analysis, namely the investigation of the resistive switching behaviour

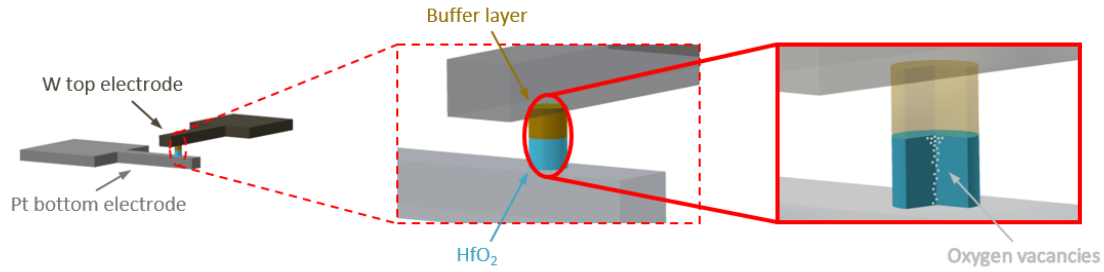

Figure 5.15: Sketch of the VCM-based filamentary resistive switching in crosspoint cells, with the conductive filament modelled as the result of oxygen vacancies motion within the HfO_2 layer

by means of voltage sweeps in the range (-1.5, 3) V, was then carried out on the complete set of one hundred and twenty-five devices accounting for all the material stacks. In this case, consequently to the highlighted independence of the main RS parameters from the dimension of the active region, the statistical analysis did not explicitly take into account the VIA diameter, considering each sample as a uniform set of devices. However, for the sake of completeness, it is worth pointing out that the same number

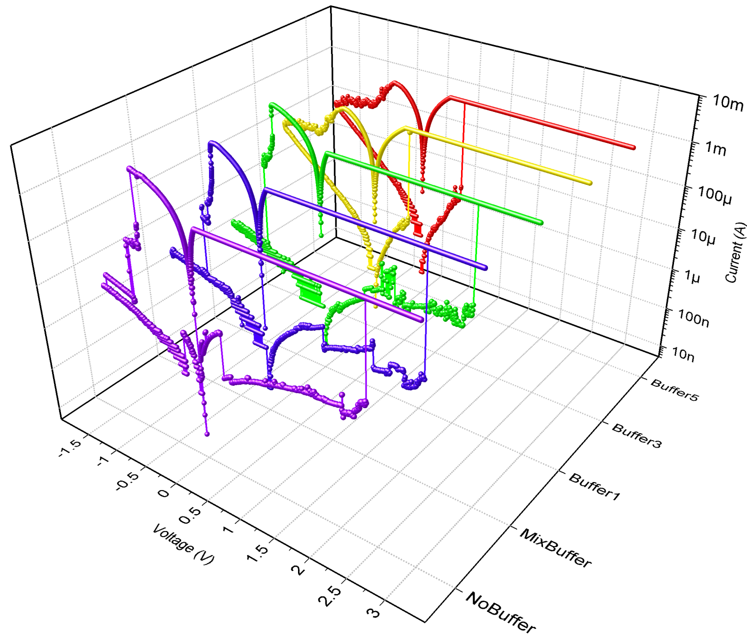

Figure 5.16: Comparison of cyclic *i*-*v* characteristics acquired for each material stack. Adapted from [211]

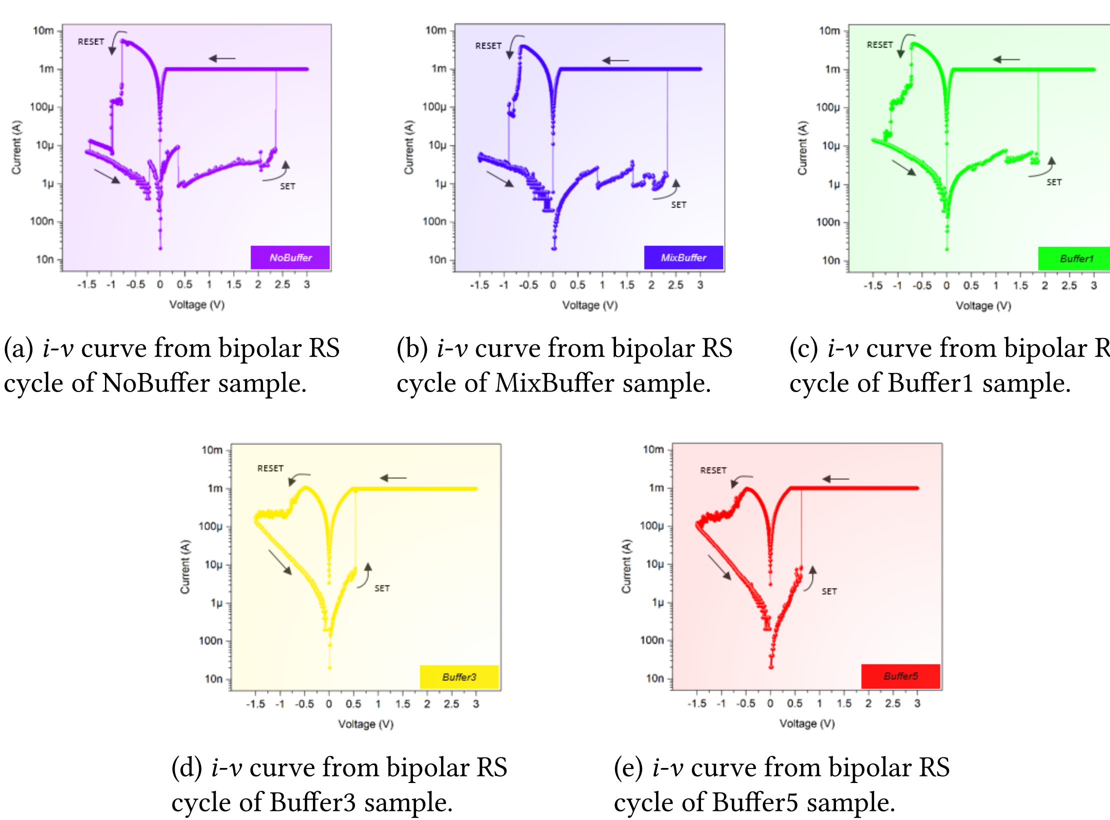

(a) *i*-*v* curve from bipolar RS cycle of NoBuffer sample.

(b) *i*-*v* curve from bipolar RS cycle of MixBuffer sample.

(c) *i*-*v* curve from bipolar RS cycle of Buffer1 sample.

(d) *i*-*v* curve from bipolar RS cycle of Buffer3 sample.

(e) *i*-*v* curve from bipolar RS cycle of Buffer5 sample.

Figure 5.17: Representative *i*-*v* characteristics of resistive switching cycles for each material stack. Adapted from [135]

of devices was tested for each VIA size. A comparison of *i*-*v* characteristics provided by representative bipolar RS cycles of each material stack is reported in Figure 5.16. Looking at them separately and in more detail (Figure 5.17), a clear distinction in the resistive switching behaviour on the basis of the buffer layer effective thickness can be appreciated. Focusing on the NoBuffer sample first, namely the reference structure for devices without buffer layer, cycling instabilities were observed, with current fluctuations occurring in the HRS positive polarity before the sharp SET transition (Figure 5.17a). For t_{eff} lower than 3 nm, a similar behaviour was found, with both MixBuffer (Figure 5.17b) and Buffer1 (Figure 5.17c) samples exhibiting a sharp HRS-to-LRS transition at quite high voltages and after a see-saw current flow. Remarkable differences were instead highlighted by the *i*-*v* characteristics of devices with buffer layers having an effective thickness of 3 nm at least. As it can be appreciated in Figure 5.17d and Figure 5.17e, for Buffer3 and Buffer5 samples respectively, larger values of t_{eff} resulted in a reduction of V_{SET} coupled with a current stabilization. Additionally, looking at the negative polarity,

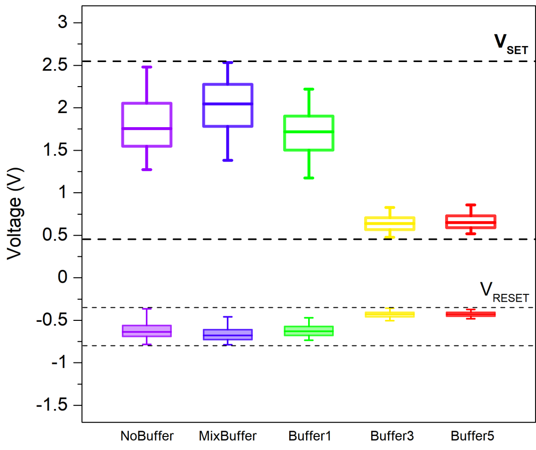

Figure 5.18: Summary of the switching voltages from statistical analysis of the DC characterization. Adapted from [135]

and at the device RESET, it can be highlighted how the insertion of a Ti-based buffer layer with $t_{\mathrm{eff}} \geq 3$ nm introduced a smooth switching, in place of the abrupt LRS-to-HRS transition, and a reduction, in absolute value, of the RESET voltage. Besides these mainly qualitative observations, a quantitative, statistical analysis of the DC characterization was also carried out. Results are shown, by means of box plots, in Figure 5.18 for the switching voltages and in Figure 5.19 for the resistance levels. Median values and standard deviations of these RS parameters are then summarized in Table 5.2.

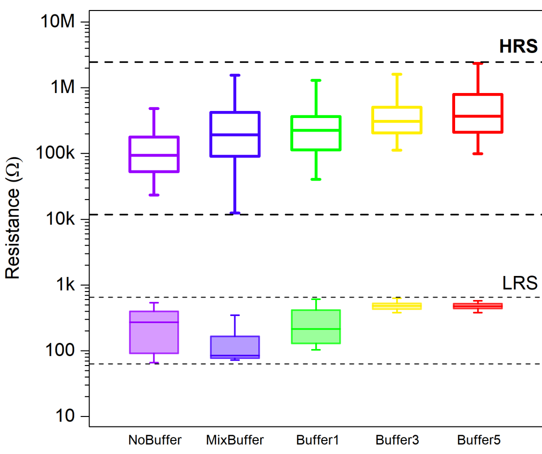

Figure 5.19: Summary of the resistance levels from statistical analysis of the DC characterization. Adapted from [135]

Table 5.2: Statistical analysis of the DC characterization [135]

Sample name	$V_{FORMING}$ (V)		V_{SET} (V)		V_{RESET} (V)		R_{HRS} (kΩ)		R_{LRS} (Ω)	
	Median	*σ*	*Median*	*σ*	*Median*	*σ*	*Median*	*σ*	*Median*	*σ*
NoBuffer	3.31	0.09	1.76	0.38	-0.64	0.12	94.48	154.61	272.55	171.05
MixBuffer	3.07	0.08	2.05	0.34	-0.68	0.10	192.86	3711.84	84.86	104.53
Buffer1	2.89	0.15	1.72	0.32	-0.63	0.09	226.78	427.42	214.86	169.08
Buffer3	2.58	0.09	0.64	0.10	-0.43	0.04	309.41	499.79	483.00	77.28
Buffer5	2.49	0.12	0.65	0.10	-0.43	0.03	368.39	1011.09	474.82	69.09

Figure 5.18 graphically clarifies the above mentioned distinction, based on t_{eff}, in the switching behaviour of the different samples. It clearly shows that the devices enclosing a pure-Ti buffer layer with thickness of 3 nm at least exhibited smaller switching voltages, with a significant reduction of V_{SET} values with respect to NoBuffer, MixBuffer and Buffer1 samples. Furthermore, it also highlights the strongly reduced device-to-device variability, especially concerning the SET voltage, when $t_{\text{eff}} \geq 3$ nm. Similarly, a huge impact of Buffer3 and Buffer5 material stacks on the reduction of the LRS device-to-device variability can be appreciated in Figure 5.19. All of these observations can be interpreted referring to reaction (1.18), which involves oxygen extraction from HfO_2 and consequent oxidations. Due to the presence of an inert Pt electrode in all the devices, such processes, which, in principle, can take place at the interface between the hafnium dioxide film and the layers it is in direct contact with, are actually limited to the HfO_2/W or HfO_2/Ti-buffer interfaces. Consequently, the reported resistive switching behaviours can be explained through the different oxidizing activity of titanium and tungsten. Accounting for both the more efficient oxygen extraction ensured by Ti and the metastable states leading up to the formation of WO_3, current fluctuations and abrupt RESET, which appeared in NoBuffer, MixBuffer and Buffer1 samples and were prevented in case of buffer layers with $t_{\text{eff}} \geq 3$ nm, can be related to tungsten oxidation, which suffers from a higher energy demand and from the existence of multiple possible oxides that can be formed before the stable WO_3 is produced [135, 206, 207, 212].
Further evidence of resistive switching stabilization thanks to titanium-based buffer layers resulted from tests in the dynamic regime. While DC characterization focused on the RS behaviour of the devices, pulse tests were performed in order to assess their operational reliability. Because of this, an optimization procedure also was carried out before starting the measurements: for each material stack, the best pulse parameters

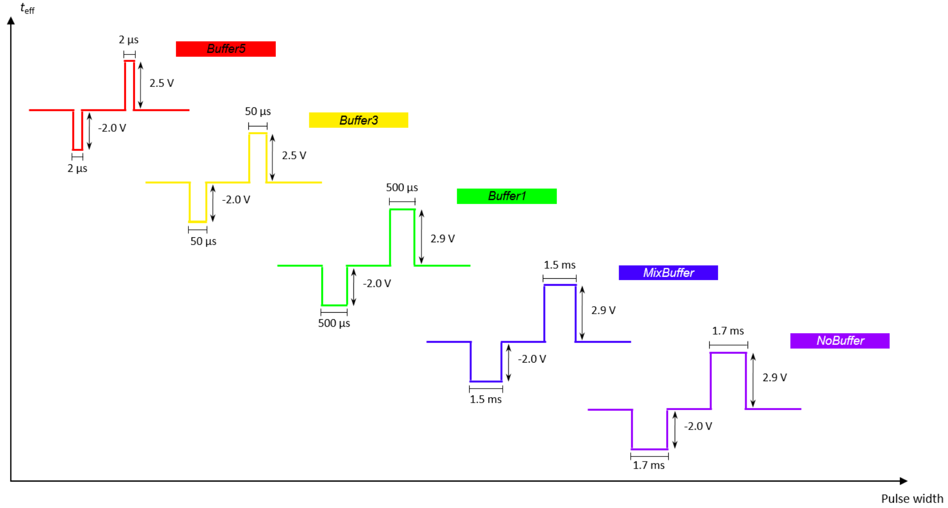

Figure 5.20: Optimized pulse parameters for each material stack. Adapted from [135]

were determined, so that all the device underwent performance tests employing the optimal combination of pulse amplitude and width. According with the asymmetric RS behaviour highlighted by the DC characterization, optimization involved both SET and RESET, in order to properly tailor the pulse parameters for both the state transitions. Concerning then the distance between consecutive pulses, 200 ms was adopted as time delay. A summary of the pulse geometry is presented in Figure 5.20, where the results of the optimization procedure are reported too. As it can be appreciated, t_{eff} turned out to play a role also in the dynamic regime: increasing the buffer layer effective thickness, both pulse width and amplitude changed. In more detail, starting from the latter, two subsets were identified, with the positive pulse amplitude of 2.9 V for $t_{eff} \leq 3$ nm which reduced to 2.5 V for Buffer3 and Buffer5 samples. Less discretized but larger differences among the material stacks were found for pulse width, that decreased from 1.7 ms for NoBuffer samples to 2 μs for Buffer5 ones. After the parameter optimization, a standard test to be adopted for all the devices was defined, with the aim of adopting a unique measure of the effect of titanium on device performances. Specifically, the impact of Ti-based buffer layers on the device endurance was evaluated employing two thousand SET-RESET pulse pairs for all the tested devices. Results are shown in Figure 5.21. Once more, with respect to the reference structure, titanium was found to play a role. However, some peculiarities were observed in this case. Differently from previous findings, endurance results indeed turned out to be best described by a classification based on $t_{eff} \geq 1$ nm, since all the devices with a buffer layer effective thickness larger than 1 nm successfully completed the fixed-length test, with endurance overcoming 2000 cycles.

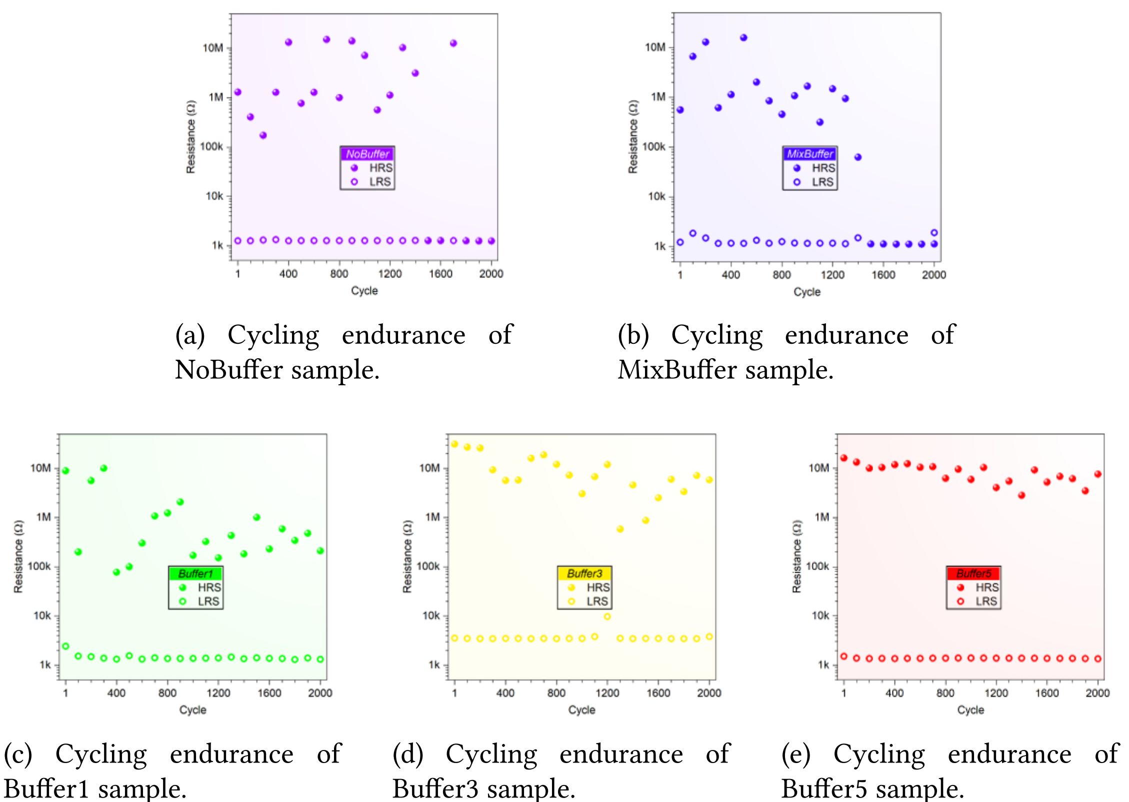

(a) Cycling endurance of NoBuffer sample.

(b) Cycling endurance of MixBuffer sample.

(c) Cycling endurance of Buffer1 sample.

(d) Cycling endurance of Buffer3 sample.

(e) Cycling endurance of Buffer5 sample.

Figure 5.21: Comparison of endurance performances, for each material stack, through a fixed-length test employing 2000 SET-RESET pulse pairs. Adapted from [135]

Particularly, this additionally meant that a higher cycling reliability was achieved by the devices with pure-Ti buffer layers, while the mixed W-Ti film did not provide significant improvements with respect to the reference structure. Both NoBuffer (Figure 5.21a) and MixBuffer Figure 5.21b samples provided indeed a maximum endurance of about 1500 cycles. With a closer look at Buffer1 Figure 5.21c, Buffer3 Figure 5.21d and Buffer5 Figure 5.21e samples, it was also highlighted how the tested devices reported a dependence of the HRS stability on t_{eff}, with less and less scattered data for the OFF state as the buffer layer effective thickness increased. Stability improvement concerning the HRS was evaluated through its coefficient of variation (CV), namely the relative standard deviation (RSD), which was reduced from 180% to 41% increasing t_{eff} from 1 nm to 5 nm (Table 5.3).
As final step in the electrical characterization of the crosspoint ReRAM cells, retention tests were performed. Similarly to the procedure adopted for endurance assessment, a common benchmark was defined for all the devices, focusing on whether the different

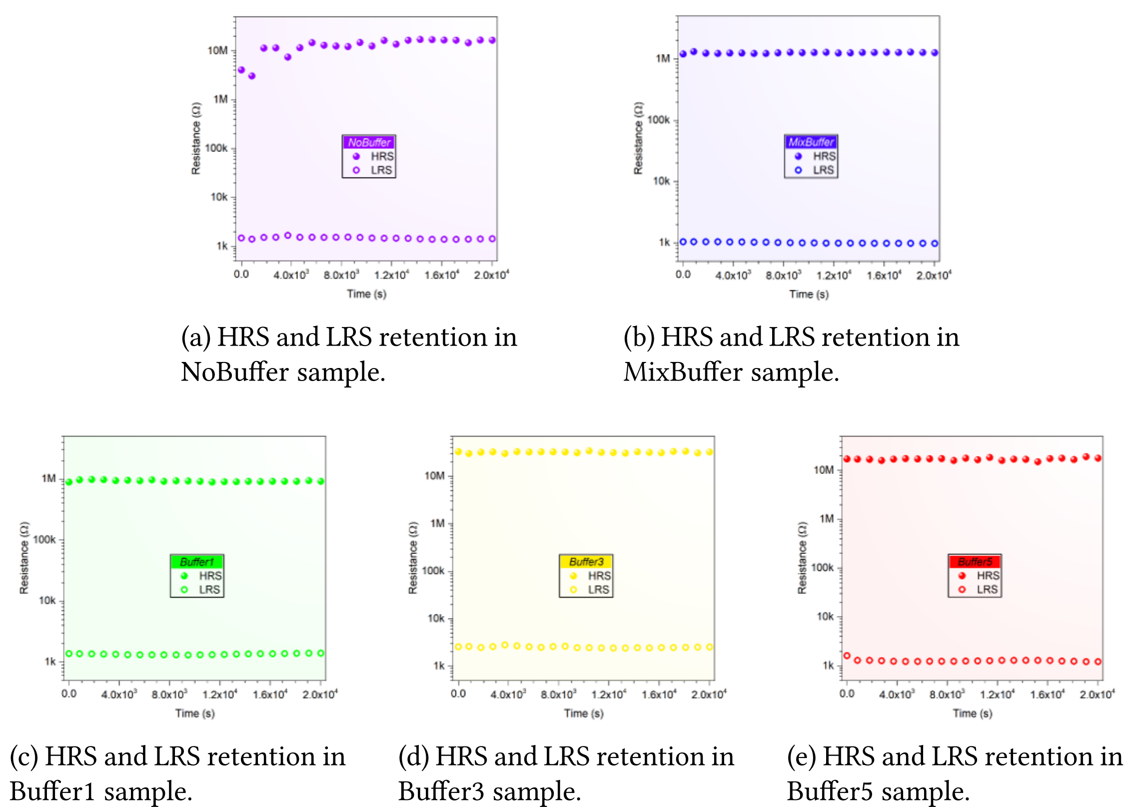

(a) HRS and LRS retention in NoBuffer sample.

(b) HRS and LRS retention in MixBuffer sample.

(c) HRS and LRS retention in Buffer1 sample.

(d) HRS and LRS retention in Buffer3 sample.

(e) HRS and LRS retention in Buffer5 sample.

Figure 5.22: Comparison of resistance state retention, for each material stack, through a common benchmark of $2{\cdot}10^4$ s. Adapted from [135]

buffer layers had a role in achieving the fixed target. Specifically, the reference value for these measurements was $2{\cdot}10^4$ s. As it is shown in Figure 5.22, the test was successfully completed by all the material stack, with a good stability of the resistance states in all the devices. Regardless of t_{eff}, both the HRS and the LRS were retained for $2{\cdot}10^4$ s with all the material stacks, and the coefficients of variation (Table 5.3) turned out to be rather low. A single exception was found for the HRS of devices from the NoBuffer sample, which reported a relative standard deviation of the resistance value of 30.0%. However, as shown in Figure 5.22a for a representative device with that material stack, this CV value originated from the initial resistance instability, which gradually reduced during the test. The overall good state retention, which can be directly related to the conductive filament stability, together with its independence from the buffer layer properties, suggested the absence of a role actively played by titanium when oxygen exchange is not crucial in determining the RS properties. Once SET and RESET transitions were

Table 5.3: Summary of endurance and retention tests with mean values and coefficients of variation for R_{HRS} and R_{LRS} [135]

Sample name	Endurance				Retention			
	R_{HRS} (MΩ)		R_{LRS} (kΩ)		R_{HRS} (MΩ)		R_{LRS} (kΩ)	
	Mean	*CV*	*Mean*	*CV*	*Mean*	*CV*	*Mean*	*CV*
NoBuffer	4.73	119%	1.27	1.4%	13.22	30.0%	1.47	4.8%
MixBuffer	3.10	156%	1.27	18.0%	1.26	2.0%	1.00	2.3%
Buffer1	1.61	180%	1.44	16.0%	0.93	2.9%	1.35	2.3%
Buffer3	10.11	87%	3.81	36.0%	32.26	3.3%	2.52	3.9%
Buffer5	8.52	41%	1.38	2.3%	17.02	5.1%	1.27	6.3%

completed, namely with the conductive filament formed or partially broken, the oxygen extraction capability of titanium, which turned out to make all the difference in the dynamic regime, was indeed no longer a key element for the device performances. Therefore, retention measurements implicitly proved that the employment of titanium buffer layers effectively translated into an enhanced control of the oxygen vacancies dynamics during the most dynamic phases of resistive switching [135].

5.5 Discussion

The upcoming integration of emerging memories in the CMOS technologies has been highlighting for a few years the need for further investigation to be possibly translated into new design rules. Additionally, in view of future applications of such emerging technologies in different frameworks of computational domain, the possibility of defining new strategies for performance tailoring has been gaining larger and larger importance. In this context, the in-depth electrical analysis of a specific issue, as the RS instability of ReRAM cells employing typical CMOS-related materials, represented one of the possible ways to contribute to the efforts in facing the unceasing demand for solutions to specific problems. The work presented in this chapter showed interesting results with a clear and quantitative meaning. It has been reported about the key role played by titanium in stabilizing and tailoring resistive switching performances, thanks to its efficient oxygen extraction which provides an improved control on one of the main aspects of the VCM mechanism: oxygen vacancies dynamics. A dependence on the amount of Ti enclosed as buffer layer between the oxidizing electrode (W) and

the oxide layer (HfO_2) has been shown, highlighting that the observed results cannot be interpreted taking into account the buffer layer thickness only. Together with a reduction, in absolute value, of both forming and switching voltages, an improvement of about 30% in endurance performances and an increase of about three orders of magnitude in response speed have been reported. Such results, obtained through a statistical approach based on th extensive analysis of more than one hundred devices, eventually turned out to suggest the Ti-buffer/W bilayer as a suitable choice to solve reliability issues in CMOS-compatible ReRAM cells based on HfO_2. Moreover, they also highlighted the possibility of tuning the device performances according to the titanium buffer layer properties, hopefully contributing to the definition of some of the new design rules for ReRAM-CMOS integration.

Chapter 6

Conclusion

Since the term *neuromorphic engineering* was coined, in 1990 [213, 214], computational systems and architectures inspired by brain have greatly evolved, to such an extent that a "Neuromorphic Revolution" is expected to start in 2024 [215–217]. Besides business and market analyses and forecasts, technological Research demonstrated, during the last few years, that both the von Neumann architecture and the Moore's law must be challenged, in order to tackle the continuously increasing need for computational power and efficiency [218, 219]. It is in this context that emerging non-volatile devices, able, or at least foreseen to be able, to implement the in-memory computing paradigm, have attracted more and more attention. Particularly, resistive switching devices stood out as feasible candidates, with their simple structure, well-suited for two-terminal devices, and a working principle based on conductivity changes upon external electrical stimuli. Also named ReRAMs, they rewarded the great interest towards them, and the consequent efforts, with promising results, opening the way for integration with the standard CMOS technology.
In this Thesis, the attention focused on a specific class of resistive switching devices, favouring those based on the valence change memory effect. This RS mechanism relies on the drift of oxygen anions, under the effect of an external voltage, within a metal oxide that consequently undergoes variations of its electrical resistance. The origin of such phenomenon is commonly ascribed to the valence changes affecting the metallic ions of the oxide as a consequence of the anion migration. This latter, in more detail, is typically described in terms of the corresponding vacancies, which are used to model the VCM mechanism although they cannot be properly defined as chemical species. Following this established methodology, the presented findings in VCM-based resistive switching devices were discussed referring to the oxygen vacancies, whose dynamics

was a major concern as fundamental aspect in the definition of the electrical properties of the tested devices. Different oxides and different structures were investigated, reporting possible technological strategies to achieve an enhanced control of the oxygen vacancies dynamics. The proposed solutions accounted for, and originated from, peculiar properties and specific requirements for each oxide, in order to always present resistive switching devices with reliable characteristics not only from the performance point of view but also concerning their fabrication.

Studies on zinc oxide have been presented first. Characterized by well-known properties like a wide direct band gap, a large exciton energy, a good thermal and chemical stability, as well as biocompatibility, this material is widely employed for a range of applications spanning from electronics to medicine. The explanation of such a versatility can be found in the richness of nanostructures ZnO can provide, and in the relatively easy processes required to produce them. Typical examples are nanoparticles and nanowires, or nanorods, which cover about 50% of the scientific works dealing with zinc oxide nanostructures (Figure 2.1a). In the field of resistive switching, ZnO has often been investigated in form of thin films or nanowires. In this Thesis, the effect of a complementary action of these structures is reported, showing the electrical performances of devices employing zinc oxide nanowires grown on top of ZnO thin films. Results for planar devices without NWs have been initially presented, showing the poor performances offered by Pt/ZnO-film/Pt structures (Figure 4.2) together with a C-AFM analysis of the filamentary resistive switching (Figure 4.8). The observed instability provided by the VCM mechanism of these devices during the electrical characterizations has been explained through the small amount of oxygen-related defects in the ZnO film, suggested by the good stoichiometry reported by XPS analysis (Figure 3.9). This lack of the ionic species needed for the redox reactions leading to VCM-based resistive switching has been reported for different film thicknesses, highlighting the necessity of facing an intrinsic issue at a deeper level with respect to the ultimate electrical performances. ZnO nanowire arrays have been proposed as a possible solution. Hydrothermally growing them on top of the zinc oxide thin film, an additional ZnO-based layer was adopted, changing the device structure to Pt/ZnO-film/ZnO-NWs/Pt and enclosing within the MIM structure a slightly more defective form of zinc oxide. Compositional analysis revealed indeed a slight understoichiometry of the nanowire arrays (Figure 3.8), which however exhibited good structural quality in terms of crystallographic orientation (Figure 3.15). Such additional layer made of ZnO NWs has been shown to be suitable to supply the underlying ZnO film with a surplus of oxygen vacancies, thus filling the lack of ionic species for VCM resistive switching. The effectiveness of this oxygen vacancies

reservoir has been proved by the huge enhancements achieved in the electrical performances, with endurance and retention results outperforming previous data reported in literature for similar devices (Table 4.1).
Following the investigation of zinc oxide, studies on hafnium dioxide have been presented. As a high-k dielectric, HfO_2 found extensive application in electronics starting from the 1990s, when the VLSI development in CMOS technology ran into the approaching physical limit for gate insulator scaling down. Thanks to the combination of its electrical properties with the potentialities offered by ALD for its deposition, hafnium dioxide became a material of choice for gate dielectrics in CMOS processes, and it established as a commonly employed oxide in electronics. Consequently, when an increasing attention started to focus on emerging memories like ReRAMs, HfO_2 naturally emerged among the possible metal oxides to be exploited, thanks to the well-established technological knowledge it offered in terms of both fabrication and CMOS integration. As a result, the number of applications of hafnium dioxide in ReRAM cells has been rapidly growing since 2008 (Figure 5.1). Despite these efforts, some open questions and unresolved issues still remain. Among them, device stability and reliability continue to be worrying when compared to the performances of other memory technologies. An example of this is represented by the case of ReRAMs employing another CMOS-compatible material like tungsten as oxidizing electrode for VCM-based devices. It was indeed previously reported that ReRAM cells exhibiting a HfO_2/W interface are affected by critical resistive switching instabilities hindering them from providing reliable performances. As a feasible solution, the insertion of a titanium buffer layer between hafnium dioxide and tungsten was proposed. In this Thesis, an extensive investigation of this RS stabilization strategy has been presented, with systematic electrical characterizations, on more than one hundred devices, aimed at evaluating the impact of titanium-based buffer layers on the performances of resistive switching device employing hafnium dioxide and tungsten as one of the electrodes. At different stages of typical resistive switching operations, the role played by titanium has been investigated varying both thickness and composition of the buffer layers. Besides pure-Ti films with thickness of 1 nm, 3 nm and 5 nm, a mixed W-Ti layer, with 10% in weight of titanium and thickness of 3 nm, has been employed too (Table 5.1). As a first step, the impact on the forming process was tested, showing an exponentially decreasing dependence of $V_{FORMING}$ on the buffer layer thickness (Figure 5.3). In more detail, it has been reported that the key parameter was not the actual physical thickness but rather an effective value (t_{eff}) accounting for the amount of titanium in the buffer layer. The mixed W-Ti buffer layer, with a thickness of 3 nm, indeed turned out to affect the forming voltage in a much different way with respect to the pure-Ti film with the same thickness,

and its t_{eff} was found to be about 0.5 nm (Figure 5.4). The forming process was also investigated performing C-AFM studies, which confirmed the reduction of $V_{FORMING}$ for increasing t_{eff} (Figure 5.5, Figure 5.6 and Figure 5.7) and showed the filamentary nature of the observed resistive switching (Figure 5.8, Figure 5.9 and Figure 5.10). This latter was also verified through a statistical analysis of the resistance levels and the switching voltages for different dimensions of the ReRAM active region, showing independence of R_{HRS}, R_{LRS}, V_{SET} and V_{RESET} from the active region width (Figure 5.14). All of these parameters were also statistically evaluated as a function of the buffer layer properties (Table 5.2), and clear differences in the results have been shown. A significant reduction of the device-to-device variability of V_{SET} has been reported for $t_{eff} \geq 3$ nm (Figure 5.18), which has also been highlighted to mark a sharp distinction for R_{LRS} (Figure 5.19). Concerning the switching voltages, stability improvements have been also observed for V_{RESET}, and both SET and RESET voltages have been reported to reduce, in absolute value, with a buffer layer effective thickness larger than 3 nm. The increase of t_{eff} turned out to also affect the device response, with improvements up to about three orders of magnitudes shown through an optimization process of pulse parameters for the dynamic operational regime (Figure 5.20). Resistive switching stabilization was ensured by titanium for endurance performances too, with all the devices employing a pure-Ti buffer layer able to overcome the early failure affecting the ReRAM cells with the mixed W-Ti film or without buffer layer (Figure 5.21). The only parameter on which titanium had a minor impact has been reported to be the state retention. All the tested devices have been indeed shown to reach a common benchmark adopted as comparison parameter, and the improvement provided by titanium took shape in the reduction of some initial instabilities observed for the devices without buffer layer (Figure 5.22). These findings have been interpreted in the light of the different oxidizing activity of titanium and tungsten in relation to reaction (1.18). Thanks to a more efficient oxygen extraction, and consequent vacancies creation, titanium can hinder the more energy demanding tungsten oxidation, especially avoiding the metastable oxides formed before WO_3 is achieved. The dependence of the presented results on t_{eff} hence comes from the role played by the amount of titanium actually enclosed between HfO_2 and tungsten, which stand out as the ultimate responsible for the RS stabilization in so far as it prevents tungsten oxidation. Device retention is an indirect proof of this. Involving a less dynamic condition of the conductive filament, hence implying a secondary role of oxygen anions and corresponding vacancies, it further highlights the importance of titanium in the critical phases of resistive switching governed by the redox processes typical of the VCM mechanism.

To conclude, this Thesis has shown different possible strategies for an improved control of the oxygen vacancies dynamics in resistive switching devices relying on the VCM mechanism. The relevance of these and similar approaches has been discussed in relation to the present needs in the field of emerging technologies, outlining future developments as they are arising from the Scientific Community. The adopted methodologies, as well as the interpretations of the results, have been constantly found, throughout this work, on the belief that the only trustworthy basis for technology is understanding of inherent mechanisms and principles. Thus explaining why oxygen vacancies were so important to present the achievements obtained for resistive switching devices.

Appendix A

Process flow for HfO_2-based crosspoint cells

Below, the complete process flow for the HfO_2-based ReRAM cells with crosspoint geometry is reported. It is the result of a series of optimization studies performed at the Center of MicroNanoTechnology (CMi) at EPFL and carried out by former members of the EPFL Microelectronic Systems Laboratory (LSM) too.

Lab: EPFL-STI-IEL-LSM
Operator Name: Vittorio Fra
Supervisor Name: Elmira Shahrabi
Date of comitee:

Téléphone:
Office: ELD 336
E-mail: vittorio.fra@polito.it

☐ Semestral Project ☐ Master Project ☐ Thesis ☑ Other

HfO_2 – based ReRAM

Description

The following process flow describes the realization of a vertically stacked single crosspoint ReRAM cell.
Key features: Pt bottom electrode, HfO_2 resistive switching layer, Ti-based buffer layer, W top electrode.

Technologies used			
Sputtering, LPCVD, ALD, photolithography, dry etching, wet etching.			
Photolith masks			
Mask #	**Critical Dimension**	**Critical Alignment**	**Remarks**
2	20 µm	First Mask	Ti/Pt BE structuration
3	1 µm	5 µm	LTO structuration for VIA definition
5	20 µm	5 µm	W/TiN TE structuration
Substrate Type			
Silicon <100>, Ø100mm, 500 nm wet oxide, single side, p type (B), 0.1-0.5 Ohm.cm			

Process outline

Step	Process description	Cross-section after process
01	**Substrate**: ***Si/SiO₂*** *Wafer cleaning (SRD rinse + O_2 plasma)* Machine: *Oxford PRS900*	View 1

02	*Adhesion layer +* *+ BE DC sputtering* Machine: *SPIDER600* Material: *Ti-Pt* Thickness: *5 nm - 125 nm*	View 1
03	*Photolitography* Machine: *ACS200 coater/develop + SuessMA6* PR: *AZECI3007 – 1.2 µm* Mask: *CD = 20 µm*	20 µm View 1
04/05	*Dry Etching* Material : *Ti [Cl_2/BCl_3]-Pt[Cl_2/Ar]* Machine: *STS Multiplex ICP* Depth: *130 nm* *+ Resist strip*	View 1
06	*LPCVD Passivation* Machine: *Centrotherm Furn.* Material: *LTO* Thickness: *100 nm*	View 1

07	*Photolithography* Machine: *ACS200 coater/develop + SuessMA6* PR: *AZECI3007 – 0.63 µm* Mask: *CD = 1 µm*	View 1
08/09	*Wet Etching* Material: *LTO [BHF]* Machine: *Plade Wetbench* Depth: *100 nm* + *Resist strip*	View 1
10/11/12	*Resist Coating* Machine: *ACS200 coater* PR : *AZECI3027 –4 µm* + *Dicing* Machine: *BM0229* + *Resist Strip*	
13	*Resistive layer ALD* Machine: *BENEQ TFS200* Material: *HfO_2* Thickness: *5 nm*	View 1

13 optional	*Buffer layer DC sputtering* Machine: *DP650* Material: *Ti or W:Ti* Thickness: *(1, 3, 5) nm*	View 1
14	*TE RF sputtering* Machine: *DP650* Material: *W* Thickness: *60 nm* + *Capping layer RF sputtering* Machine: *DP650* Material: *TiN* Thickness: *15 nm*	View 1
15	*Photolithography* Machine: *Manual coater + MJB4* PR: *AZECI3007 – 1 μm* Mask: *CD = 20 μm*	View 2

16/17	*Dry Etching* Material: *TiN [Cl_2/BCl_3]* Material: *W [SF_6]* Material: *Ti [Cl_2/BCl_3] - HfO_2 [Ar/Cl_2/BCl_3]* Machine: *STS Multiplex ICP* Depth : *83nm* + *Resist strip*	View 2

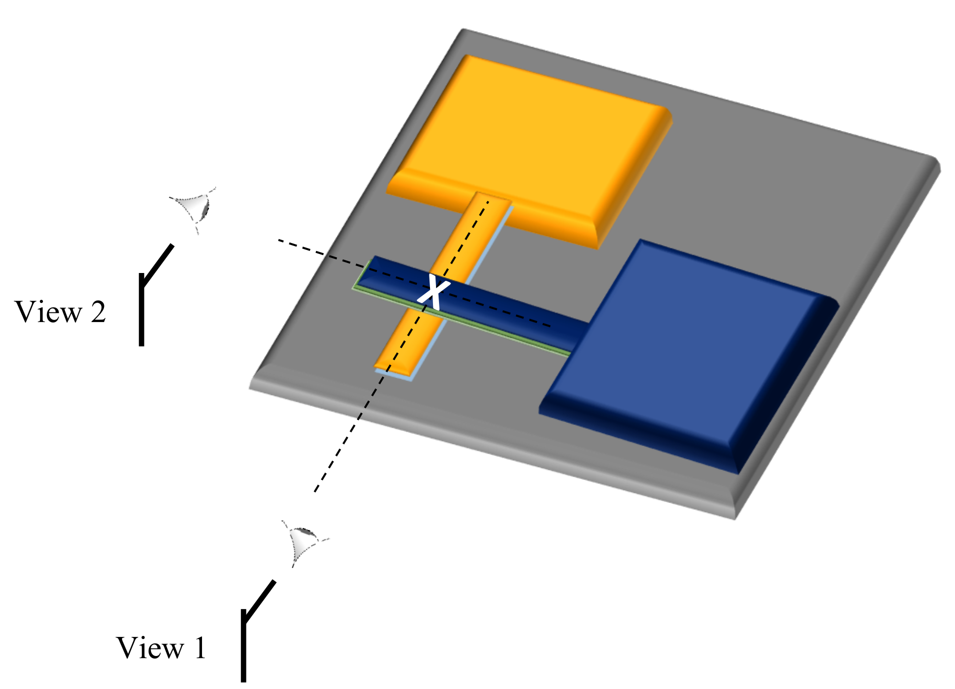

Appendix B

Force estimation in contact mode AFM measurements

The following MATLAB code reports the function `Force` written on purpose to estimate the tip-to-sample force applied during AFM measurements in contact mode. As input arguments, together with information about the employed tip, it only requires the file paths corresponding to the topography and deflection images simultaneously acquired during the measurement.

```
function [] = Force(filename,filename_defl,tip)

% Force estimation from topography and deflection images.

% By means of this function, the tip-to-sample force applied during
% an AFM measurement in contact mode can be estimated starting from
% the topography and deflection images simultaneously acquired.
% The tip model is needed as input argument of string type.
% Detailed information suitable for function running are stored for
% two tips, labelled as SCMPICV2 and Pt400B.

format long

%%%%%%%%%%%%%%%%%%%%%%%%%%%%%% INPUT ARGUMENTS %%%%%%%%%%%%%%%%%%%%%%%%%%%%%%
% Topography: filename

% Deflection: filename_defl

% Employed tip: tip
```

```
%%%%%%%%%%%%%%%%%%%%%%%%%%%%%%%%%%%%%%%%%%%%%%%%%%%%%%%%%%%%%%%%%%%%%%%%%%

%%%%%%%%%%%%%%%%%%%%%%%%%%%%%% TIP DETAILS %%%%%%%%%%%%%%%%%%%%%%%%%%%%%%%
% Tip characteristics (nominal values from manufacturer)
tips = struct();
tips.order = {'t','l','w','h','f0','k'}; % units: m, m, m, m, Hz, N/m
tips.SCMPICV2 = [1.8e-6, 450e-6, 35e-6, 12.5e-6, 10e3, 0.1];
tips.Pt400B = [2.5e-6, 400e-6, 60e-6, 80e-6, 5e3, 0.3];

% Employed tip data
t_tip = tips.(tip)(find(strcmp(tips.order,'t')==1));
l_tip = tips.(tip)(find(strcmp(tips.order,'l')==1));
w_tip = tips.(tip)(find(strcmp(tips.order,'w')==1));
h_tip = tips.(tip)(find(strcmp(tips.order,'h')==1));
f0_tip = tips.(tip)(find(strcmp(tips.order,'f0')==1));
k_tip = tips.(tip)(find(strcmp(tips.order,'k')==1));

% Estimation of actual k through f0 characterization
% https://www.nanoandmore.com/more-about-afm-cantilevers
f_meas = struct(); % Struct containing the measured frequencies, Hz
f_meas.SCMPICV2 = ();
f_meas.Pt400B = ();
f_meas_tip = f_meas.(tip);

rho_tip = (4*k_tip/(w_tip*t_tip*l_tip))*(0.162^2)/(f0_tip^2);

% Estimated k, N/m
k_est = (f_meas_tip^2)/(0.162^2)*(rho_tip*w_tip*t_tip*l_tip)/4;
%%%%%%%%%%%%%%%%%%%%%%%%%%%%%%%%%%%%%%%%%%%%%%%%%%%%%%%%%%%%%%%%%%%%%%%%%%

%%%%%%%%%%%%%%%%%%%%%%%%%%%%%% AFM TOOL DATA %%%%%%%%%%%%%%%%%%%%%%%%%%%%%%
% piezo-controller, um/V
Z_Transfer = ();

z_slope = struct(); % V/um
z_slope.SCMPICV2 = ();
z_slope.Pt400B = ();
z_slope_tip = z_slope.(tip);
%%%%%%%%%%%%%%%%%%%%%%%%%%%%%%%%%%%%%%%%%%%%%%%%%%%%%%%%%%%%%%%%%%%%%%%%%%

%%%%%%%%%%%%%%%%%%%%%%%%%%%%%% DATA IMPORT %%%%%%%%%%%%%%%%%%%%%%%%%%%%%%%
gwy2matlab = readgwychannel(filename,0);
gwy2matlab_defl = readgwychannel(filename_defl,0);
%%%%%%%%%%%%%%%%%%%%%%%%%%%%%%%%%%%%%%%%%%%%%%%%%%%%%%%%%%%%%%%%%%%%%%%%%%
```

```
setpoint = gwy2matlab_defl.data - gwy2matlab.data./Z_Transfer; % V
distribution = fitdist(setpoint(:),'Normal');
setpoint_estimation = round(distribution.mu,1);
setpoint = setpoint_estimation;

force = setpoint/(z_slope_tip/1e-6)*k_est; % N

sprintf('The estimated force is %s nN.',force.*1e9)

end
```

Appendix C

Superposition of current and topography data from C-AFM analysis

The following MATLAB code was written to obtain a point-by-point superposition of current and topography maps simultaneously acquired during C-AFM measurements. In more detail, the aim was to precisely localize the highly conductive spots on the corresponding topography image.

```
%% Superposition of current data on topography images

clear
format long

%%%%%%%%%%%%%%%%%%%%%% IMPORT MORPHOLOGY DATA %%%%%%%%%%%%%%%%%%%%%%
filename = '';
    %%% CHECK %%%
    height_check = 1; % 1 for height, 0 for deflection
    %%%%%%%%%%%%%
gwy2matlab_height = readgwychannel(filename,0);
if isfield(gwy2matlab_height,'xoff') == 0
    gwy2matlab_height.xoff = 0;
    gwy2matlab_height.yoff = 0;
end
x_height = linspace(gwy2matlab_height.xoff,gwy2matlab_height.xoff + ...
    ...
```

```
                          gwy2matlab_height.xreal,gwy2matlab_height.xres);
y_height = (gwy2matlab_height.yoff+gwy2matlab_height.yreal - ...
               linspace(0,gwy2matlab_height.yreal,gwy2matlab_height.yres));
if height_check == 1
    gwy2matlab_height.data = gwy2matlab_height.data;
end
%%%%%%%%%%%%%%%%%%%%%%%%%%%%%%%%%%%%%%%%%%%%%%%%%%%%%%%%%%%%%%%%%%%%%%%%%%%%%%

%%%%%%%%%%%%%%%%%%%%%%%% IMPORT CURRENT DATA %%%%%%%%%%%%%%%%%%%%%%%%%%%%
filename_current = '';
gwy2matlab_current = readgwychannel(filename_current,0);
if isfield(gwy2matlab_current,'xoff') == 0
    gwy2matlab_current.xoff = 0;
    gwy2matlab_current.yoff = 0;
end
x = linspace(gwy2matlab_current.xoff,gwy2matlab_current.xoff + ...
               gwy2matlab_current.xreal,gwy2matlab_current.xres);
y = (gwy2matlab_current.yoff+gwy2matlab_current.yreal - ...
      linspace(0,gwy2matlab_current.yreal,gwy2matlab_current.yres));
max_current_abs = max(abs(gwy2matlab_current.data(:)));
%%%%%%%%%%%%%%%%%%%%%%%%%%%%%%%%%%%%%%%%%%%%%%%%%%%%%%%%%%%%%%%%%%%%%%%%%%%%%%


%%%%%%%%%%%%%%%%%%% DATA PREPARATION AND VISUALIZATION %%%%%%%%%%%%%%%%%%%

threshold = []; % to be set for current spots selection
sel = 0;
for ii = 1:length(gwy2matlab_current.data(:,1)) % y
    for jj = 1:length(gwy2matlab_current.data(1,:)) % x
        if gwy2matlab_current.data(ii,jj) > ...
                threshold*max(gwy2matlab_current.data(:))
            sel = sel+1;
            x_selected(sel) = x(jj);
            y_selected(sel) = y(ii);
        end
    end
end

    %%% CHECK %%%
    check_mask = 1; % 1 for specific sub-regions, 0 otherwise
    %%%%%%%%%%%%%%%

if check_mask == 1
```

```
    % Mask parameters from Gwyddion
    mask = [ , ; ... % x-coordinate (or column number), dimension
             , ];    % y-coordinate (or row number), dimension
    x_masked = x_height(mask(1,1):(mask(1,1)+mask(1,2)));
    y_masked = y_height(mask(2,1):(mask(2,1)+mask(2,2)));
    data_masked = gwy2matlab_height.data(mask(2,1):(mask(2,1) + ...
                  mask(2,2)),mask(1,1):(mask(1,1)+mask(1,2)));

    figure
    pcolor(x_masked,y_masked,data_masked.*1e9)
    hold on
    plot(x_selected,y_selected,'.r','MarkerSize',9)
    pbaspect([1 1 1])
    shading interp
    xlabel('x-coordinate')
    ylabel('y-coordinate')
    colormap(gray)
    colorbar
    title(colorbar,'nm')
    title('Current on topography')
    set(gca,'xtick',[])
    set(gca,'ytick',[])

else

    figure
    pcolor(x_height,y_height,gwy2matlab_height.data.*1e9)
    hold on
    plot(x_selected,y_selected,'.r','MarkerSize',9)
    pbaspect([1 1 1])
    shading interp
    xlabel('x-coordinate')
    ylabel('y-coordinate')
    colormap(gray)
    colorbar
    title(colorbar,'nm')
    title('Current on topography')

end
```

Nomenclature

AFM	**A**tomic **F**orce **M**icroscopy
AI	**A**rtificial **I**ntelligence
ALD	**A**tomic **L**ayer **D**eposition
AZO	**A**luminum-doped **Z**inc **O**xide
BE	**B**ottom **E**lectrode
BOE	**B**uffer **O**xide **E**tch
C-AFM	**C**onductive **AFM**
CBRAM	**C**onductive-**B**ridge **RAM**
CC	**C**ompliance **C**urrent
CF	**C**onductive **F**ilament
CMOS	**C**omplementary **M**etal-**O**xide-**S**emiconductor
CPU	**C**entral **P**rocessing **U**nit
CVD	**C**hemical **V**apour **D**eposition
CV	**C**oefficient of **V**ariation
DC	**D**irect **C**urrent
DRAM	**D**ynamic **RAM**
ECM	**E**lectro**C**hemical **M**etallization
EPROM	**E**rasable **P**rogrammable **R**ead-**O**nly **M**emory

FESEM	**F**ield-**E**mission **S**canning **E**lectron **M**icroscopy
FTO	**F**luorine-doped **T**in **Oxide**
FWHM	**F**ull **W**idth at **H**alf **M**aximum
GO	**G**raphene **O**xide
HMT	**H**exa**M**ethylene**T**etramine
HRS	**H**igh **R**esistance **S**tate
IC	**I**ntegrated **C**ircuit
IRDS	**I**nternational **R**oadmap for **D**evices and **S**ystems
ITO	**I**ndium **T**in **O**xide
IoT	**I**nternet **o**f **T**hings
LPCVD	**L**ow **P**ressure **CVD**
LRS	**L**ow **R**esistance **S**tate
LTO	**L**ow **T**emperature **O**xide
MIM	**M**etal-**I**nsulator-**M**etal
MOSFET	**M**etal-**O**xide-**S**emiconductor **F**ield-**E**ffect **T**ransistor
NR	**N**ano**R**od
NVM	**N**on-**V**olatile **M**emory
NW	**N**ano**W**ire
OxRRAM	**Ox**ide **RRAM**
PEI	**P**oly**E**thylene**I**mine
PMC	**P**rogrammable **M**etallization **C**ell
RAM	**R**andom **A**ccess **M**emory
RRAM	**R**esistance **RAM**
RSD	**R**elative **S**tandard **D**eviation

RS	**R**esistive **S**witching
RW	**R**esistive **W**indow
ReRAM	**Re**sistive **RAM**
SA1	**S**tuck **A**t **1**
SCLC	**S**pace-**C**harge-**L**imited **C**urrent
SCM	**S**torage **C**lass **M**emory
SPM	**S**canning **P**robe **M**icroscopy
SRAM	**S**tatic **RAM**
TE	**T**op **E**lectrode
TMO	**T**ransition **M**etal **O**xide
VCM	**V**alence **C**hange **M**emory
VIA	**V**ertical **I**nterconnect **A**ccess
VLSI	**V**ery **L**arge **S**cale **I**ntegration
XPS	**X**-ray **P**hotoelectron **S**pectroscopy
XRD	**X**-**R**ay **D**iffraction

Bibliography

1. Calzecchi-Onesti, T. Sulla conduttività elettrica delle limature metalliche. *Il Nuovo Cimento* **16,** 58–64 (1884).
2. Calzecchi-Onesti, T. Sulla conduttività elettrica delle limature metalliche. *Il Nuovo Cimento* **17,** 38–42 (1885).
3. Marconi, G. Wireless telegraphy. *Journal of the Institution of Electrical Engineers* **28,** 273–290 (1899).
4. Hickmott, T. W. Low-Frequency Negative Resistance in Thin Anodic Oxide Films. *Journal of Applied Physics* **33,** 2669–2682 (1962).
5. Biederman, H. Metal-insulator-metal sandwich structures with anomalous properties. *Vacuum* **26,** 513–523 (1976).
6. Gibbons, J. & Beadle, W. Switching properties of thin NiO films. *Solid-State Electronics* **7,** 785–790 (1964).
7. Hiatt, W. R. & Hickmott, T. W. Bistable Switching in Niobium Oxide Diodes. *Applied Physics Letters* **6,** 106–108 (1965).
8. Chopra, K. L. Avalanche-Induced Negative Resistance in Thin Oxide Films. *Journal of Applied Physics* **36,** 184–187 (1965).
9. Simmons, J. & Verderber, R. New thin-film resistive memory. *Radio and Electronic Engineer* **34,** 81 (1967).
10. Argall, F. Switching phenomena in titanium oxide thin films. *Solid-State Electronics* **11,** 535–541 (1968).
11. Chua, L. Memristor-The missing circuit element. *IEEE Transactions on Circuit Theory* **18,** 507–519 (1971).
12. Chua, L. O. & Kang, S. M. Memristive Devices and Systems. *Proceedings of the IEEE* **64,** 209–223 (1976).

13. Lee, J. S., Lee, S. & Noh, T. W. Resistive switching phenomena: A review of statistical physics approaches. *Applied Physics Reviews* **2,** 031303 (2015).
14. Ielmini, D. & Waser, R. *Resistive Switching* (Wiley-VCH Verlag GmbH & Co. KGaA, Weinheim, Germany, 2016).
15. Asamitsu, A., Tomioka, Y., Kuwahara, H. & Tokura, Y. Current switching of resistive states in magnetoresistive manganites. *Nature* **388,** 50–52 (1997).
16. Zhuang, W. *et al. Novel colossal magnetoresistive thin film nonvolatile resistance random access memory (RRAM)* in *Digest. International Electron Devices Meeting,* (IEEE, 2002), 193–196.
17. Yi-Chou Chen *et al. An access-transistor-free (0T/1R) non-volatile resistance random access memory (RRAM) using a novel threshold switching, self-rectifying chalcogenide device* in *IEEE International Electron Devices Meeting 2003* (IEEE, 2003), 37.4.1–37.4.4.
18. Kinoshita, K. *et al. New Model Proposed for Switching Mechanism of ReRAM* in *2006 21st IEEE Non-Volatile Semiconductor Memory Workshop* **2006** (IEEE, 2006), 84–85.
19. Hasegawa, T., Terabe, K., Nakayama, T. & Aono, M. *Quantum Point Contact Switch using Solid Electrochemical Reaction* in *Extended Abstracts of the 2001 International Conference on Solid State Devices and Materials* **371** (The Japan Society of Applied Physics, 2001), 564–565.
20. Terabe, K., Hasegawa, T., Nakayama, T. & Aono, M. Quantized conductance atomic switch. *Nature* **433,** 47–50 (2005).
21. Mitkova, M. & Kozicki, M. Silver incorporation in Ge–Se glasses used in programmable metallization cell devices. *Journal of Non-Crystalline Solids* **299-302,** 1023–1027 (2002).
22. Baek, I. *et al. Highly scalable non-volatile resistive memory using simple binary oxide driven by asymmetric unipolar voltage pulses* in *IEDM Technical Digest. IEEE International Electron Devices Meeting, 2004.* (IEEE, 2005), 587–590.
23. Szot, K., Speier, W., Bihlmayer, G. & Waser, R. Switching the electrical resistance of individual dislocations in single-crystalline SrTiO3. *Nature Materials* **5,** 312–320 (2006).
24. Janousch, M. *et al.* Role of Oxygen Vacancies in Cr-Doped SrTiO3 for Resistance-Change Memory. *Advanced Materials* **19,** 2232–2235 (2007).
25. Strukov, D. B., Snider, G. S., Stewart, D. R. & Williams, R. S. The missing memristor found. *Nature* **453,** 80–83 (2008).

26. Smerieri, A., Berzina, T., Erokhin, V. & Fontana, M. P. Polymeric electrochemical element for adaptive networks: Pulse mode. *Journal of Applied Physics* **104,** 114513 (2008).

27. Afifi, A., Ayatollahi, A. & Raissi, F. STDP implementation using memristive nanodevice in CMOS-Nano neuromorphic networks. *IEICE Electronics Express* **6,** 148–153 (2009).

28. Di Ventra, M., Pershin, Y. V. & Chua, L. O. Circuit Elements With Memory: Memristors, Memcapacitors, and Meminductors. *Proceedings of the IEEE* **97,** 1717–1724 (2009).

29. Zamarreño-Ramos, C. *et al.* On Spike-Timing-Dependent-Plasticity, Memristive Devices, and Building a Self-Learning Visual Cortex. *Frontiers in Neuroscience* **5,** 1–22 (2011).

30. Wang, L. & Zou, H. A new emotion model of associative memory neural network based on memristor. *Neurocomputing* **410,** 83–92 (2020).

31. Desoer, C. A. & Kuh, E. S. *Basic Circuit Theory* (McGraw-Hill, 1969).

32. Muthuswamy, B. & Banerjee, S. *Introduction to Nonlinear Circuits and Networks* (Springer International Publishing, Cham, 2019).

33. Oster, G. & Auslander, D. M. The Memristor: A New Bond Graph Element. *Transactions of the ASME* **94,** 249–252 (1972).

34. Oster, G. F., Perelson, A. S. & Katchalsky, A. Network thermodynamics: dynamic modelling of biophysical systems. *Quarterly Reviews of Biophysics* **6,** 1–134 (1973).

35. Chua, L. Resistance switching memories are memristors. *Applied Physics A* **102,** 765–783 (2011).

36. Corinto, F., Civalleri, P. P. & Chua, L. O. *A complete classification of memristor devices* in *2015 European Conference on Circuit Theory and Design (ECCTD)* (IEEE, 2015), 1–4.

37. Yang, J. J. *et al.* Memristive switching mechanism for metal/oxide/metal nanodevices. *Nature Nanotechnology* **3,** 429–433 (2008).

38. Vongehr, S. & Meng, X. The missing memristor has not been found. *Scientific Reports* **5,** 1–7 (2015).

39. Kim, J., Pershin, Y. V., Yin, M., Datta, T. & Di Ventra, M. An Experimental Proof that Resistance-Switching Memory Cells are not Memristors. *Advanced Electronic Materials* **6,** 2000010 (2020).

40. Wang, F. Z., Li, L., Shi, L., Wu, H. & Chua, L. O. Φ memristor: Real memristor found. *Journal of Applied Physics* **125,** 054504 (2019).
41. Papagianni, C., Nian, Y., Wang, Y., Wu, N. & Ignatiev, A. *Impedance study of reproducible switching memory effect* in *Proceedings. 2004 IEEE Computational Systems Bioinformatics Conference* (IEEE, 2004), 125–128.
42. Waser, R. Resistive non-volatile memory devices (Invited Paper). *Microelectronic Engineering* **86,** 1925–1928 (2009).
43. Waser, R. & Wuttig, M. *Memristive Phenomena - From Fundamental Physics to Neuromorphic Computing* (eds Waser, R. & Wuttig, M.) (Forschungszentrum Jülich GmbH, Jülich, 2016).
44. Meijer, G. I. Who Wins the Nonvolatile Memory Race? *Science* **319,** 1625–1626 (2008).
45. Yu, S. *Resistive Random Access Memory (RRAM)* (2016).
46. Ielmini, D. in *Wiley Encyclopedia of Electrical and Electronics Engineering* Resistive-Switching Memory (John Wiley & Sons, Inc., Hoboken, NJ, USA, 2014).
47. Waser, R. & Aono, M. Nanoionics-based resistive switching memories. *Nature Materials* **6,** 833–840 (2007).
48. Jeong, D. S., Schroeder, H. & Waser, R. Mechanism for bipolar switching in a Pt/-TiO2/Pt resistive switching cell. *Physical Review B* **79,** 195317 (2009).
49. Yang, Y. & Lu, W. Nanoscale resistive switching devices: mechanisms and modeling. *Nanoscale* **5,** 10076 (2013).
50. Waser, R., Dittmann, R., Staikov, G. & Szot, K. Redox-Based Resistive Switching Memories - Nanoionic Mechanisms, Prospects, and Challenges. *Advanced Materials* **21,** 2632–2663 (2009).
51. Chan, M., Zhang, T., Ho, V. & Lee, P. Resistive switching effects of HfO2 high-k dielectric. *Microelectronic Engineering* **85,** 2420–2424 (2008).
52. Gaba, S. *et al.* Improvement of RRAM Device Performance Through On-Chip Resistors. *MRS Proceedings* **1430,** 177–182 (2012).
53. Jeong, D. S. *et al.* Emerging memories: resistive switching mechanisms and current status. *Reports on Progress in Physics* **75,** 076502 (2012).
54. Celano, U. *Metrology and Physical Mechanisms in New Generation Ionic Devices* Springer T (Springer International Publishing, 2016).

55. Kozicki, M., Gopalan, C., Balakrishnan, M., Park, M. & Mitkova, M. *Nonvolatile memory based on solid electrolytes* in *Proceedings. 2004 IEEE Computational Systems Bioinformatics Conference* **00** (IEEE, 2004), 10–17.

56. Kund, M. *et al. Conductive bridging RAM (CBRAM): an emerging non-volatile memory technology scalable to sub 20nm* in *IEEE InternationalElectron Devices Meeting, 2005. IEDM Technical Digest.* **00** (IEEE, 2005), 754–757.

57. Valov, I., Waser, R., Jameson, J. R. & Kozicki, M. N. Electrochemical metallization memories—fundamentals, applications, prospects. *Nanotechnology* **22,** 254003 (2011).

58. Bard, A. J. & Faulkner, L. R. *Electrochemical methods fundamentals and applications* 864 (John Wiley & Sons, Inc., 2001).

59. Waser, R. & Valov, I. Electrochemical Reactions in Nanoionics - Towards Future Resistive Switching Memories. **25,** 431–437 (2009).

60. Valov, I. & Lu, W. D. Nanoscale electrochemistry using dielectric thin films as solid electrolytes. *Nanoscale* **8,** 13828–13837 (2016).

61. Maier, J. Ionic conduction in space charge regions. *Progress in Solid State Chemistry* **23,** 171–263 (1995).

62. Strukov, D. B. & Williams, R. S. Exponential ionic drift: Fast switching and low volatility of thin-film memristors. *Applied Physics A: Materials Science and Processing* **94,** 515–519 (2009).

63. Ielmini, D. Modeling the Universal Set/Reset Characteristics of Bipolar RRAM by Field- and Temperature-Driven Filament Growth. *IEEE Transactions on Electron Devices* **58,** 4309–4317 (2011).

64. Zhu, J., Zhang, T., Yang, Y. & Huang, R. A comprehensive review on emerging artificial neuromorphic devices. *Applied Physics Reviews* **7,** 011312 (2020).

65. Menzel, S., Linn, E. & Waser, R. in *Emerging Nanoelectronic Devices* 137–161 (John Wiley & Sons Ltd, Chichester, United Kingdom, 2014).

66. Kröger, F. & Vink, H. Relations between the concentrations of imperfections in solids. *Journal of Physics and Chemistry of Solids* **5,** 208–223 (1958).

67. Celano, U. *et al.* Switching mechanism and reverse engineering of low-power Cu-based resistive switching devices. *Nanoscale* **5,** 11187–11192 (2013).

68. Menzel, S., Böttger, U., Wimmer, M. & Salinga, M. Physics of the Switching Kinetics in Resistive Memories. *Advanced Functional Materials* **25,** 6306–6325 (2015).

69. Goux, L. & Valov, I. Electrochemical processes and device improvement in conductive bridge RAM cells. *physica status solidi (a)* **213,** 274–288 (2016).

70. Waser, R. Redox-Based Resistive Switching Memories. *Journal of Nanoscience and Nanotechnology* **12,** 7628–7640 (2012).

71. Gao, B., Kang, J., Liu, L., Liu, X. & Yu, B. A physical model for bipolar oxide-based resistive switching memory based on ion-transport-recombination effect. *Applied Physics Letters* **98,** 232108 (2011).

72. Degraeve, R. *et al. Hourglass concept for RRAM: A dynamic and statistical device model* in *Proceedings of the 21th International Symposium on the Physical and Failure Analysis of Integrated Circuits (IPFA)* (IEEE, 2014), 245–249.

73. Sawa, A. Resistive switching in transition metal oxides. *Materials Today* **11,** 28–36 (2008).

74. Jeong, D. S., Schroeder, H. & Waser, R. Abnormal bipolar-like resistance change behavior induced by symmetric electroforming in Pt/TiO2/Pt resistive switching cells. *Nanotechnology* **20,** 0–4 (2009).

75. Celano, U. *et al.* Evidences of areal switching in Vacancy-Modulated Conductive Oxide (VMCO) memory. *Microelectronic Engineering* **178,** 122–124 (2017).

76. Celano, U. *Electrical Atomic Force Microscopy for Nanoelectronics* (Springer International Publishing, Cham, 2019).

77. Govoreanu, B. *et al. Vacancy-modulated conductive oxide resistive RAM (VMCO-RRAM): An area-scalable switching current, self-compliant, highly nonlinear and wide on/off-window resistive switching cell* in *2013 IEEE International Electron Devices Meeting* (IEEE, 2013), 10.2.1–10.2.4.

78. Langmore, I. & Krasner, D. *Applied Data Science - Course notes* (2013).

79. Von Neumann, J. First draft of a report on the EDVAC. *IEEE Annals of the History of Computing* **15,** 27–75 (1993).

80. Ali, A. & Syed, K. S. in *Advances in Computers* 87–118 (Elsevier Inc., 2013).

81. Machanick, P. The case for SRAM main memory. *ACM SIGARCH Computer Architecture News* **24,** 23–30 (1996).

82. Natarajan, S., Chung, S., Paris, L. & Keshavarzi, A. Searching for the dream embedded memory. *IEEE Solid-State Circuits Magazine* **1,** 34–44 (2009).

83. Chen, A., Hutchby, J., Zhirnov, V. V. & Bourianoff, G. *Emerging Nanoelectronic Devices* (John Wiley & Sons Ltd, Chichester, United Kingdom, 2015).

84. Beyond CMOS. in *International Roadmap for Devices and Systems* (IEEE, 2020).

85. Sebastian, A., Le Gallo, M., Khaddam-Aljameh, R. & Eleftheriou, E. Memory devices and applications for in-memory computing. *Nature Nanotechnology* **15,** 529–544 (2020).

86. Freitas, R. F. & Wilcke, W. W. Storage-class memory: The next storage system technology. *IBM Journal of Research and Development* **52,** 439–447 (2008).

87. Cappelletti, P. *Non volatile memory evolution and revolution* in *2015 IEEE International Electron Devices Meeting (IEDM)* (IEEE, 2015).

88. Levisse, A., Giraud, B., Noel, J.-P., Moreau, M. & Portal, J.-M. *RRAM Crossbar Arrays for Storage Class Memory Applications: Throughput and Density Considerations* in *2018 Conference on Design of Circuits and Integrated Systems (DCIS)* (IEEE, 2018), 1–6.

89. Zahoor, F., Azni Zulkifli, T. Z. & Khanday, F. A. Resistive Random Access Memory (RRAM): an Overview of Materials, Switching Mechanism, Performance, Multilevel Cell (mlc) Storage, Modeling, and Applications. *Nanoscale Research Letters* **15** (2020).

90. Ielmini, D. & Wong, H.-S. P. In-memory computing with resistive switching devices. *Nature Electronics* **1,** 333–343 (2018).

91. Chen, Y. ReRAM: History, Status, and Future. *IEEE Transactions on Electron Devices* **67,** 1420–1433 (2020).

92. Wulf, W. A. & McKee, S. A. Hitting the Memory Wall: Implications of the Obvious. *ACM SIGARCH Computer Architecture News* **23,** 20–24 (1995).

93. Huang, X., Liu, C., Jiang, Y.-G. & Zhou, P. In-memory computing to break the memory wall. *Chinese Physics B* **29,** 078504 (2020).

94. Prall, K. *Benchmarking and Metrics for Emerging Memory* in *2017 IEEE International Memory Workshop (IMW)* **6** (IEEE, 2017), 1–5.

95. Zhao, Y., Deng, B., Huang, J., Lu, H. & Hua, X.-S. *Stylized Adversarial AutoEncoder for Image Generation* in *Proceedings of the 2017 ACM on Multimedia Conference - MM '17* (ACM Press, New York, New York, USA, 2017), 244–251.

96. Zhao, J. *et al.* Dual-agent GANs for photorealistic and identity preserving profile face synthesis. *Advances in Neural Information Processing Systems,* 66–76 (2017).

97. Sindhu, N. & Mamatha, H. R. in, 197–211 (Springer Singapore, 2021).

98. Huawei AI. *Huawei presents "Unfinished Symphony"* 2019.

99. Levin, R., Elgammal, A., Gotham, M., Werzowa, W. & Siegert, C. *Articial intelligence will complete Beethoven's 10th Symphony* 2019.
100. Computing on the brain. *Nature Electronics* **3,** 347–347 (2020).
101. Bains, S. The business of building brains. *Nature Electronics* **3,** 348–351 (2020).
102. Citri, A. & Malenka, R. C. Synaptic Plasticity: Multiple Forms, Functions, and Mechanisms. *Neuropsychopharmacology* **33,** 18–41 (2008).
103. Dharani, K. *The Biology of Thought* (Elsevier, 2015).
104. Zhang, W. *et al.* Neuro-inspired computing chips. *Nature Electronics* **3,** 371–382 (2020).
105. NEUROTECH. *Neuromorphic Computing Technology (NCT) state of the art* tech. rep. (2020).
106. Sangwan, V. K. & Hersam, M. C. Neuromorphic nanoelectronic materials. *Nature Nanotechnology* **15,** 517–528 (2020).
107. Zhang, Y. *et al.* Brain-inspired computing with memristors: Challenges in devices, circuits, and systems. *Applied Physics Reviews* **7,** 011308 (2020).
108. Spiga, S., Sebastian, A., Querlioz, D. & Rajendran, B. *Memristive Devices for Brain-Inspired Computing* (Elsevier, 2020).
109. Chakraborty, I., Jaiswal, A., Saha, A. K., Gupta, S. K. & Roy, K. Pathways to efficient neuromorphic computing with non-volatile memory technologies. *Applied Physics Reviews* **7,** 021308 (2020).
110. Milo, V., Malavena, G., Monzio Compagnoni, C. & Ielmini, D. Memristive and CMOS Devices for Neuromorphic Computing. *Materials* **13,** 166 (2020).
111. Wang, Z. *et al.* Resistive switching materials for information processing. *Nature Reviews Materials* **5,** 173–195 (2020).
112. Li, Y. *et al.* Filament-Free Bulk Resistive Memory Enables Deterministic Analogue Switching. *Advanced Materials* **2003984,** 2003984 (2020).
113. Marković, D., Mizrahi, A., Querlioz, D. & Grollier, J. Physics for neuromorphic computing. *Nature Reviews Physics* **2,** 499–510 (2020).
114. Ielmini, D. & Ambrogio, S. Emerging neuromorphic devices. *Nanotechnology* **31,** 092001 (2020).
115. Zidan, M. A. & Lu, W. D. *RRAM fabric for neuromorphic and reconfigurable compute-in-memory systems* in *2019 IEEE Custom Integrated Circuits Conference (CICC)* (IEEE, 2019).

116. Li, H., Raina, P. & Wong, H.-S. P. *Neuro-inspired computing with emerging memories: where device physics meets learning algorithms* in *Spintronics XII* (SPIE, 2019).

117. Hui, F. *et al.* Graphene and Related Materials for Resistive Random Access Memories. *Advanced Electronic Materials* **3,** 1600195 (2017).

118. Cha, A.-N. *et al.* An All-Organic Composite System for Resistive Change Memory via the Self-Assembly of Plastic-Crystalline Molecules. *ACS Applied Materials & Interfaces* **9,** 2730–2738 (2017).

119. Gupta, V., Kapur, S., Saurabh, S. & Grover, A. Resistive Random Access Memory: A Review of Device Challenges. *IETE Technical Review* **37,** 377–390 (2020).

120. Huang, T., Chen, J., Ting, Y. & Wu, W. Ni/NiO/HfO2 Core/Multishell Nanowire ReRAM Devices with Excellent Resistive Switching Properties. *Advanced Electronic Materials* **4,** 1800256 (2018).

121. Sassine, G. *et al.* Hybrid-RRAM toward Next Generation of Nonvolatile Memory: Coupling of Oxygen Vacancies and Metal Ions. *Advanced Electronic Materials* **5,** 1800658 (2019).

122. Yen, T. J., Gismatulin, A., Volodin, V., Gritsenko, V. & Chin, A. All Nonmetal Resistive Random Access Memory. *Scientific Reports* **9,** 6144 (2019).

123. Özgür, Ü. *et al.* A comprehensive review of ZnO materials and devices. *Journal of Applied Physics* **98,** 041301 (2005).

124. Gomez, J. L. & Tigli, O. Zinc oxide nanostructures: from growth to application. *Journal of Materials Science* **48,** 612–624 (2013).

125. Cauda, V. *et al.* in *Handbook of Nanomaterials Properties* 26, 137–177 (Springer Berlin Heidelberg, Berlin, Heidelberg, 2014).

126. Robertson, J. High dielectric constant oxides. *The European Physical Journal Applied Physics* **28,** 265–291 (2004).

127. Choi, J., Mao, Y. & Chang, J. Development of hafnium based high-k materials—A review. *Materials Science and Engineering: R: Reports* **72,** 97–136 (2011).

128. Hong, X. *et al.* Oxide-based RRAM materials for neuromorphic computing. *Journal of Materials Science* **53,** 8720–8746 (2018).

129. Zhang, Y., Ram, M. K., Stefanakos, E. K. & Goswami, D. Y. Synthesis, Characterization, and Applications of ZnO Nanowires. *Journal of Nanomaterials* **2012,** 1–22 (2012).

130. Fra, V. *et al.* Hydrothermally grown ZnO nanowire array as an oxygen vacancies reservoir for improved resistive switching. *Nanotechnology* **31,** 374001 (2020).

131. Laegu Kang *et al.* Electrical characteristics of highly reliable ultrathin hafnium oxide gate dielectric. *IEEE Electron Device Letters* **21,** 181–183 (2000).

132. Gusev, E. *et al. Ultrathin high-K gate stacks for advanced CMOS devices* in *International Electron Devices Meeting. Technical Digest* (IEEE, 2001), 20.1.1–20.1.4.

133. Heyns, M. *et al. Scaling of high-k dielectrics towards sub-1nm EOT* in *2003 International Symposium on VLSI Technology, Systems and Applications. Proceedings of Technical Papers* (IEEE, 2003), 247–250.

134. Kim, K. R. *et al.* Resistive switching characteristics of HfO2 grown by atomic layer deposition. *Journal of the Korean Physical Society* **49** (2006).

135. Fra, V., Shahrabi, E., Leblebici, Y. & Ricciardi, C. Investigation on the Stabilizing Effect of Titanium in HfO2-Based Resistive Switching Devices With Tungsten Electrode. *Frontiers in Nanotechnology* **2,** 1–14 (2020).

136. Yang, Y. & Huang, R. Probing memristive switching in nanoionic devices. *Nature Electronics* **1,** 274–287 (2018).

137. Kunat, M., Gil Girol, S., Becker, T., Burghaus, U. & Wöll, C. Stability of the polar surfaces of ZnO: A reinvestigation using He-atom scattering. *Physical Review B* **66,** 081402 (2002).

138. Cao, H. *et al.* Preparation and characterization of Al and Mn doped ZnO (ZnO: (Al, Mn)) transparent conducting oxide films. *Journal of Solid State Chemistry* **177,** 1480–1487 (2004).

139. Coppa, B. J. *et al.* In situ cleaning and characterization of oxygen- and zinc-terminated, n- type, ZnO{0001} surfaces. *Journal of Applied Physics* **95,** 5856–5864 (2004).

140. Jeong, Y. *et al.* Bias-Stress-Stable Solution-Processed Oxide Thin Film Transistors. *ACS Applied Materials & Interfaces* **2,** 611–615 (2010).

141. Heinhold, R., Williams, G. T., Cooil, S. P., Evans, D. A. & Allen, M. W. Influence of polarity and hydroxyl termination on the band bending at ZnO surfaces. *Physical Review B* **88,** 235315 (2013).

142. Milano, G. *et al.* Tuning ZnO Nanowire Dissolution by Electron Beam Modification of Surface Wetting Properties. *The Journal of Physical Chemistry C* **122,** 8011–8021 (2018).

143. Conti, D. *et al.* Resistive switching in sub-micrometric ZnO polycrystalline films. *Nanotechnology* **30,** 065707 (2019).

144. Arguello, C. A., Rousseau, D. L. & Porto, S. P. S. First-Order Raman Effect in Wurtzite-Type Crystals. *Physical Review* **181,** 1351–1363 (1969).

145. Calleja, J. M. & Cardona, M. Resonant Raman scattering in ZnO. *Physical Review B* **16,** 3753–3761 (1977).

146. Cuscó, R. *et al.* Temperature dependence of Raman scattering in ZnO. *Physical Review B* **75,** 165202 (2007).

147. Zhang, R., Yin, P.-G., Wang, N. & Guo, L. Photoluminescence and Raman scattering of ZnO nanorods. *Solid State Sciences* **11,** 865–869 (2009).

148. Russo, V., Ghidelli, M., Gondoni, P., Casari, C. S. & Li Bassi, A. Multi-wavelength Raman scattering of nanostructured Al-doped zinc oxide. *Journal of Applied Physics* **115,** 073508 (2014).

149. Milano, G. *et al.* Unravelling Resistive Switching Mechanism in ZnO NW Arrays: The Role of the Polycrystalline Base Layer. *The Journal of Physical Chemistry C* **122,** 866–874 (2018).

150. Laurenti, M., Porro, S., Pirri, C. F., Ricciardi, C. & Chiolerio, A. Zinc Oxide Thin Films for Memristive Devices: A Review. *Critical Reviews in Solid State and Materials Sciences* **42,** 153–172 (2017).

151. Chang, W. Y. *et al.* Unipolar resistive switching characteristics of ZnO thin films for nonvolatile memory applications. *Applied Physics Letters* **92,** 022110 (2008).

152. Lee, S., Kim, H., Park, J. & Yong, K. Coexistence of unipolar and bipolar resistive switching characteristics in ZnO thin films. *Journal of Applied Physics* **108,** 076101 (2010).

153. Porro, S. *et al.* Multiple resistive switching in core–shell ZnO nanowires exhibiting tunable surface states. *Journal of Materials Chemistry C* **5,** 10517–10523 (2017).

154. Zhou, W. *et al.* Optically modulated electric synapses realized with memristors based on ZnO nanorods. *Applied Physics Letters* **113,** 061107 (2018).

155. Park, J., Lee, S. & Yong, K. Photo-stimulated resistive switching of ZnO nanorods. *Nanotechnology* **23,** 385707 (2012).

156. Park, J., Lee, S., Lee, J. & Yong, K. A Light Incident Angle Switchable ZnO Nanorod Memristor: Reversible Switching Behavior Between Two Non-Volatile Memory Devices. *Advanced Materials* **25,** 6423–6429 (2013).

157. Younis, A. *et al.* High-Performance Nanocomposite Based Memristor with Controlled Quantum Dots as Charge Traps. *ACS Applied Materials & Interfaces* **5,** 2249–2254 (2013).

158. Dugaiczyk, L. *et al.* Resistive switching in single vertically-aligned ZnO nanowire grown directly on Cu substrate. *Chemical Physics Letters* **575,** 112–114 (2013).

159. Yoo, E. J., Shin, I. K., Yoon, T. S., Choi, Y. J. & Kang, C. J. Resistive Switching Characteristics of ZnO Nanowires. *Journal of Nanoscience and Nanotechnology* **14,** 9459–9464 (2014).

160. Anoop, G., Panwar, V., Kim, T. Y. & Jo, J. Y. Resistive Switching in ZnO Nanorods/Graphene Oxide Hybrid Multilayer Structures. *Advanced Electronic Materials* **3,** 1600418 (2017).

161. Tseng, Z.-L. *et al.* Electrical bistability in hybrid ZnO nanorod/polymethylmethacrylate heterostructures. *Applied Physics Letters* **97,** 212103 (2010).

162. Simanjuntak, F. M. *et al.* Role of nanorods insertion layer in ZnO-based electrochemical metallization memory cell. *Semiconductor Science and Technology* **32,** 124003 (2017).

163. Sun, Y. *et al.* High On–Off Ratio Improvement of ZnO-Based Forming-Free Memristor by Surface Hydrogen Annealing. *ACS Applied Materials & Interfaces* **7,** 7382–7388 (2015).

164. Shen, G.-H. *et al.* Low switching-threshold-voltage zinc oxide nanowire array resistive random access memory. *Thin Solid Films* **618,** 90–94 (2016).

165. Jasmin, A., Porro, S., Chiolerio, A., Pirri, C. F. & Ricciardi, C. *Polymer coated ZnO nanowires for memristive devices* in *2015 IEEE 15th International Conference on Nanotechnology (IEEE-NANO)* (IEEE, 2015), 496–498.

166. Chang, W. Y., Lin, C. A., He, J. H. & Wu, T. B. Resistive switching behaviors of ZnO nanorod layers. *Applied Physics Letters* **96,** 242109 (2010).

167. Park, S. *et al.* Resistive switching characteristics of sol-gel based ZnO nanorods fabricated on flexible substrates. *physica status solidi (RRL) - Rapid Research Letters* **7,** 493–496 (2013).

168. Huang, C.-H. *et al.* ZnO 1−x Nanorod Arrays/ZnO Thin Film Bilayer Structure: From Homojunction Diode and High-Performance Memristor to Complementary 1D1R Application. *ACS Nano* **6,** 8407–8414 (2012).

169. Milano, G., Porro, S., Valov, I. & Ricciardi, C. Recent Developments and Perspectives for Memristive Devices Based on Metal Oxide Nanowires. *Advanced Electronic Materials* **5,** 1800909 (2019).

170. Chang, W.-Y. *et al.* Unipolar resistive switching characteristics of ZnO thin films for nonvolatile memory applications. *Applied Physics Letters* **92,** 022110 (2008).

171. Zhuge, F. *et al.* Improvement of resistive switching in Cu/ZnO/Pt sandwiches by weakening the randomicity of the formation/rupture of Cu filaments. *Nanotechnology* **22,** 275204 (2011).

172. Huang, H.-W. *et al.* Stability scheme of ZnO-thin film resistive switching memory: influence of defects by controllable oxygen pressure ratio. *Nanoscale Research Letters* **8,** 483 (2013).

173. Laurenti, M., Porro, S., Pirri, C. F., Ricciardi, C. & Chiolerio, A. Zinc Oxide Thin Films for Memristive Devices: A Review. *Critical Reviews in Solid State and Materials Sciences* **42,** 153–172 (2017).

174. Op de Beeck, J. *et al.* Direct imaging and manipulation of ionic diffusion in mixed electronic–ionic conductors. *Nanoscale* **10,** 12564–12572 (2018).

175. Simanjuntak, F. M., Ohno, T. & Samukawa, S. Neutral Oxygen Beam Treated ZnO-Based Resistive Switching Memory Device. *ACS Applied Electronic Materials* **1,** 18–24 (2019).

176. Chen, C., Pan, F., Wang, Z. S., Yang, J. & Zeng, F. Bipolar resistive switching with self-rectifying effects in Al/ZnO/Si structure. *Journal of Applied Physics* **111,** 013702 (2012).

177. More, K. D. *et al.* Highly stable switching and long retention property of spin coated ZnO thin film for resistive non-volatile memory application. *Materials Research Express* **6,** 096429 (2019).

178. Bhushan, B. *Scanning Probe Microscopy in Nanoscience and Nanotechnology* (Springer Berlin Heidelberg, Berlin, Heidelberg, 2010).

179. Lanza, M. *Conductive Atomic Force Microscopy* (Wiley-VCH Verlag GmbH & Co. KGaA, Weinheim, Germany, 2017).

180. Lanza, M., Celano, U. & Miao, F. Nanoscale characterization of resistive switching using advanced conductive atomic force microscopy based setups. *Journal of Electroceramics* **39,** 94–108 (2017).

181. Binnig, G., Quate, C. F. & Gerber, C. Atomic Force Microscope. *Physical Review Letters* **56,** 930–933 (1986).

182. Jiang, L. *et al.* Understanding Current Instabilities in Conductive Atomic Force Microscopy. *Materials* **12,** 459 (2019).

183. Münstermann, R. *et al.* Morphological and electrical changes in TiO 2 memristive devices induced by electroforming and switching. *physica status solidi (RRL) - Rapid Research Letters* **4,** 16–18 (2010).

184. Celano, U. *et al.* Imaging the three-dimensional conductive channel in filamentary-based oxide resistive switching memory. *Nano Letters* **15,** 7970–7975 (2015).

185. Celano, U. *et al.* Understanding the Dual Nature of the Filament Dissolution in Conductive Bridging Devices. *The Journal of Physical Chemistry Letters* **6,** 1919–1924 (2015).

186. Singh, A. K., Blonkowski, S. & Kogelschatz, M. Resistive switching study in HfO 2 based resistive memories by conductive atomic force microscopy in vacuum. *Journal of Applied Physics* **124,** 014501 (2018).

187. Sebastian, A. *et al.* Resistance switching at the nanometre scale in amorphous carbon. *New Journal of Physics* **13,** 013020 (2011).

188. Milano, G., Boarino, L. & Ricciardi, C. Junction properties of single ZnO nanowires with asymmetrical Pt and Cu contacts. *Nanotechnology* **30,** 244001 (2019).

189. Milano, G. *et al.* Self-limited single nanowire systems combining all-in-one memristive and neuromorphic functionalities. *Nature Communications* **9,** 5151 (2018).

190. Miranda, E., Milano, G. & Ricciardi, C. Compact Modeling of the I-V Characteristics of ZnO Nanowires Including Nonlinear Series Resistance Effects. *IEEE Transactions on Nanotechnology* **19,** 297–300 (2020).

191. Haynes, W. M. *CRC Handbook of Chemistry and Physics* (CRC Press, Boca Raton, FL, 2014).

192. Hasegawa, T., Terabe, K., Tsuruoka, T. & Aono, M. Atomic Switch: Atom/Ion Movement Controlled Devices for Beyond Von-Neumann Computers. *Advanced Materials* **24,** 252–267 (2012).

193. Tappertzhofen, S., Waser, R. & Valov, I. Impact of the Counter-Electrode Material on Redox Processes in Resistive Switching Memories. *ChemElectroChem* **1,** 1287–1292 (2014).

194. Gu, T. Metallic filament formation by aligned oxygen vacancies in ZnO-based resistive switches. *Journal of Applied Physics* **115,** 203707 (2014).

195. Lim, E. & Ismail, R. Conduction Mechanism of Valence Change Resistive Switching Memory: A Survey. *Electronics* **4,** 586–613 (2015).

196. Murgatroyd, P. N. Theory of space-charge-limited current enhanced by Frenkel effect. *Journal of Physics D: Applied Physics* **3,** 308 (1970).

197. Wang, X. *et al.* *Extending gate dielectric scaling limit by use of nitride or oxynitride* in *1995 Symposium on VLSI Technology. Digest of Technical Papers* **06520** (Japan Soc. Appl. Phys, 1995).

198. Qi, W.-j. *et al. High-K gate dielectrics* in *SPIE Conference on Microelectronic Device Technology* **3881** (1999).

199. Byoung Hun Lee *et al. Ultrathin hafnium oxide with low leakage and excellent reliability for alternative gate dielectric application* in *International Electron Devices Meeting. Technical Digest* (IEEE, 1999), 133–136.

200. Yang, F. & Kotecki, D. E. Electrical and Structural Characterization of HfO2 MIM Capacitors. *MRS Proceedings* **745,** N5.16 (2002).

201. Mohammad, B. *et al.* State of the art of metal oxide memristor devices. *Nanotechnology Reviews* **5,** 311–329 (2016).

202. Xue, K.-H. & Miao, X.-S. Oxygen vacancy chain and conductive filament formation in hafnia. *Journal of Applied Physics* **123,** 161505 (2018).

203. Rodriguez-Fernandez, A., Muñoz-Gorriz, J., Suñé, J. & Miranda, E. A new method for estimating the conductive filament temperature in OxRAM devices based on escape rate theory. *Microelectronics Reliability* **88-90,** 142–146 (2018).

204. Shahrabi, E., LaGrange, T., Demirci, T. & Leblebici, Y. Performance improvement of chip-level CMOS-integrated ReRAM cells through material optimization. *Microelectronic Engineering* **214,** 74–80 (2019).

205. Wang, J., Li, L., Huyan, H., Pan, X. & Nonnenmann, S. S. Highly Uniform Resistive Switching in HfO 2 Films Embedded with Ordered Metal Nanoisland Arrays. *Advanced Functional Materials* **29,** 1808430 (2019).

206. Shahrabi, E. *et al.* Switching Kinetics Control of W-Based ReRAM Cells in Transient Operation by Interface Engineering. *Advanced Electronic Materials* **5,** 1800835 (2019).

207. Kim, W. *et al.* Impact of oxygen exchange reaction at the ohmic interface in Ta 2 O 5 -based ReRAM devices. *Nanoscale* **8,** 17774–17781 (2016).

208. Guo, Y. & Robertson, J. Materials selection for oxide-based resistive random access memories. *Applied Physics Letters* **105,** 223516 (2014).

209. Tirano, S. *et al.* Accurate analysis of parasitic current overshoot during forming operation in RRAMs. *Microelectronic Engineering* **88,** 1129–1132 (2011).

210. Nafria, M. *et al.* (Invited) Advanced Measurement Techniques for the Characterization of ReRAM Devices. *ECS Transactions* **79,** 139–148 (2017).

211. *Projects at the EPFL Center of MicroNanotechnology* (CMi EPFL, 2020).

212. Lassner, E. & Schubert, W.-D. *Tungsten* 422 (Springer US, Boston, MA, 1999).

213. Mead, C. Neuromorphic electronic systems. *Proceedings of the IEEE* **78,** 1629–1636 (1990).

214. Mead, C. How we created neuromorphic engineering. *Nature Electronics* **3,** 434–435 (2020).

215. Yole Developpement. *Artificial Intelligence Computing for Customer report - Press Release* tech. rep. (2019), 1–5.

216. Yole Developpement. *Neuromorphic Sensing & Computing report - Press Release* tech. rep. (2019), 1–5.

217. Pelé, A.-F. Neuromorphic Revolution to Start in 2024. *EE Times Europe,* 1–7 (2019).

218. Big data needs a hardware revolution. *Nature* **554,** 145–146 (2018).

219. Berggren, K. *et al.* Roadmap on emerging hardware and technology for machine learning. *Nanotechnology* **32,** 012002 (2021).

This Ph.D. thesis has been typeset by means of the TeX-system facilities. The typesetting engine was LuaLaTeX. The document class was `toptesi`, by Claudio Beccari, with option `tipotesi =scudo`. This class is available in every up-to-date and complete TeX-system installation.